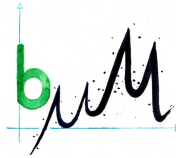




UNIVERSITÄT  
BAYREUTH



UNIVERSITY OF BAYREUTH – MICROMETEOROLOGY

---

Master Thesis

**What drives submeso-scale motions in the  
wintertime Arctic atmospheric boundary layer? A  
field study using Fiber-Optic Distributed Sensing in  
Ny-Ålesund, Svalbard**



Jannis-Michael Huss

Student number: 1599250

supervised by

Prof. Dr. Christoph Thomas

Dr. Wolfgang Babel

---

Bayreuth, November 2021

# Abstract

The drivers of transport of energy, momentum and matter across the atmospheric boundary layer (ABL) are key quantities for our comprehension and prediction of atmospheric processes on all scales. Yet we lack a profound understanding of these drivers for a wide range of conditions where the absence of solar radiation results in a lack of convective mixing and the ABL becomes stably stratified. This particularly applies to polar night in the Arctic with its constant absence of daylight. Traditional measurement techniques, relying on point measurements, are failing to resolve the relevant processes in these conditions, which contradict the commonly assumed similarity relationships applying to the convective ABL.

The NY-Ålesund Turbulence Fiber Optic eXperiment (NYTEFOX) on Svalbard aimed at improving on the observational base of these processes, commonly summarized as submeso-scale motions, by combining classic observing systems with a large deployment of the novel fiber-optic distributed sensing (FODS) technique that allows for continuous observations in both time and space. The targeted research questions of this thesis were (1) which drivers impact the transport processes in the stable ABL and whether boundary layer regimes can improve their prediction and (2) which impact the non-local variations in surface properties have on the local heat flux.

For a general overview, a surface energy balance was computed, including horizontal heat advection relying on spatial FODS observations. Furthermore, a routine was developed to determine the intensity of the submeso-scale phenomenon of periodic wind-directional changes termed meandering. Boundary layer regimes were then formed based on wind speed and direction, longwave incoming radiation, static stability and the meandering intensity. A multi-resolution decomposition was performed on the FODS observations of temperature and wind speed to investigate the scale-dependent power of the observed processes. To evaluate non-local influences on the vertical sensible heat flux  $Q_H$ , the respective flux was modeled based on solely local drivers according to the Monin-Obukhov similarity theory and compared to the measured flux. Lastly, a case study on a solitary submeso-scale motion was conducted.

The investigated conditions of polar night were dominated by stable stratification and a variety of non-stationary, submeso-scale processes, which the FODS setup proved capable to resolve. Meandering occurred as interaction of competing katabatic flows of different origin and relied on periods of calm winds. The results showed an increasing importance of submeso-scale processes with decreasing wind speed and decreasing longwave incoming radiation.  $Q_H$ 's strongest individual determinant was wind speed, but the flux appeared to depend on a complex interplay: The flux magnitude increased with high wind speeds, steep vertical temperature gradients as well as strong meandering and clear skies. Non-local surface properties had strongest influence on the local flux during clear skies and weak flows, especially of katabatic origin.

Concluding, this work sheds light on several site-specific as well as general drivers of submeso-scale processes and non-local influences, many of which are closely tied to the surrounding orography and surface heterogeneity. It thereby contributes to a better comprehension of processes in the nighttime Arctic ABL.

---

# Zusammenfassung

Die Triebkräfte für den Transport von Energie, Impuls und Materie durch die atmosphärische Grenzschicht sind Schlüsselgrößen für unser Verständnis und unsere Vorhersage atmosphärischer Prozesse auf allen Skalen. Dennoch fehlt uns ein umfassendes Verständnis dieser Triebkräfte für einen weiten Bereich an Bedingungen, in welchen die Abwesenheit von Sonneneinstrahlung zu fehlender konvektiver Durchmischung führt und die Grenzschicht stabil geschichtet ist. Dies gilt insbesondere für die anhaltende Dunkelheit in der arktischen Polarnacht. Die unter diesen Bedingungen relevanten Prozesse entsprechen nicht den für die konvektive Grenzschicht allgemein anerkannten Ähnlichkeitsbeziehungen und herkömmliche Messverfahren, die sich auf Punktmessungen stützen, scheiternd daran, diese Prozesse abzubilden.

Das NY-Ålesund Turbulence Fiber Optic eXperiment (NYTEFOX) auf Spitzbergen hatte das Ziel, die Beobachtungsbasis für diese Prozesse, die als submeso-skalige Phänomene zusammengefasst werden, zu verbessern. Dafür wurden klassische Beobachtungssysteme mit einem großen Aufbau der neuartigen Glasfaser-Messtechnik (FODS für fiber-optic distributed sensing) kombiniert, die kontinuierliche Beobachtungen sowohl in der Zeit als auch im Raum ermöglicht. Die Forschungsfragen dieser Arbeit lauteten: (1) Welche Faktoren die Transportprozesse in der stabilen Grenzschicht beeinflussen und ob Grenzschichtregime ihre Vorhersage verbessern können und (2) welchen Einfluss die nichtlokalen Variationen der Oberflächeneigenschaften auf den lokalen Wärmefluss haben.

Für einen allgemeinen Überblick wurde eine Oberflächenenergiebilanz berechnet, einschließlich der horizontalen Advektion fühlbarer Wärme auf der Grundlage räumlicher FODS-Beobachtungen. Darüber hinaus wurde eine Routine zur Bestimmung der Intensität des submeso-skaligen Phänomens periodischer Windrichtungsänderungen, des so genannten Mäandrierens, entwickelt. Die Grenzschichtregime wurden gebildet auf Grundlage der Windgeschwindigkeit und Windrichtung, der langwelligen Einstrahlung, der statischen Stabilität und der Intensität des Mäandrierens. Eine mehrskalige Zerlegung (multi-resolution decomposition) der FODS-Messungen von Temperatur und Windgeschwindigkeit wurde durchgeführt, um die skalenabhängige Energie der beobachteten Prozesse zu untersuchen. Zur Bewertung der nichtlokalen Einflüsse auf den vertikalen fühlbaren Wärmestrom  $Q_H$  wurde der entsprechende Fluss auf der Grundlage ausschließlich lokaler Einflüsse nach der Monin-Obukhov-Ähnlichkeitstheorie modelliert und mit dem gemessenen Fluss verglichen. Abschließend wurde eine Fallstudie über ein einzelnes submeso-skalige Phänomen durchgeführt.

Die untersuchten Bedingungen in der Polarnacht waren geprägt von einer stabilen Schichtung und einer Vielzahl von nicht-stationären, submeso-skaligen Prozessen, die mit dem FODS-Aufbau beobachtet werden konnten. Mäandrieren trat als Interaktion konkurrierender katabatischer Strömungen unterschiedlichen Ursprungs auf und bedurfte windstillen Perioden. Die Ergebnisse zeigen zudem, dass die Bedeutung submeso-skaliger Prozesse mit abnehmender Windgeschwindigkeit und abnehmender langwelliger Einstrahlung zunimmt. Der stärkste individuelle Bestimmungsfaktor für  $Q_H$  war die Windgeschwindigkeit, der Fluss schien jedoch von einem komplexen Zusammenspiel abzuhängen: Der Betrag des Flusses nahm mit hohen

---

Windgeschwindigkeiten, steilen vertikalen Temperaturgradienten sowie starkem Mäandrieren und klarem Himmel zu. Der nichtlokale Einfluss von Oberflächeneigenschaften auf den lokalen Wärmestrom war bei klarem Himmel und schwachen Winden, insbesondere katabatischem Ursprungs, am größten.

Diese Arbeit gibt Aufschluss über mehrere standortspezifische sowie allgemeine Triebkräfte submeso-skaliger Prozesse und nichtlokale Einflüsse, von denen viele eng mit der umgebenden Orographie und Oberflächenheterogenität verbunden sind. Sie trägt damit zu einem besseren Verständnis der Prozesse in der nächtlichen arktischen Grenzschicht bei.

# Contents

<b>Abstract</b>	<b>I</b>
<b>Zusammenfassung</b>	<b>III</b>
<b>List of figures</b>	<b>VII</b>
<b>List of tables</b>	<b>XVII</b>
<b>List of abbreviations</b>	<b>XIX</b>
<b>List of symbols</b>	<b>XXI</b>
<b>1. Introduction</b>	<b>1</b>
1.1. Background on stable boundary layers . . . . .	1
1.2. Objectives . . . . .	6
<b>2. Methods</b>	<b>9</b>
2.1. Site description . . . . .	9
2.2. Setup . . . . .	10
2.3. Feasibility . . . . .	13
2.4. Data processing . . . . .	13
2.4.1. Fiber-optic distributed sensing . . . . .	13
2.4.1.1. Temperature . . . . .	13
2.4.1.2. Wind speed . . . . .	14
2.4.2. External turbulence measurements . . . . .	16
2.4.3. Data correction . . . . .	16
2.5. Analysis . . . . .	17
2.5.1. Radiation and energy balance . . . . .	17
2.5.2. Flux-gradient-similarity . . . . .	20
2.5.3. Defining boundary layer regimes . . . . .	20
2.5.4. Detecting meandering . . . . .	24
2.5.5. Multi-resolution decomposition . . . . .	26
<b>3. Results and discussion</b>	<b>27</b>
3.1. General characteristics . . . . .	27
3.1.1. Air temperature and wind speed . . . . .	27
3.1.2. Radiation and energy balance . . . . .	29
3.2. Boundary layer regimes (RQ 1) . . . . .	32
3.2.1. Topography as wind determinator (H 1.1) . . . . .	32
3.2.2. Wind speed and cloud cover as proxy for submeso-scale motions (H 1.2)	36
3.2.3. Occurrence and generation of meandering (H 1.3) . . . . .	40
3.2.4. Varying influence of local topography (H 1.4) . . . . .	44

3.2.5. Drivers of sensible heat flux (H 1.5) . . . . .	49
3.3. Non-local drivers (RQ 2) . . . . .	53
3.3.1. Non-local influence and wind speed and direction (H 2.1) . . . . .	55
3.3.1.1. Monin-Obukhov similarity theory (MOST) . . . . .	55
3.3.1.2. Horizontal advection . . . . .	57
3.3.2. Non-local influence and cloud cover (H 2.2) . . . . .	59
3.4. Case study: soliton . . . . .	62
<b>4. Conclusions</b>	<b>65</b>
<b>Acknowledgements</b>	<b>69</b>
<b>Bibliography</b>	<b>71</b>
<b>A. Additional figures</b>	<b>81</b>
A.1. To methods . . . . .	81
A.2. To results and discussion . . . . .	84
A.2.1. Temperature by wind direction . . . . .	98
<b>Declaration of authorship</b>	<b>103</b>

# List of Figures

1.1.	Schematic plot of turbulence spectra, adapted from Foken (2017), originally from Lumley and Panofsky (1964). The range from $10^{-5}$ to $10^{-3}$ Hz is usually called meso-turbulence while everything $>10^{-3}$ Hz is micro-turbulence. Submeso-scale motions take place in the transition, between $10^{-4}$ and $10^{-1}$ Hz, which in this depiction is overlapping with both micro- and meso-turbulence. . . . .	5
2.1.	a) shows the location of Ny-Ålesund in the Kongsfjord (Copyright ©Norwegian Polar Institute). The arrows highlight the location of the Zeppelin mountain and Brøgger glacier, to which will be referred later on. The red rectangle marks the section displayed in b), which is a hillshade of a digital elevation model (DEM) published by Boike et al. (2018). The hillshade was compiled by Alexander Schulz. The setup is marked as red polygon, the black areas indicate missing data. . . . .	9
2.2.	Schematic setup (top panel) and picture of the setup (bottom panel) from the Zeppelin Mountain in the south (photo credit: Harald Sodemann). The fiber-optic array had a length of 700 m. The letters refer to the locations of the fiber-optic distributed sensing (FODS) device (a); the road crossings (b, c, g, h); the 10 m towers (d, e, i), and the minisodar (f). The letters a–i refer to the same elements in both panels. . . . .	11
2.3.	Photographs of the support structures of the metal-encased optical fibers: (a) clamping fixtures at each transects ends to tension the fibers. A metal wire was wrapped around the fiber, additionally secured by clamping screws, acting as an anchor point for tensioners commonly used for pasture fences. (b) tripods along the transects to support the fibers which were clamped in incised blocks of Styrofoam®. (c) bottom and (d) top mounts for fiber profiles on the telescoping towers. Rims of scooter wheels were used at the top to reduce the attack surface for winds while discs of acrylic glass served as mounts at the bottom, where the fibers were kept tight by clamping screws. Photo credit for (a), (b) and (c): Irene Suomi. . . . .	12
2.4.	Map of interpolated temperatures based on all horizontal temperature readings by the optical fiber for 2 min on 26.02.2020. The spatial resolution is 5x5 m. The colored points are the original readings, dark blue points mark the locations of the ultrasonic anemometers (USAs). The black square shows the footprint of the reference plane for estimating $Q_A$ . Temperatures are interpolated for all black points to calculate gradients while wind components are interpolated for the location of the orange rings. . . . .	19
2.5.	Friction velocity $u_*$ over wind speed on log axis recorded by the ultrasonic anemometers (USAs) at all towers, covering the whole measuring period (26.02. – 10.03.2020). Colored lines are bin averages (method: median) for the respective tower of equal width in log space. The dashed line visualizes the wind speed threshold of $2.5 \text{ ms}^{-1}$ . . . . .	23

2.6.	Density distribution of wind direction $\varphi$ recorded by the ultrasonic anemometer (USA) at the EDDY tower (latter ‘e’ in Fig. 2.2) with a perturbation time scale of 2 min. The plot covers the whole measuring period from 26.02. – 10.03.2020. The direction sectors for regime categorization (see Sect. 2.5.3) are expressed by colors and sector names ( <i>NE</i> , <i>SE</i> , <i>SW</i> and <i>NW</i> ) according to the sectors main direction. The labeled vertical lines depict the sector boundaries. . . . .	23
2.7.	Distribution of $\Delta\varphi$ calculated with a maximum $\Delta t$ of 4 min (see Sect. 2.5.4). The top panel shows only weak-wind data with $U \leq 2.5 \text{ m s}^{-1}$ while the bottom panel shows all data with higher wind speeds. The orange lines are the density functions and the green lines the normal distribution. The blue solid lines show a students t-distribution fitted to the respective data while the dashed lines are the related cumulative density. The respective fit parameters are listed under ‘t dist. params.’. The grey vertical lines mark the 5 <sup>th</sup> and 95 <sup>th</sup> percentile with the respective $\Delta\varphi$ values listed as interpercentile range (IPR). . . . .	25
3.1.	a) temperature at 2.1 m above ground level (a.g.l.) and b) wind speed at 2.5 m a.g.l. recorded by slow response sensors at Alfred Wegener Institute for Polar and Marine Research (AWI)’s eddy covariance (EC)-station for the whole measuring period (26.02. - 10.03.2020). Data were collected at 0.5 Hz, aggregated to 10 min. . . . .	27
3.2.	Wind speed $U$ (a), wind direction $\varphi$ (b) and vertical wind direction change (c) across height $z$ for the whole measuring period (26.02. - 10.03.2020). Data are measured by the sound detection and ranging (SODAR) (latter ‘f’ in Fig. 2.2), vertically aggregated to a resolution of 5 m and temporally averaged to 10 min. White areas indicate missing data due to an insufficient signal. While wind speeds ranged up to almost $23 \text{ m s}^{-1}$ the range displayed in (a) is limited to $15 \text{ m s}^{-1}$ for better distinguishability of lower velocities. The vertical wind direction change in (c) is computed as difference between running block differences of 20 m height. Blue colors indicate a clockwise directional change with increasing height while red represents counter-clockwise turns. . . . .	28
3.3.	Radiation data recorded by the baseline surface radiation network over the whole measuring period (26.02. - 10.03.2020). a) shows the radiation balance with shortwave incoming radiation ( $K \downarrow$ ), the shortwave reflex radiation ( $K \uparrow$ ), incoming and outgoing longwave radiation ( $I \downarrow$ and $I \uparrow$ ) and the net radiation ( $Q_S^*$ ). b) displays the shortwave and longwave net radiation, supplemented by $Q_S^*$ . The data fulfill the sign convention of positive fluxes away and negative towards the surface and are aggregated from 1 min to 60 min. . . . .	30

- 3.4. Time series of the surface energy balance (see Eq. 2.5) for the whole measuring period (26.02. - 10.03.2020). The components are net radiation  $Q_S^*$ , turbulent sensible and latent heat flux  $Q_H$  and  $Q_E$ , respectively, soil heat flux  $Q_G$  and horizontal advection of sensible heat  $Q_A$ , calculated according to equation 2.4. The turbulent quantities were computed with 10 min perturbation time scale and  $Q_A$  was calculated on a temporal resolution of 2 min. All other quantities were recorded with 1 min resolution. All time series were then aggregated to a 60 min resolution on which the residual term  $\epsilon_m$  was computed according to equation 2.6. The gaps in  $Q_E$  and  $\epsilon$  on 01.03. and 02.03.2020 are caused by instrument failure, marked by the light-grey vertical bars. The data fulfill the sign convention of positive fluxes away from and negative towards the surface. . . . . 30
- 3.5. Horizontal advection of sensible heat  $Q_A$  (see Eq.2.4), against (a) the residual of the surface energy balance  $\epsilon$  (see Eq. 2.2) and (b) the modified residual  $\epsilon_m$  (see Eq. 2.6) from which  $Q_A$  is excluded. The contour lines depict the point density while the blue solid lines are bin medians with a bin width of 300 data points The black, dashed line is the 1:1 relation.  $n$  represents the sample size, which covers the whole measurement period from 26.02. until 10.03.2020 with a temporal resolution of 2 min. . . . . 32
- 3.6. 2D histogram of wind speed and direction recorded by the ultrasonic anemometer (USA) at the EDDY tower, covering the whole measuring period (26.02. - 10.03.2020). The pixel size is  $x = 8^\circ$  and  $y = 0.25 \text{ m s}^{-1}$ . The color indicates the percentage of total with a distance between contour lines of 0.1%. The dashed line visualizes the wind speed threshold of  $2.5 \text{ m s}^{-1}$  (see Sect. 2.5.3). . . . . 33
- 3.7. Cumulative barplot of the occurrence of all boundary layer regimes (Sect. 2.5.3) that occur at least twice within the measuring period (for all regimes, see App. A.13). This covers 188 of the 223 windows (84%) and 32 out of 960 possible regimes. The numbers above the bars as well as the grayscale indicate the number of windows for the respective regime. The numbers below the x-axis represent the regime categories as listed in table 2.1 where 0 indicates that no category covered at least 90% of the respective window. The integers stand for wind speed  $U$ , wind direction  $\varphi$ , longwave downwelling radiation  $I \downarrow$ , static stability *st.stab* and meandering intensity *IPR*. . . . . 34
- 3.8. Power spectra of fiber-optic distributed sensing (FODS) temperature (a to d) and wind speed (e to h), combined for all horizontal fiber transects except between latter (a) and (d) in figure 2.2. The data are conditionally sampled by regimes with the respective regimes categories according to table 2.1 stated by each plot's title: The parameters (wind speed, wind direction, longwave downwelling radiation, static stability and meandering intensity) are separated by hyphens. 'a' refers to all categories (no sub-sampling), two digits to two categories. Hence, the rows subset by wind speed (1 = weak vs. 2 = strong) and the columns by longwave downwelling radiation (1 = weak vs. 23 = medium and strong). The variance on the y-axis is plotted logarithmically, the x-axis shows the dyadic multi-resolution decomposition (MRD) modes. The colored lines are the variances of single MRD windows, colored chronologically to reveal temporal effects. The bold line connects the medians of each mode. . . . . 38

3.9.	Spatially aggregated Pearson correlation coefficients $r_p$ for the fiber-optic distributed sensing (FODS) temperature observations of the transect OBSE-EDDY by separation distance and for the different multi-resolution decomposition (MRD) modes. The regime encoding is as described below figure 3.8. Absolute $r_p$ is plotted for weak wind and weak longwave downwelling radiation (a) while for medium to high radiation and weak (b) as well as strong winds (c) the correlation is plotted as ratio: $r_p$ of the respective regime divided by $r_p$ of a. . . . .	39
3.10.	Density histogram of wind directions for all regime windows with meandering category 1 to 4 (see Tab. 2.1) in sub-figure a to d respectively. Directions are recorded by an ultrasonic anemometer at the EDDY tower with a perturbation time scale of 2 min. Colors denote the wind direction sectors, also listed in table 2.1 while $n$ is the number observations in each sub-figure. . . . .	42
3.11.	Time series of wind direction $\varphi$ on the 26/27.02.2020 (a) and 29.02.2020 (b). Directions have a temporal resolution of 2 min and were recorded by the ultrasonic anemometer at the EDDY tower. Wind direction sectors are marked by horizontal, meandering category by vertical colored bars, visible at the top and bottom. . . . .	43
3.12.	Temperature deviation from the spatial average ( $\hat{T}$ ) for the fiber-optic distributed sensing transect from the EDDY tower to the BSRN tower. The grey areas mark the interquartile range (IQR) while the solid line is the temporal average. a) covers all time windows with weak winds ( $U \leq 2.5 \text{ m s}^{-1}$ ), b) all with strong winds ( $U > 2.5 \text{ m s}^{-1}$ ). The gaps show where the transect crossed two roads and no data are available while the vertical grey bar marks the fiber section crossing an old railroad embankment running in a shallow, snow-filled indentation. . . . .	45
3.13.	Pearson correlation coefficients $r_p$ between the EDDY tower (left column) and BSRN tower (right column) and all bins along the fiber-optic distributed sensing transect between those towers. Correlations for separate multi-resolution decomposition modes are represented by separate lines. a) to d) show correlations of temperature, e) to h) of wind speed data along the fiber-optic cable. The labels indicate whether all time windows with weak winds ( $U \leq 2.5 \text{ m s}^{-1}$ ) or strong winds ( $U > 2.5 \text{ m s}^{-1}$ ) are included as well as their respective number $n$ . The spatial gaps and the vertical grey bar at around 100 m are explained in figure 3.12. . . . .	47
3.14.	Pearson correlation coefficients $r_p$ as explained in figure 3.13 for the transect from EDDY to OBSE (left column) and EDDY to BSRN (right column). The first row includes all time windows with weak winds ( $U \leq 2.5 \text{ m s}^{-1}$ ) from the SW-sector (see Tab. 2.1) while the second contains all other weak-wind windows. The gaps and vertical bar in the right column are as described in figure 3.12. The grey bar in the left column marks where the railroad track crosses the transect EDDY-OBSE. . . . .	48

- 3.15. Scatter plot of the sensible heat flux  $Q_H$  vs (a) wind velocity, (b) friction velocity, (c) wind direction, (d) longwave downwelling radiation, (e) static stability and (f) the meandering indicator interpercentile range (see Sect. 2.5.4). (a) to (e) are based on values aggregated to 2 min. (f) is based on the multi-resolution decomposition (MRD) windows with a length of 77 min (see Sect. 2.5.3), determining the temporal resolution for IPR. The y-axis is set so that the 0.25<sup>th</sup> to 99.75<sup>th</sup> percentile of the 2 min  $Q_H$  is shown, cutting off extreme outliers. Data points are colored by wind speed with (a) serving as reference. The black lines show bin averages with widths of 300 values for (a) to (e) and 20 for (f). The red lines show regression models, which are linear for (a) and (b) and logarithmic for (f), with the  $r^2$  and model formula printed in the plot. The vertical dashed line in (a) marks the wind speed threshold of  $2.5 \text{ m s}^{-1}$  (see Sect. 2.5.3). 50
- 3.16. Scatter plot of the buoyancy flux  $Q_H$  vs the wind velocity based on 2 min statistics. The points are colored by the wind direction regimes 1 to 4 according to table 2.1.  $n$  is the number of observations per class. The solid lines show bin averages with widths of 300 values for each direction category while the dashed line marks the wind speed threshold of  $2.5 \text{ m s}^{-1}$  derived in section 3.1.1. The plot area covers the mid 99.5 % of  $Q_H$ . . . . . 51
- 3.17. For each of the 32 regimes (see Sect. 2.5.3) that occur at least twice during the measurement campaign: (a) The median sensible heat flux  $Q_H$  for the three ultrasonic anemometers (USAs) at the corners of the fiber-optic distributed sensing (FODS) array (colored points) as well as the median of all USAs (black points). The gray area marks the interquartile range (IQR) (the mid 50 % of the data). (b) Pearson correlation coefficient  $r_p$  as median of the correlations of all windows within the respective regime, for each USA (colored points) as well as all data (black points). The regimes are ordered by median  $Q_H$ , the regime categories on the x-axis refer to table 2.1 with zero indicating that no single category occurred during at least 90 % of the respective regime. The points are connected by lines for better lucidity, not indicating any conditions between the regimes. . . . . 52
- 3.18. Scatterplot of the sensible heat flux  $Q_H$  modeled with Monin-Obukhov similarity theory (MOST) and measured by the ultrasonic anemometer (USA) at the BSRN tower. The contour lines represent the density of points. The dashed line shows the 1:1 relationship, while the blue solid line depicts a least rectangles linear regression with the model parameters as well as the sample size printed top left. The temporal resolution is 2 min and the plot covers the whole campaign period from 26.02.2020 until 10.03.2020. . . . 54
- 3.19. Scatterplot of the difference between measured and modeled sensible heat flux  $Q_H$  (see Fig. 3.18) over wind speed  $U$ . The contour lines show the density of points, the violet solid line connects bin medians with a bin-width of 300. A linear model is represented by the dashed blue line with the model parameters as well as sample size printed top right. . . . . 56
- 3.20. Scatterplots as in figure 3.19 for different wind direction sectors (see Tab. 2.1). The grey solid lines are bin medians with the bin width being the sample size  $n$  divided by 15. 57

<p>3.21. Horizontal advection of sensible heat (<math>Q_A</math>, see Eq. 2.4) against wind velocity, recorded by the ultrasonic anemometer (USA) at the EDDY tower. Subfigures depict the four wind direction categories (see Tab. 2.1). The dashed vertical line marks the wind speed threshold of <math>2.5 \text{ m s}^{-1}</math>. The grey solid lines are bin medians with the bin width being the sample size <math>n</math> divided by 15. . . . .</p>	<p>58</p>
<p>3.22. Scatterplot of the difference between measured and modeled sensible heat flux <math>Q_H</math> (see Fig. 3.18) against wind speed <math>U</math>, measured by the ultrasonic anemometer (USA) at the EDDY tower. The subfigures a) to c) are subsets for the three regime categories for longwave downwelling radiation <math>I \downarrow</math>, explained in table 2.1 with the <math>I \downarrow</math>-range plotted top right. The contour lines show the density of points, <math>n</math> is the sample size of the respective subset. . . . .</p>	<p>60</p>
<p>3.23. Scatterplot of the horizontal advection of sensible heat <math>Q_A</math> according to section 2.5.1 against wind speed <math>U</math>, measured by the ultrasonic anemometer (USA) at the EDDY tower. The subfigures a) to c) are subsets for the three regime categories for longwave downwelling radiation <math>I \downarrow</math>, explained in table 2.1 with the <math>I \downarrow</math>-range plotted top right. The contour lines show the density of points, <math>n</math> is the sample size of the respective subset. . . . .</p>	<p>61</p>
<p>3.24. Observations of the fiber-optic distributed sensing (FODS) and ultrasonic anemometer (USA) setup on 05.03.2020 from 16:40 to 16:55. (a) shows wind speed <math>U</math> and direction <math>\varphi</math> recorded by the USA at the EDDY tower with a temporal resolution of 30 s. The dashed line marks the orientation of the horizontal fiber in (b) and (c) (<math>244^\circ</math>) while the dotted line is the direction orthogonal to said fiber (<math>154^\circ</math>). (b) and (c) display the first 108 m of horizontal fiber from the EDDY tower towards the BSRN tower where (b) shows temperatures and (c) the wind component orthogonal to the fiber. The horizontal stripes in (c) are artifacts of fiber holders and strips of streamer, added for safety reasons in the field. The three most protruding artifacts were already removed by linear spatial interpolation. (d) displays a temperature profile next to the EDDY tower, measured with a high resolution fiber optic column. The lowest 0.23 m with temporally homogeneous and relatively warm temperatures were within snow. The dashed horizontal line marks the approximate height at which the horizontal fibers in (b) and (c) are mounted. . . . .</p>	<p>63</p>
<p>3.25. Time series of wind speed <math>U</math> (blue line) and sensible heat flux <math>Q_H</math> (orange line) for the 05.03.2020 from 16:40 to 16:55. The period corresponds to figure 3.24. Observations are made by ultrasonic anemometer (USA) at the EDDY tower with a perturbation time scale of 30 s. The grey bar marks the time where the solitary motion displayed in figure 3.24 reaches the EDDY tower. . . . .</p>	<p>64</p>

A.1.	Average wind speed $U$ of the ultrasonic anemometers (USAs) for the whole campaign period (top) and absolute change in wind speed between two averaging blocks ( $ \Delta U_{block} $ ) of 60 min length, shifted along the time series (bottom). The dashed horizontal line marks a threshold value of 1.4K. Changes above this threshold, highlighted as red sections of the curve, were used as indicators for strong wind speed changes. The time series was cut into separate blocks for computation of fiber-optic distributed sensing (FODS) wind speeds at the maximum $dU/dt$ of each of these sections, marked by the light blue, vertical lines (see Sect. 2.4.1.2). . . . .	81
A.2.	Distribution of longwave incoming radiation $I \downarrow$ for the whole campaign period. Colors indicate the regime categories 1 to 4 as outlined in section 2.5.3). . . . .	82
A.3.	Boxplot of the maximum absolute changes in wind direction $\Delta\phi$ vs. different maximum time window lengths from 2 min to 16 min. The method is applied for 2 min wind direction data measured by the ultrasonic anemometer (USA) at the EDDY tower and covers all windows used for meandering detection (see Sect. 2.5.4). . . . .	82
A.4.	Histogram of wind-directional changes $\Delta\varphi$ , derived as outlined in section 2.5.4 for a 77 min long time window on 26.02.2020. The orange curve visualizes the smoothed density distribution of the directional changes while the green curve shows the density of a normal distribution based on the mean and standard deviation of the directional changes. The blue solid curve is the density of a students t-distribution fitted to the distribution of directional changes while the blue dashed curve is the cumulative density of this students t-distribution. The vertical grey bars indicate the 5 <sup>th</sup> and 95 <sup>th</sup> percentile of the students t-distribution, indicated by ‘thresh. = 5%’. The distributions fitting parameters (‘location’, ‘scale’ and ‘freed.’ for degrees of freedom) as well as the percentiles (‘ipr’ for interpercentile range) are listed below ‘t dist params.’. ‘dt’ sates the maximum time difference over which $\Delta\varphi$ was computed (see Sect. 2.5.4). . . . .	83
A.5.	Scatter plots of (a) the latent heat flux $Q_E$ and (b) the specific humidity $q$ vs wind direction $\varphi$ , measured by the eddy covariance (EC) station of the Alfred Wegener Institute for Polar and Marine Research (AWI) for the whole measuring period. The perturbation time scale is 10 min. The contour lines display the point densities. The ranges of the y-axes are slightly reduced for better distinguishability of values with small magnitude, cutting off some of the data points with very large magnitudes. . . . .	84
A.6.	Scatter plots of latent heat flux $Q_E$ over specific humidity $q$ , measured by the eddy covariance (EC) station of the Alfred Wegener Institute for Polar and Marine Research (AWI) for the whole measuring period. The perturbation time scale is 10 min. The contour lines display the point densities. The ranges of the x- and y-axes are slightly reduced for better distinguishability of values with small magnitude, cutting off some of the data points with very large magnitudes. . . . .	85
A.7.	Scatter plot of horizontal advection of latent heat $Q_A$ vs wind direction $\varphi$ , measured by the NYTEFOX EDDY tower for the whole measuring period. The temporal resolution is 2 min. The contour lines display the point densities. . . . .	85

A.8.	Scatter plot between the residual of the surface energy balance with ( $\epsilon$ , see Eq. 2.2) and without ( $\epsilon_m$ , see Eq. 2.6) horizontal advection of sensible heat. The temporal resolution is 2 min and $n$ is the sample size. The contour lines display the point densities. The dashed black line is the 1:1 relation while the solid blue line represents a linear model with the models slope $m$ and the respective $p$ -value as well as the squared person correlation coefficient $r^2$ . . . . .	86
A.9.	Scatter plot of the buoyancy flux $Q_H$ vs the regime parameters a) wind velocity, b) wind direction, c) long wave downwelling radiation, d) static stability and e) the meandering indicator interpercentile range (IPR) (see Sect. 2.5.3). The y-axis is set so that the 0.1 <sup>th</sup> to 99.9 <sup>th</sup> percentile are pictured, cutting off extreme outliers. Orange color marks the periods from 08.03.2020, 02:30 to 10:26 and 13:30 to 14:40 UTC. . . . .	87
A.10.	Scatter plot of the wind velocity $U$ (a) and friction velocity $u_*$ (b) vs static stability for the whole measuring period. The orange lines represents bin averages of 0.1 K ln m <sup>-1</sup> width. The contour lines depict the point density. . . . .	88
A.11.	Sonic temperature $T_s$ at Eddy tower for 07.03.2020, 22:00 to 08.03.2020, 17:00 UTC. The orange area marks the periods highlighted in A.9. The abrupt temperature drop explains the positive buoyancy flux $Q_H$ for the highlighted periods. . . . .	89
A.12.	ECMWF Reanalysis v5 (ERA5) for 08.03.2020, 07:00 UTC. Shading: 850 hPa wind speeds; vectors: 850 hPa wind vectors; contour lines: 850 hPa geopotential height (GPH) in meter. Plot by Dr. Alexander Schulz. . . . .	90
A.13.	Cumulative barplot of the occurrence of all occurring boundary layer regimes (Sect. 2.5.3) within the measuring period. This covers 67 out of 960 possible regimes. The numbers above the bars as well as the grayscale indicate the number of windows for the respective regime. The numbers below the x-axis represent the regime categories as listed in table 2.1 where 0 indicates that no category covered at least 90 % of the respective window. The integers stand for wind speed $U$ , wind direction $\varphi$ , longwave downwelling radiation $I \downarrow$ , static stability $st.stab$ and meandering intensity interpercentile range (IPR). Windows with identical number of occurrence are ordered by their regime category numbers. . . . .	91
A.14.	ECMWF Reanalysis v5 (ERA5) for 02.03.2020, 12:00 UTC. Shading: 850 hPa wind speeds; vectors: 850 hPa wind vectors; contour lines: 850 hPa geopotential height (GPH) in meter. Plot by Dr. Alexander Schulz. . . . .	92
A.15.	ECMWF Reanalysis v5 (ERA5) for 03.03.2020, 22:00 UTC. Shading: 850 hPa wind speeds; vectors: 850 hPa wind vectors; contour lines: 850 hPa geopotential height (GPH) in meter. Plot by Dr. Alexander Schulz. . . . .	93
A.16.	ECMWF Reanalysis v5 (ERA5) for 04.03.2020, 04:00 UTC. Shading: 850 hPa wind speeds; vectors: 850 hPa wind vectors; contour lines: 850 hPa geopotential height (GPH) in meter. Plot by Dr. Alexander Schulz. . . . .	94

- A.17. Power spectra of fiber-optic distributed sensing (FODS) temperature (a to d) and wind speed (e to h), combined for all horizontal fiber transects except between latter (a) and (d) in figure 2.2. The data are conditionally sampled by regimes with the respective regimes categories according to table 2.1 stated by each plot's title: The parameters (wind speed, wind direction, longwave downwelling radiation, static stability and meandering intensity) are separated by hyphens. 'a' refers to all categories (no sub-sampling), two digits to two categories. Hence, the rows subset by wind speed (1 = weak vs. 2 = strong) and the columns by longwave downwelling radiation (2 = medium vs. 3 = strong). The variance on the y-axis is plotted logarithmically, the x-axis shows the dyadic multi-resolution decomposition (MRD) modes. The colored lines are the variances of single MRD windows, colored chronologically to reveal temporal effects. The bold line connects the medians of each mode. . . . . 95
- A.18. Spatially aggregated temporal correlation coefficients of fiber-optic distributed sensing (FODS) temperature (a to d) and wind speed (e to h) against the separation distance for the fiber transect between the OBSE and EDDY tower ((d) and (e) in figure 2.2). The correlations are computed for time scales from 9 s to 77 min indicated by the colors, based on a multi-resolution decomposition (MRD). The data are conditionally sampled by regimes with the respective regimes categories according to table 2.1 stated by each plot's title: The parameters (wind speed, wind direction, longwave downwelling radiation, static stability and meandering intensity) are separated by hyphens. 'a' refers to all categories (no sub-sampling), two digits to two categories. Hence, the rows subset by wind speed (1 = weak vs. 2 = strong) and the columns by longwave downwelling radiation (1 = weak vs. 23 = medium and strong). . . . . 96
- A.19. Density histograms of temperature differences along all horizontal sections of the fiber-optic distributed sensing (FODS) setup with a temporal resolution of 9 s. Differences are calculated between block averages of 4.8 m width, shifted along the fiber. Results are shown for all regime windows with weak-winds and clear-sky conditions (top) as well as weak-wind and cloudy conditions (bottom). . . . . 97
- A.20. Density histograms of the maximum spatial temperature differences between the three USAs at the corners of the setup with a perturbation time scale of 2 min. Results are shown for all regime windows with weak-winds and clear-sky conditions (top) as well as weak-wind and cloudy conditions (bottom). . . . . 97
- A.21. Temperatures over wind direction, measured by an USA at the EDDY tower with a perturbation time scale of 2 min. (a) includes the period from 26.02.2020, 14:30 to 27.02.2020, 14:30, (b) covers the 29.02.2020. The periods match those of figure 3.11. The points are colored chronologically from white to black. The vertical colored bars visualize the wind direction sectors listed in table 2.1: NE-sector = 320 – 80, SE-sector = 80 – 170, SW-sector = 170 – 275 and NW-sector = 275 – 320. . . . . 98

A.22. Power spectra of fiber-optic distributed sensing (FODS) temperature, combined for all horizontal fiber transects except between latter (a) and (d) in figure 2.2. The data are conditionally sampled by regimes according to table 2.1. **a** only includes weak winds from the SW-sector down the slopes of the adjacent mountains and glaciers while **b** includes weak winds from all other sectors as well as periods with varying sectors. The variance on the y-axis is plotted logarithmically, the x-axis shows the dyadic multi-resolution decomposition (MRD) modes. The colored lines are the variances of single MRD windows, colored chronologically to reveal temporal effects. The bold line connects the medians of each mode. . . . . 99

A.23. Time series of the sensible heat flux  $Q_H$  for the whole campaign period. The black line displays the  $Q_H$  measured by the ultrasonic anemometer (USA) at the BSRN tower while the orange line is the  $Q_H$  modeled using Monin-Obukhov similarity theory (MOST) according to section 2.5.2. The measured flux is processed on a perturbation time scale of 2 min which is also the raw resolution of the modeled  $Q_H$ . A running mean of 60 min is then applied to both for improved clarity. . . . . 100

A.24. Point density of horizontal advection of sensible heat  $Q_A$  against the residual of the surface energy balance  $\epsilon$  (as in Fig. 3.5) for winds below (left) and above (right)  $2.5 \text{ m s}^{-1}$ , measured by the ultrasonic anemometer (USA) at the EDDY tower. The dashed line depicts the 1 : 1 relation. . . . . 101

A.25. Map of the south-western part of the fiber-optic distributed sensing (FODS) setup for two instants of time during the occurrence of a solitary submeso-scale motion (see Sect. 3.4) with the time stamp topleft. The broad colored bars display temperature along the fiber-optic cable at approximately 1 m a.g.l. while the bordering stripes show the wind speed component orthogonal to the fiber. The EDDY tower is located at the bottom left tip of the setup where the grey arrow shows the wind direction recorded by the ultrasonic anemometer (USA) mounted. The respective wind speed is written below. The underlying map is a hillshade based on a digital elevation model (DEM) published by Boike et al. (2018). . . . . 102

# List of Tables

2.1.	The regime parameters wind speed ( $U$ ), wind direction( $\varphi$ ), longwave incoming radiation ( $I \downarrow$ ), static stability and meandering and their categories applied to form boundary layer (BL) regimes. . . . .	21
2.2.	Explanation of the meandering categorization applied on windows of 77 min length according to section 2.5.4. . . . .	26
3.1.	Proportion of large differences between measured and modeled sensible heat flux $Q_H$ during weak winds ( $U \leq 2.5 \text{ m s}^{-1}$ ) and strong winds ( $U > 2.5 \text{ m s}^{-1}$ ) as well as by wind direction sectors during weak winds. The direction sectors are defined according to table 2.1. The first column states the threshold of the absolute difference. . . . .	55
3.2.	Proportion of large absolute horizontal advection of sensible heat $ Q_A $ during weak winds ( $U \leq 2.5 \text{ m s}^{-1}$ ) and strong winds ( $U > 2.5 \text{ m s}^{-1}$ ) as well as by wind direction sectors during weak winds. The direction sectors are defined according to table 2.1. The first column states the threshold of the absolute difference. . . . .	59
A.1.	Comparison of the $I \downarrow$ category of regimes with identical regime parameters for all variables except for $I \downarrow$ (see Sect. 2.5.3). ‘regime a’ and ‘regime b’ are the numbers of the compared regimes according to figure 3.17 while ‘cat. a’ and ‘cat. b’ are the respective $I \downarrow$ regime categories. The comparisons in the upper block show a lower magnitude of the sensible heat flux $Q_H$ for higher $I \downarrow$ which is inverted for the lower block. . . . .	99
A.2.	Comparison of the meandering category interpercentile range (IPR) of regimes with identical regime parameters for all variables except for IPR (see Sect. 2.5.3 and 2.5.4). ‘regime a’ and ‘regime b’ are the numbers of the compared regimes according to figure 3.17 while ‘cat. a’ and ‘cat. b’ are the respective IPR regime categories. The comparisons in the upper block show a higher magnitude of the sensible heat flux $Q_H$ for higher IPR which is inverted for the lower block. . . . .	101



# List of abbreviations

<b>ABL</b>	atmospheric boundary layer
<b>a.g.l.</b>	above ground level
<b>a.s.l.</b>	above sea level
<b>AWI</b>	Alfred Wegener Institute for Polar and Marine Research
<b>AWIPEV</b>	collaborative research station of AWI and IPEV
<b>BL</b>	boundary layer
<b>BSRN</b>	baseline surface radiation network
<b>CASES-99</b>	Cooperative Atmospheric Surface Exchange Study 1999
<b>CBL</b>	convective boundary layer
<b>DEM</b>	digital elevation model
<b>DTS</b>	distributed temperature sensing
<b>EC</b>	eddy covariance
<b>ECMWF</b>	European Centre for Medium-Range Weather Forecasts
<b>ERA5</b>	ECMWF Reanalysis v5
<b>ESSD</b>	Earth System Science Data
<b>FODS</b>	fiber-optic distributed sensing
<b>GPH</b>	geopotential height
<b>GPS</b>	global positioning system
<b>H</b>	hypothesis
<b>HPU</b>	heat pulse unit
<b>IPEV</b>	Institute Paul Emile Victor
<b>IPR</b>	interpercentile range
<b>IQR</b>	interquartile range
<b>LAF</b>	length along the fiber
<b>LASER</b>	light amplification by stimulated emission of radiation
<b>LOVE19</b>	Large-eddy Observatory Voitsumra Experiment 2019
<b>MOST</b>	Monin-Obukhov similarity theory
<b>MRD</b>	multi-resolution decomposition
<b>NYTEFOX</b>	NY-Ålesund Turbulence Fiber Optic eXperiment
<b>PE</b>	polyethylene
<b>RQ</b>	research question

<b>SBL</b>	stable boundary layer
<b>SCP</b>	Shallow Cold Pool Experiment
<b>SODAR</b>	sound detection and ranging
<b>USA</b>	ultrasonic anemometer

# List of symbols

symbol	explanation	unit
$c_f$	Specific heat capacity of a fiber-optic cable	(J kg <sup>-1</sup> K <sup>-1</sup> )
$c_p$	Specific heat capacity of air	(J kg <sup>-1</sup> K <sup>-1</sup> )
$f$	Frequency	(s <sup>-1</sup> )
$g$	Gravitational acceleration	(m <sup>2</sup> s <sup>-2</sup> )
$H_A$	Advective transport of sensible heat through a defined plane	(W m <sup>-2</sup> )
$I \downarrow$	Incoming longwave radiation	(W m <sup>-2</sup> )
$I \uparrow$	Outgoing longwave radiation	(W m <sup>-2</sup> )
$K \downarrow$	Incoming shortwave radiation	(W m <sup>-2</sup> )
$K \uparrow$	Shortwave reflex radiation	(W m <sup>-2</sup> )
$K_a$	Thermal conductivity of air	(W m <sup>-1</sup> K <sup>-1</sup> )
$L$	Obukhov length	(-)
$L_e$	Edge length of the footprint for computation of $Q_A$	(m)
$p$	Atmospheric pressure	(Pa)
$Pr$	Prandtl number	(-)
$P_s$	Heating rate	(W m <sup>-1</sup> )
$q$	Specific humidity	(kg kg <sup>-1</sup> )
$Q_A$	Horizontal advection of sensible heat	(W m <sup>-2</sup> )
$Q_E$	Latent heat flux	(W m <sup>-2</sup> )
$Q_G$	Ground heat flux	(W m <sup>-2</sup> )
$Q_H$	Sensible heat flux	(W m <sup>-2</sup> )
$Q_s^*$	Net radiation	(W m <sup>-2</sup> )
$Q_S$	Storage term	(W m <sup>-2</sup> )
$R_a$	Specific gas constant	(J kg <sup>-1</sup> K <sup>-1</sup> )
$r$	Radius	(m)
$RH$	Relative humidity	(%)
$r_P$	Pearson's correlation coefficient	(-)
$T$	Dry bulb temperature	(K or °C)
$\hat{T}$	Spatial temperature perturbation	(K or °C)
$T_h$	Temperature of a heated fiber-optic cable	(K)
$T_h$	Temperature of a unheated (reference) fiber-optic cable	(K)
$T_s$	Sonic temperature	(K or °C)
$TKE$	Turbulent kinetic energy	(m <sup>2</sup> s <sup>-2</sup> )
$U$	Wind speed	(m s <sup>-1</sup> )
$u$	Wind component from west to east	(m s <sup>-1</sup> )
$u_*$	Friction velocity	(m s <sup>-1</sup> )
$v$	Wind component from south to north	(m s <sup>-1</sup> )
$\nu_a$	Kinematic viscosity of air	(m <sup>2</sup> s <sup>-1</sup> )

symbol	explanation	unit
$\overline{w'T'}$	Sensible heat flux	(K s <sup>-1</sup> )
$z$	Height above ground	(m)
$\alpha_0$	Inverse Prandtl number	(-)
$\Gamma$	Atmospheric temperature gradient	(K m <sup>-1</sup> )
$\Delta$	Difference	(-)
$\epsilon$	Residual term of the energy balance	(W m <sup>-2</sup> )
$\epsilon_m$	Modified residual term of the energy balance: without $Q_A$	(W m <sup>-2</sup> )
$\epsilon_s$	Surface emissivity	(-)
$\zeta$	Stability estimate $z/L$	(-)
$\Theta$	Potential temperature	(K or °C)
$\kappa$	Von Kármán constant	(-)
$\pi$	Ratio of a circle's circumference to its diameter	(-)
$\rho$	Density	(kg m <sup>-3</sup> )
$\sigma$	Standard deviation	(-)
$\sigma^2$	Variance	(-)
$\sigma_S$	Stefan-Boltzmann constant	(W m <sup>-2</sup> K <sup>-4</sup> )
$\varphi$	Wind direction	(°)
$\varphi_H(\zeta)$	Universal function for sensible heat	(-)

# 1. Introduction

Predictions of atmospheric conditions have become essential for a wide range of our everyday life. Weather forecasts are vital to the supply of societies' basic needs such as agricultural food production and logistics as well as protection against natural calamities. Predictions on larger temporal as well as spatial scales have gained increasing importance, shedding light on the drivers and potential courses of global climate change, affecting transnational political and societal development.

A key quantity for such models are the processes responsible for exchange of heat and matter between the surface and the atmosphere, emphasizing the critical role of the ABL. The exchange processes within the ABL are well understood and described by theories for convective conditions where the boundary layer (BL) is mixed by sufficiently strong turbulence. This turbulence is either generated by shear forces during strong enough winds or buoyancy-driven convection, where the soil is warmed by solar radiation, warming the lowermost layer of air, which then rises due to the resulting reduction of its density (Vila-Guerau de Arellano et al., 2015).

However, we lack this kind of comprehensive process understanding for conditions where turbulent convection breaks down and the BL becomes stably stratified, no longer fulfilling the similarity assumptions confirmed for the convective boundary layer (CBL) (Sun et al., 2020; Thomas, 2011; Sun et al., 2012; Pfister et al., 2021a; Mahrt, 2010; Acevedo et al., 2014). With convection being closely tied to solar radiation, this largely affects polar night in the Arctic where daylight is absent for several months.

This lack of process understanding for a large portion of Arctic conditions gains increasing importance on the background of so-called Arctic amplification (Cohen et al., 2014; Overland et al., 2016), describing the extraordinary sensitivity of the Arctic to climate change. Temperatures in the Arctic are rising faster than the global average (Solomon, 2007) with an increase per decade of  $1.3 \pm 0.7$  K for the average annual temperature and even  $3.1 \pm 2.4$  K for the winter months in Ny-Ålesund, Svalbard for the period from 1993 to 2013 (Maturilli et al., 2015). While several contributing mechanisms, such as the snow/sea ice–albedo feedback (Curry et al., 1995; Screen and Simmonds, 2010) are known, summarized e.g. by Maturilli et al. (2015), climate predictions still suffer from largest uncertainties for polar regions (Holtslag et al., 2013; Davy and Esau, 2014; Stocker et al., 2014; Cohen et al., 2014). Gaining improved understanding of the mechanisms dominating exchange processes in the Arctic stable boundary layer (SBL), hence, is of the essence.

## 1.1. Background on stable boundary layers

The density of air varies with its humidity and potential temperature, which accounts for adiabatic warming or cooling of air with varying density. Vertical variations in those parameters, hence, result in a density stratification. In consequence, the density of a vertically allocated

parcel of air may differ from the surrounding air density, exerting a buoyancy force on the parcel. If this force has an accelerating effect on the parcel, it drives convective mixing and the environment is referred to as statically unstable while it is called statically neutral when no force acts on the parcel. If the density, however, decreases with height, e.g. due to a vertically increasing potential temperature, the buoyancy force decelerates the parcel's movement, forcing it back to its original location. This situation is called statically stable (Arya, 2001).

The vertical temperature gradient is, to a large extent, determined by the balance of radiation components at the surface. These components of the surface radiation balance the shortwave global radiation and reflected radiation ( $K \downarrow$ ,  $K \uparrow$ ) as well as incoming and outgoing longwave radiation ( $I \downarrow$ ,  $I \uparrow$ ). The net radiation  $Q_S^*$  then results from

$$Q_S^* = K \downarrow + K \uparrow + I \downarrow + I \uparrow \quad (1.1)$$

(Foken, 2017, Ch. 1.4.1).

During the absence of sunlight this radiation balance is dominated by longwave radiation with outgoing energy transfer usually exceeding the incoming. The difference gets especially pronounced during clear skies, where no clouds re-emit part of the outgoing longwave radiation back to the surface. This radiation imbalance results in a radiative cooling of the surface and the near-surface air (Arya, 2001), causing an increase of potential temperature with height and hence a ground-based layer of statically stable air (Stull, 1988).

Winds aloft may accelerate, forming a surface-decoupled, so-called low-level jet, whereas, in the absence of a strong synoptic forcing, the air inside this SBL calms down (Stull, 1988). But while the classic theories now predict turbulence to be totally suppressed by dynamic stability (Monin and Obukhov, 1954), more recent observations demonstrated that turbulent motions are maintained even for extremely stable conditions (Acevedo et al., 2007; Mahrt, 2010; Mahrt et al., 2013; Zeeman et al., 2015). The characteristics of these motions, however, differ greatly from those occurring under convective conditions:

Daytime (micro-)turbulence, scaling with surface stress, can be assumed to be a stochastic, random process with a coherent space-time scaling. The spatial extent of a turbulent element, termed ‘eddy’, corresponds to its duration (Foken, 2017), fulfilling Taylor’s hypothesis of frozen turbulence (Taylor, 1938). The scale of these eddies is ranging on the order of centimeters to several meters and milliseconds to tens of seconds (see Fig. 1.1).

The motions dominating the weak-wind SBL are on larger scales, ranging from less than a minute up to more than 1 h in time and from horizontal extends of several meters up to 2 km (see Fig. 1.1 and Mahrt et al., 2009; Mahrt, 2014; Thomas et al., 2012). However, since, in contrast to classic turbulent eddies, the shape of these motions is not necessarily isotropic but often dominated by two-dimensional modes, the vertical depth may still be only a few meters (Mahrt et al., 2009). As their scales are still below what is typically referred to as the mesoscale, these phenomena are termed submeso-scale motions (Anquetin et al., 1998; Mahrt et al., 2009).

Being a collective term, submeso-scale motions cover a broad variety of phenomena, such as turbulence intermittency (Sun et al., 2012; Mahrt et al., 2013), microfronts, more recently termed thermal submesofronts (Mahrt et al., 2009; Kang et al., 2015; Pfister et al., 2021a,b),

solitons and propagating wave modes (Mahrt, 2014; Mahrt and Thomas, 2016), katabatic flows or density currents (Mahrt et al., 2001; Sun et al., 2002) and meandering of the wind direction (Etling, 1990; Anfossi et al., 2005; Belušić and Mahrt, 2008; Lang et al., 2018).

While these submeso-scale motions seem to occur under all conditions including the CBL, their impact is limited primarily to the weak-wind SBL, where they are not superimposed by turbulence (Anfossi et al., 2005; Mahrt, 2010). In this range, turbulence depends very little on stratification and dynamic stability (Mahrt and Thomas, 2016), hence, no critical Richardson number (as a measure for dynamic stability) corresponds to a complete collapse of turbulence. In simulations turbulent exchange close to the surface is usually parametrized by use of Monin-Obukhov similarity assumptions (Monin and Obukhov, 1954). However, all physical similarity relationships are influenced by non-turbulent, submeso-scale motions, whose energy distribution varies substantially between locations (Vickers and Mahrt, 2007; Mahrt et al., 2009), resulting in varying scaling parameters from site to site (Acevedo et al., 2014). Hence, the universal similarity expressions do not account for the specific flux contribution of non-turbulent motions in the submeso-scale range.

Spatial heterogeneity of a surface introduces further influencing factors on fluxes that the parametrizations, based on local parameters, do not account for. In a heterogeneous environment the actual flux might not be in equilibrium with the local properties for various reasons (Li et al., 2012). One such reason is the formation of internal BLs at transitions between surfaces with different properties, that might cause the turbulent processes of advected air to lack full adjustment to the new surface (McNaughton and Laubach, 1998). This effect increases with stratification and the associated reduction of mixing, since surface turbulence takes an increasing amount of time to get mixed to the height of e.g. a flux measurement and vice versa. Hence, the surface properties determining the flux at a given height have an increasing upstream distance to the point of observation with increasing stability to the point, where the observed flux is totally decoupled from the underlying surface, violating the assumption of local similarity (Optis et al., 2016).

Large differences between observed fluxes and fluxes modeled according to Monin-Obukhov similarity theory (MOST), hence, point towards non-turbulent modes of possibly non-local origin, serving as diagnostic tool to identify respective periods, as will be shown later in this thesis.

For atmospheric models, however, these non-represented contributions pose a problem. In current simulations, turbulence in the SBL is artificially enhanced in order to reduce the mismatch between model outcome and observations (van de Wiel et al., 2002; Sandu et al., 2013). But while the energy in submeso-scale motions has been found to generally increase with the complexity of the terrain (Nappo, 1991; Williams et al., 2013) and some basic characteristics of the occurring motions can be related to stability and wind speed (Kang et al., 2015), the aforementioned large heterogeneity between sites is far from being predictable.

Simulations might benefit from locally found similarity expression, Acevedo et al. (2014), however, point out that one would need local expressions for each simulated location and condition, limiting its applicability, and it still might not be accurate due to the highly variable nature of the submeso-scale processes. Therefore, the goal must be a better understanding of the

physical processes and controlling mechanisms of submeso-scale motions, allowing to directly incorporate these into future simulations.

While this asks for further observations, classic measurement techniques are facing a challenge resolving the respective structures. In spite of their large variety, submeso-scale phenomena have in common, that they are significantly non-stationary (Kang et al., 2015; Mahrt, 2007; Mahrt et al., 2009). Neither do they fulfill Taylor’s hypotheses of frozen turbulence (Thomas, 2011; Nakamura and Mahrt, 2005) nor the assumption of isotropy, horizontal homogeneity and ergodicity, which are the foundation of common similarity concepts and theories on turbulence. Hence, point observations in time cannot be expected to provide a representative picture of the motions’ spatial structure and characteristics nor can they be reproduced based on said theories.

A measurement technique with continuous observations both in time and space is needed to resolve the gaps currently left between the point observations of even dense sensor networks. These requirements are met by the distributed temperature sensing (DTS) technique, which is able to record temperatures along a fiber-optic cable by observing the distributed Raman backscatter of a pulsed light amplification by stimulated emission of radiation (LASER) (Selker et al., 2006) with a resolution of decimeters in space and seconds in time (Tyler et al., 2009; Thomas et al., 2012; Pfister et al., 2017; Thomas and Selker, 2021). Due to further development, the technique additionally allows for observation of wind speeds (Sayde et al., 2015; van Ramshorst et al., 2020) and wind directions (Lapo and Freundorfer, 2020; Freundorfer et al., 2021) as well as soil moisture, when buried in the ground (Sayde et al., 2010). Hence, the commonly used term DTS, focused on temperature observation, is recently replaced by the more general term fiber-optic distributed sensing (FODS).

Horizontal as well as vertical FODS deployments have been successfully operated in the BL of the mid-latitudes, providing unique insights into the (nocturnal) BL (e.g. Thomas et al., 2012; Pfister et al., 2017; Lapo et al., 2021; Fritz et al., 2021). In the Arctic, vertical fibers, mounted on a tethered balloon, were used for profile observations of the troposphere on Svalbard with flights of several hours, revealing new insights about stratification and internal boundary layers (Linhardt, 2021). However, no horizontally continuous observations of the Arctic SBL, allowing for investigation of submeso-scale motions, were yet existing. The NY-Ålesund Turbulence Fiber Optic eXperiment (NYTEFOX), being the subject of this thesis, realized such a deployment in early spring 2020 at the Arctic super-site of Ny-Ålesund, Svalbard. The project was a cooperation of the Alfred Wegener Institute for Polar and Marine Research (AWI) and the micrometeorology group of the University of Bayreuth with access to the research facility of the joint French-German collaborative research station of AWI and IPEV (AWIPEV).

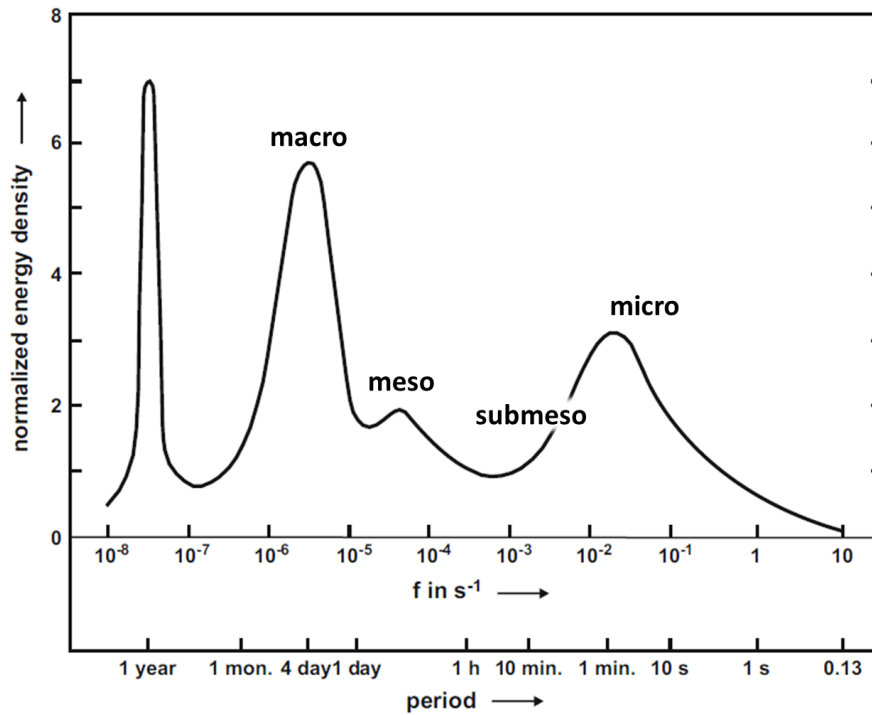


Figure 1.1.: Schematic plot of turbulence spectra, adapted from Foken (2017), originally from Lumley and Panofsky (1964). The range from  $10^{-5}$  to  $10^{-3}$  Hz is usually called meso-turbulence while everything  $>10^{-3}$  Hz is micro-turbulence. Submeso-scale motions take place in the transition, between  $10^{-4}$  and  $10^{-1}$  Hz, which in this depiction is overlapping with both micro- and meso-turbulence.

## 1.2. Objectives

The main three objectives of the NYTEFOX project were:

- to investigate the mechanisms determining spatio-temporal variability in the stable Arctic ABL and identify parameters that allow prediction of the appearance as well as character of mixing motions. The overall goal is to improve our understanding and future parametrization of the relevant exchange processes.
- to explain and close an observational gap that was found between spatially allocated point measurements of operational AWIPEV infrastructure (Schulz, 2017) in order to tie their representativeness to flow regimes that can be derived from atmospheric standard measurements.
- to examine the technical as well as administrative feasibility of a large FODS setup in the harsh conditions of Arctic winter and at a site with restrictions due to research activity and environmental conservation.

The third objective will be briefly covered in the discussion but was mainly subject to the technical evaluation of the data, published in Earth System Science Data (ESSD) (Zeller et al., 2021). Another Master thesis to the project (Zeller, 2020) focused on the second objective. This thesis is focused on the first objective by addressing the following research questions (RQs) and hypotheses (Hs):

RQ 1: Do boundary layer regimes allow predictions about the characteristics of flux and turbulence across the static stability and wind speed ranges?

H 1.1: a) Strong winds will mostly blow along the fjord, channeled by the surrounding mountains.

b) Weak winds are expected to have variable directions due to (sub)meso-scale structures and phenomena, or constant direction because they come down the slopes of the mountains and glaciers as gravity-driven drainage flows.

These hypotheses are motivated by the findings summarized in section 2.1.

H 1.2: Weak winds associated with small cloud cover, allowing for strong radiative cooling, show enhanced horizontal temperature and wind speed variance on time scales of minutes to one hour, indicating motions on the submeso scale.

H 1.3: Abrupt wind-directional changes termed ‘meandering’ mostly occur during weak winds and are generated by competing flows of gravity-driven cold air drainage orthogonal to the fjord axis and weak along-fjord synoptic flows as a result of topographic channeling.

H 1.4: Small-scale topographic features gain importance for the local flow in the weak-wind regime, while in strong winds their effect is negligible due to turbulent convection.

H 1.5: The magnitude of the sensible heat flux  $Q_H$  is primarily forced by wind speed.

RQ 2: Do we observe conditions when the turbulence characteristics are non-locally determined by the properties of the source areas of the advected mean flow, i.e., the turbulence to have a memory of the non-local source area, and thus to disobey local similarity theory?

H 2.1: The impact of non-local influence scales with wind speed and wind direction.

Wind-direction sectors with solely strong winds are expected to show local equilibrium turbulence scaling with local surface characteristics, while turbulence from exclusive weak-wind sectors is subject to non-local forcings of the source area of the time-averaged flow. Sectors with alternating weak- and strong-wind regimes show alternating behavior depending on wind velocity.

H 2.2: For the weak-wind regime, cloud cover is expected to act as an additional forcing on the time-averaged flow, submeso-scale motions, and turbulence: the non-local upwind source area has some impact on turbulence in case of absent to small cloud cover of warm low clouds, while uniform overcast conditions will eliminate the spatial differences between non-local upwind source areas.



## 2. Methods

The observational dataset collected during the campaign was published on Zenodo (Huss et al., 2021), supplemented by a data description paper (Zeller et al., 2021). This paper includes a detailed description of the study site, setup and processing of the raw data. The sections covered by the paper will only be summarized in the following.

### 2.1. Site description

The NY-Ålesund Turbulence Fiber Optic eXperiment (NYTEFOX) was conducted from 26 February to 10 March 2020 in Ny-Ålesund ( $78^{\circ}55'$  N and  $11^{\circ}56'$  E). This small town is the northernmost year-round inhabited settlement in the world, located in the Kongsfjord on the northwestern coast of Svalbard's main island 'Spitsbergen' (see Fig. 2.1). The archipelago, politically belonging to Norway, lies in the Arctic Ocean between Greenland and Siberia.

The village is confined by the fjord in the north-east and by mountains of 500 m to almost

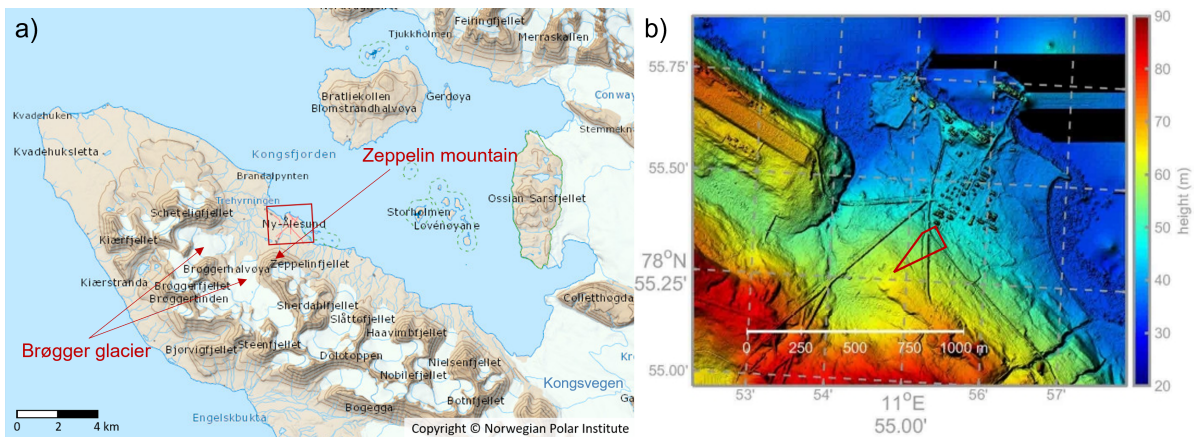


Figure 2.1.: a) shows the location of Ny-Ålesund in the Kongsfjord (Copyright ©Norwegian Polar Institute). The arrows highlight the location of the Zepplin mountain and Brøgger glacier, to which will be referred later on. The red rectangle marks the section displayed in b), which is a hillshade of a digital elevation model (DEM) published by Boike et al. (2018). The hillshade was compiled by Alexander Schulz. The setup is marked as red polygon, the black areas indicate missing data.

800 m above sea level (a.s.l.) to the south and west as well as several glaciers with snouts towards Ny-Ålesund. This orographic setting determines the local wind field with three dominant directions: Winds along the fjord axis from southeast and northwest are observed with the full range of wind speeds, while southwesterly winds, being the third main sector, typically occur with lower velocities (Esau and Repina, 2012; Jocher et al., 2012; Maturilli et al., 2013; Schulz, 2017).

Even though being located at  $79^{\circ}$  N, Ny-Ålesund experiences relatively mild temperatures with monthly averages of  $6^{\circ}\text{C}$  (July) to  $-12^{\circ}\text{C}$  (March) for the 30-year period from 1990 to 2019

(Norwegian Center for Climate Services). Responsible is the West Spitsbergen Current, transporting water of enhanced salinity and temperature from the North Atlantic into the Arctic Ocean, passing Svalbard’s west coast (Aagaard and Greisman, 1975; Haugan, 1999).

Due to the high latitude, conditions during the campaign in early spring were strongly determined by the absence of direct sunlight. Although for flat terrain polar night technically ended on 18 February (Maturilli et al., 2013), the mountain ridge south of Ny-Ålesund still cast a shadow on the study site with only short periods of direct sun during the last days.

### 2.2. Setup

The experiment was set up at the southwestern border of Ny-Ålesund, next to the research facility of the AWIPEV. The core of the setup was a horizontal, trapezoidal array of optical fibers with vertical profiles at three of its corners (Fig. 2.2, letter d, e, and i or OBSE, EDDY and BSRN, respectively). The array’s circumference was about 700 m and allowed for observation of temperature and wind speed along the fibers. Each of the profile towers was equipped with an ultrasonic anemometer (USA) for high-temporal-resolution observation of wind speed, direction and turbulent quantities. A sound detection and ranging (SODAR) was set up at the southernmost point of the setup (letter f in Fig. 2.2), recording vertical wind profiles up to 300 m a.g.l.. The setup was completed by a high-resolution fiber-optic column, measuring the temperature profile from within the snow up to 2.5 m a.g.l. next to the southwestern profile tower.

The FODS technique (Thomas and Selker, 2021), providing high spatiotemporal resolution of temperature, allows to explicitly resolve thermal structures in space and time on scales of short-lived turbulence as well as submeso-scale phenomena (Peltola et al., 2021; Thomas et al., 2012; Pfister et al., 2019; Zeeman et al., 2015). The resolution in this setup was 0.127 m in space and 9 s in time. To take full advantage of the spatially continuous measurements, the horizontal fiber was arranged in a two-dimensional, trapezoidal shape in order to resolve thermal structures irrespective of their horizontal orientation and direction of movement.

The key part of the setup was a pair of metal-encased, loosely buffered single-core fibers of 50  $\mu\text{m}$  diameter (C-Tube, BRUGG, Switzerland) coated with a white, 0.2 mm thick polyethylene (PE) jacket for electric insulation. One of the parallel fibers, which were separated by about 0.1 m, was continuously heated by resistance (red fiber in Fig. 2.2) using a heat pulse unit (HPU) (Silixa, London, UK). The combination of the temperature readings of the unheated and heated fiber-optic cable allowed for computation of wind speed, since the cooling rate of the heated fiber and hence the difference between both fibers is a function of convective cooling (see Sayde et al. (2015); van Ramshorst et al. (2020) and Sec. 2.4.1). The cooling, however, is sensitive to the angle of attack and hence only correctly representing winds orthogonal to the fiber. While this is no constraint for vertically oriented fibers which are always about orthogonal to the main wind, it may render the absolute observed wind speed along horizontal sections incorrect. It, though, still yields valuable high-resolution information on the relative distribution of wind speeds in space.

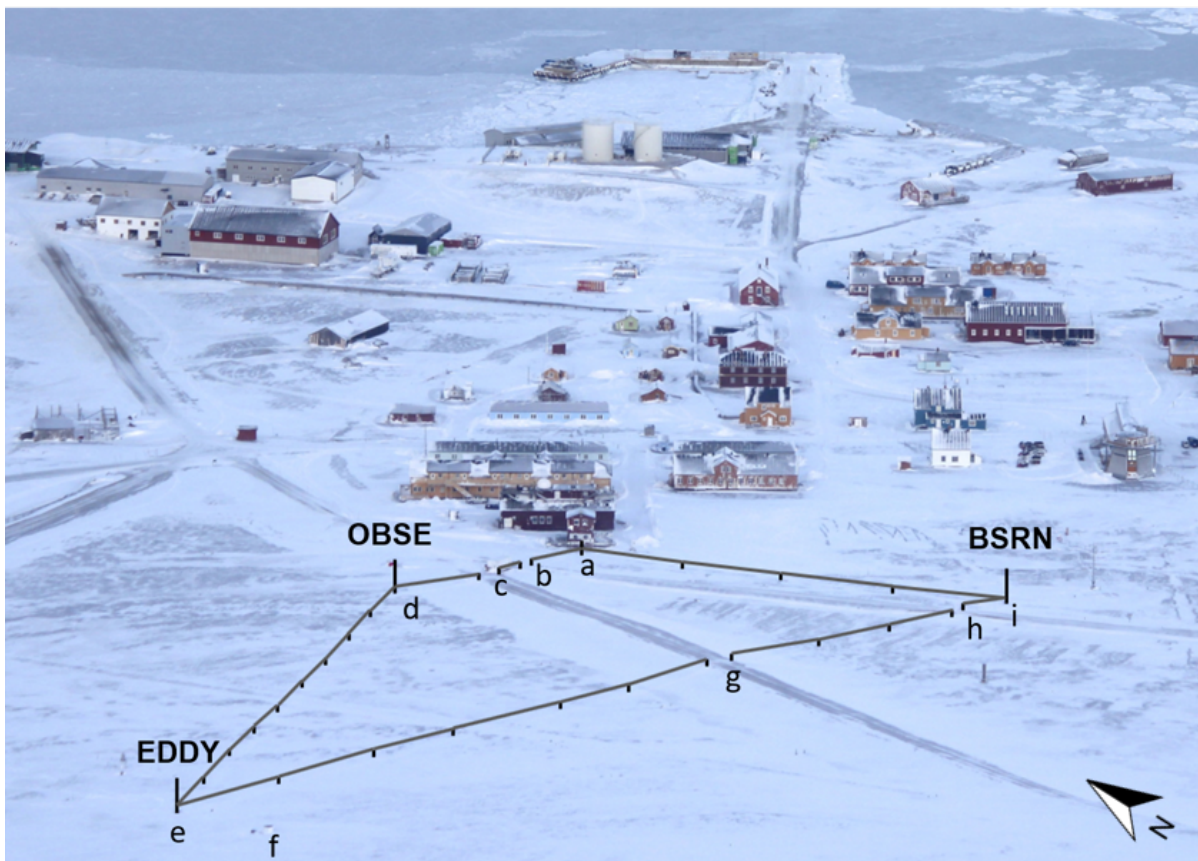
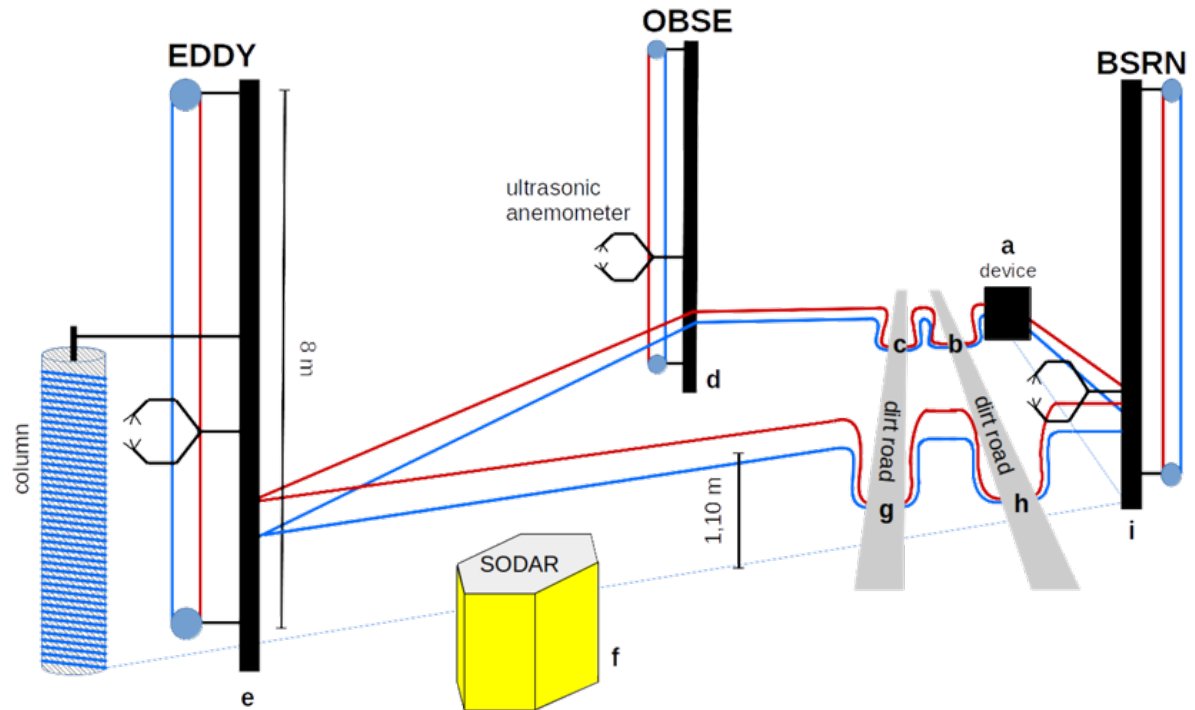


Figure 2.2.: Schematic setup (top panel) and picture of the setup (bottom panel) from the Zeppelin Mountain in the south (photo credit: Harald Sodemann). The fiber-optic array had a length of 700 m. The letters refer to the locations of the fiber-optic distributed sensing (FODS) device (a); the road crossings (b, c, g, h); the 10 m towers (d, e, i), and the minisodar (f). The letters a–i refer to the same elements in both panels.

## 2. Methods

The fibers were mounted at about 1.1 m a.g.l., strung between the telescoping towers featuring three of the corners (letter d, e and i in Fig. 2.2), a metal pole (letter a) and tripods, where the fiber transects crossed roads (letter b, c, g, h). Tension was kept by clamping fixtures used for pasture fences (see Fig. 2.3a). The fibers were supported by tripods about every 30 m (see Fig. 2.3b). Both the unheated and heated fibers were routed vertically along the three 10 m tall towers (see Fig. 2.3c and d), resulting in an ascending and descending branch each, doubling the amount of data points along the profiles.

Both ends of the unheated as well as heated fiber ran into the balloon house (building next to

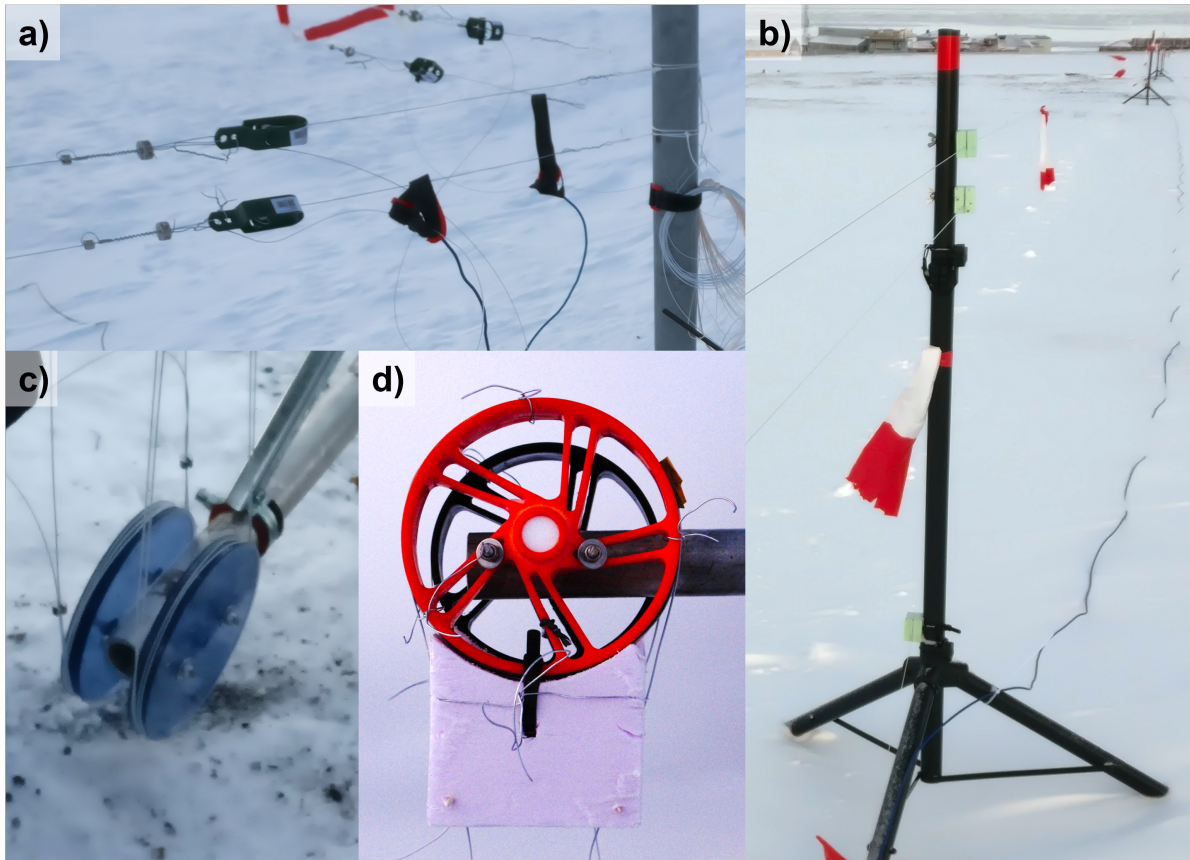


Figure 2.3.: Photographs of the support structures of the metal-encased optical fibers: (a) clamping fixtures at each transect ends to tension the fibers. A metal wire was wrapped around the fiber, additionally secured by clamping screws, acting as an anchor point for tensioners commonly used for pasture fences. (b) tripods along the transects to support the fibers which were clamped in incised blocks of Styrofoam®. (c) bottom and (d) top mounts for fiber profiles on the telescoping towers. Rims of scooter wheels were used at the top to reduce the attack surface for winds while discs of acrylic glass served as mounts at the bottom, where the fibers were kept tight by clamping screws.

Photo credit for (a), (b) and (c): Irene Suomi.

letter a in Fig. 2.2), where each of them was guided through two reference sections of different, controlled and monitored temperature for later calibration. See Zeller et al. (2021), section 3.1.1 for further details on the utilized reference baths. Here, the fibers were fusion-spliced in series, resulting in one continuous optical path. Both its ends were connected to the FODS device (ULTIMA DTS, 5 km variant, Silixa, London, UK) in a double-ended configuration (Hausner et al., 2011).

For more details and descriptions of the remaining compartments of the setup (high-resolution fiber-optic column, USAs and SODAR) as well as their resolutions and accuracies, see Zeller et al. (2021), section 3.1 to 3.3 and table 1.

Additionally, data of the following long-term observation systems operated by the AWIPEV were used in this thesis, which are not described by Zeller et al. (2021): The turbulent latent heat flux was recorded by AWI's eddy covariance (EC) station at 78.921 42° N and 11.914 16° E, about 40 m north of the southwestern profile tower (EDDY). Fluxes were recorded by a USA (CSAT3, Campbell Scientific, Inc., Logan, USA) and a LI-7500RS Open Path Gas Analyzer (LI-COR, Inc., Lincoln, USA) mounted at 2 m a.g.l.. The USA's azimuth was 36°. The system was recording at a frequency of 20 Hz.

The station also featured a ground heat flux plate (HFP01, Hukseflux, Delft, Netherlands) installed at a depth of 0.1 m and recording with a temporal resolution of 2 s.

Data were provided by the Alfred Wegener Institute, Helmholtz Centre for Polar and Marine Research, Potsdam, Germany (PI Alexander Schulz).

Observations of shortwave and longwave radiation were conducted by the baseline surface radiation network (BSRN), located at 78.925° N and 11.930° E, about 90 m northeast of the eastern profile tower (BSRN). The temporal resolution is 1 min. The instrumentation and data set is described in detail by Maturilli et al. (2015).

## 2.3. Feasibility

The successful conductance of the campaign proved the administrative as well as technical feasibility. Svalbard's regulations for conservation of environment and cultural relics still allowed the setup. The undertaken measures to increase visibility and passability of the deployment prevented interference with other research activities and trespassers and while a reindeer once collided with the optical fiber, no harm was done to wildlife and no lasting damage to the setup. However, even better visible markings might completely prevent such incidents.

All materials and operating systems withstood the harsh conditions and provided reasonable results across the whole range of occurring temperatures and wind speeds. An exception might be the high resolution column made of tightly buffered optical fiber, whose readings suggest artifacts due to thermal shrinking of the materials (preliminary results from Prof. Christoph Thomas, not shown).

## 2.4. Data processing

### 2.4.1. Fiber-optic distributed sensing

#### 2.4.1.1. Temperature

The processing and calibration of the FODS observations was done in Python (van Rossum and Drake, 2010) using the open-source library 'pyfocs', developed by the Micrometeorology

Group of the University of Bayreuth (Lapo et al., 2020).

The processing procedure consisted of two main parts: transformation of the raw signal (Raman backscatter intensities, see Selker et al. (2006) for more details) to calibrated temperatures and assignment of geographically referenced, three-dimensional coordinates to the data.

Since the FODS method records only relative measurements, parts of the optical fibers were guided through reference sections of known temperature (see Sect. 2.2). Based on these sections, temperatures were computed for each location along the fiber. The applied calibration method for a double-ended setup, implemented in `pyfocs`, is based on Des Tombe et al. (2020). In order to extract sections with known locations and no artifacts, several steps had to be executed: During the campaign, each point of interest, such as the beginning and end of each transect, was mapped using a global positioning system (GPS) device and measuring the fiber height a.g.l.. Inducing a distinct temperature peak at each respective point along the fiber, visible in the output, then allowed to link the respective length along the fiber (LAF) to the coordinates. `Pyfocs` linearly interpolated the coordinates between the endpoints of each section, assigning an x-, y- and z-coordinate to each bin.

Next, artifacts of the fiber holders were removed in an iterative process by employing diagnostics. Due to their thermal mass and radiative properties, which deviated from those of the fiber, the holders altered the temperature of adjoining fibers and reduced their variability in time. Hence, their influence could be seen both in the average magnitude and standard deviation of the signal, allowing for exclusion of the respective sections by adjusting the margins of the transects.

However, only the artifacts of the metal tensioners (see Fig. 2.3a) and the mounting discs of the vertical profiles (see Fig. 2.3c and d) were subject to this correction. In contrast, the Styrofoam<sup>®</sup> blocks (see Fig. 2.3b) created no visible artifact in the unheated temperature data due to the combination of their low heat capacity and small size. Shielding the fiber from winds, however, they had an effect on the heated temperatures and, hence, the computed wind speeds, similar to the impact of the streamer, attached to increase visibility and avoid accidents. These small artifacts were not excluded in this thesis, though.

The later applied wind speed derivation relies on the data from the unheated and heated fibers being spatially aligned. In the presence of strong temperature gradients, even small mismatches can strongly reduce the quality of the results. Hence, the respective fiber sections were spatially aligned during a period where no heating was applied, by finding the maximum in the spatial cross-correlation. The magnitude of the largest necessary shift was about two bins, corresponding to 0.25 m.

As a last step, the data were temporally resampled to a regular time step of 9 s, eliminating small deviations induced by the internal processing of the FODS device.

### 2.4.1.2. Wind speed

Wind speed computation was based on the wind speed function included in the `pyfocs` package, which was converted from Python to R (R Core Team, 2021). The method after van Ramshorst et al. (2020) was applied, being a revision of Sayde et al. (2015). To account for longwave

radiation towards the fiber ( $I \downarrow + I \uparrow$ ), however, the original expression by Sayde et al. (2015) was used instead of the version simplified by van Ramshorst et al. (2020) for wind tunnel application.

At the core of the computation are the temperatures of the unheated reference fiber  $T_r$  and the heated segment  $T_h$ . Furthermore, the calculation relies on fiber properties such as its radius  $r$ , heat capacity  $c_f$ , density  $\rho$  and surface emissivity  $\epsilon_s$  as well as the thermal conductivity and kinematic viscosity of air  $K_a$  and  $\nu_a$ , respectively, and the Stefan-Boltzmann constant  $\sigma_S$ .  $Pr$  is the Prandtl number and  $C$ ,  $m$  and  $n$  are empirical constants to calculate the Nusselt number, hence related to forced advection of heat by moving air (Cengel and Ghajar, 2014). With  $dt$  being the time between observations and  $P_s$  the applied heating rate to the heated fiber, wind speed  $U$  was calculated according to

$$U = \left( \frac{0.5 P_s \pi^{-1} r^{-1} + 0.5 (I \downarrow + I \uparrow) \epsilon_s - \epsilon_s \sigma_S T_h^4 - 0.5 c_f \rho r \frac{dT_h}{dt}}{C(2r)^{m-1} Pr^n K_a \nu_a^{-m} (T_h - T_r)} \right)^{\frac{1}{m}}. \quad (2.1)$$

The recorded heating rates, however, did not deliver reasonable results with computed wind speeds being almost five times higher than reference wind speeds. Hence, a calibration routine was established, with the wind speeds recorded by the USAs as a reference, to find the heating rate that minimizes the offset in the computed wind speeds from these two techniques. Since this optimal rate varied with wind speed, the campaign period was first divided into temporal blocks of about equal wind speed, according to the following steps:

- The wind speed, recorded by all three USAs with a perturbation time scale of 2 min was spatially averaged.
- A block difference was computed: Two succeeding blocks of 60 min length were shifted along the time series. The wind speeds within the blocks were temporally averaged and the absolute difference between them was computed. This revealed any major changes in the wind-speed regime while the temporal averaging limited the impact of short-lived velocity variations.
- Each period where this difference exceeded  $1.4 \text{ m s}^{-1}$  was then considered a period of major change and its point of maximum  $dU/dt$  was selected as break point.

These break points divided the campaign period into 31 sections of relatively steady wind speed (see App. A.1). Since, due to technical reasons, the 14 days were also treated separately, wind speed calibration was done for 44 individual temporal blocks.

For optimization of the heating rate, the wind speed for the whole array was computed for each temporal block, based on different heating rates with steps of  $0.05 \text{ W m}^{-1}$ . To derive a quality criterion, the computed wind speeds at the vertical sections at the towers, not suffering from angular dependence, were compared to the wind speeds observed by the USAs at the respective towers. To allow for a meaningful comparison, again several steps were executed:

- The FODS wind speeds at the USA height  $\pm 0.5 \text{ m}$  were spatially averaged for both the ascending and descending branches, resulting in a spatial average of 14 bins à  $0.127 \text{ m}$ .
- The resulting wind speeds were temporally averaged to match the time steps of the highest resolution of available USA statistics, which was 30 s.

Now, for each of the three towers a time series of FODS wind speeds based on each of the heating rates was available, matching the location and temporal resolution of the reference wind speed measured by the respective USA.

- For each heating rate and each tower the median deviation between FODS wind speeds and USA reference wind speeds was computed.
- The resulting medians for the three towers were spatially averaged for each heating rate individually. The magnitude of this average median served as a quality criterion for the respective heating rate, indicating the offset of the FODS wind speeds: smaller is better.

Next, a linear interpolation between the heating rates and respective offsets was done between the two heating rates that, according to the outlined criterion, overestimated and underestimated the actual wind speed the least. The heating rate that referred to an offset of zero was then used to recompute the FODS wind speeds for the whole array. This procedure was conducted for each of the 41 temporal blocks individually.

### 2.4.2. External turbulence measurements

The turbulence observations of AWI's EC station were processed by Alexander Schulz, using EddyPro® (LI-COR, Inc., 2021). A double rotation was applied, rotating the coordinate system such that the average vertical wind equaled zero. Furthermore, frequency corrections for the low frequency (Moncrieff et al., 2004) and high frequency range (Moncrieff et al., 1997) were applied as well as a density correction after Webb et al. (1980).

A perturbation time scale of 10 min was used. Due to a storing failure of the logger, the last 20 min of each hour were not recorded, resulting in two succeeding, empty 10 min intervals per hour. However, the analyses based on these data were conducted on a temporal resolution of 1 h. The malfunction, hence, reduced the amount of data contained in each temporal average and hence its statistical validity while gaps in the final analyses could be avoided.

For the processing steps of the high resolution FODS column, the NYTEFOX USAs and the SODAR, see Zeller et al. (2021), section 4.1.3 to 4.3.

### 2.4.3. Data correction

Due to technical difficulties, one of the two FODS calibration baths had an instationary temperature, occasionally causing the temperatures of the two units to converge and even cross each other. These events resulted in implausible observations for the whole FODS setup. Hence, a quality criterion was developed with the temperature observations of the USAs at the profile towers as reference. This resulted in rejection of a total of 20 h 50 min of data which were discarded. For further information on the selection criterion, see Zeller et al. (2021), section 4.1.2.

## 2.5. Analysis

All data analysis was done using R (R Core Team, 2021), version 3.6.0., 4.0.3 and 4.1.0.

### 2.5.1. Radiation and energy balance

All fluxes of energy and matter are specified according to the micrometeorological sign convention where fluxes directed away from the surface have a positive sign while negative values indicate flux towards the surface.

A radiation balance was devised according to equation 1.1 based on the observations of short-wave global radiation and reflected radiation ( $K \downarrow$ ,  $K \uparrow$ ) as well as incoming and outgoing longwave radiation ( $I \downarrow$ ,  $I \uparrow$ ) from AWI's BSRN station.

The resulting net radiation  $Q_S^*$  in addition with the ground heat flux  $Q_G$  forms the available energy at the surface, balanced by the turbulent energy transfer between surface and atmosphere (sensible and latent heat flux  $Q_H$  and  $Q_E$ ). Hence, a surface energy balance can be formed as

$$-Q_S^* = Q_H + Q_E + Q_G + \epsilon. \quad (2.2)$$

where the imbalance term  $\epsilon$  accounts for a horizontally non-uniform surface, containing all components preventing a closed energy balance (Mauder et al., 2020). Under the site conditions with a snow-covered surface, this mainly includes advection, heat storage, vertical divergence of radiation and turbulent flux and uncertainties of the measurements.

The influence of measurement uncertainty cannot be assessed with the setup but is not expected to be systematic on the device level. However, one has to keep in mind that the radiation measurements were separated from the flux station by about 300 m and hence did not share the same footprint. The change of heat storage in the soil above the depth where  $Q_G$  is measured is usually considered a significant quantity (Heusinkveld et al., 2004; Meyers and Hollinger, 2004). However, due to the insulating snow cover and the absence of a distinct diurnal cycle with direct solar radiation, temperature fluctuations in the upper soil layer and hence the change in its storage are expected to be small compared to the other terms of the energy balance. This also applies to the change in heat storage of the air below the height of the flux station, whose heat capacity is especially small due to the low moisture in cold conditions.

The most significant contribution to  $\epsilon$  is expected from horizontal advection of sensible heat  $Q_A$ , being an interplay between secondary circulations on a submeso scale (Kanda et al., 2004; Mauder et al., 2020) and the influences of very different surfaces in close proximity. These different surfaces include e.g. the fjord, glaciers, plane snow surfaces and steep mountains slopes. The large two-dimensional setup of optical fibers allows for directly estimating  $Q_A$  from the horizontal temperature field and the wind direction and speed recorded by the USAs.

The estimation of this term in the heat budget was done for a volume with a square footprint of  $L_e = 45$  m edge length. It was located inside the FODS array such that all associated measuring points were inside the array and did not intersect with the roads (see Fig. 2.4).  $Q_A$  was then defined as the sum of net heat transport in x and y direction through the vertical walls

of the volume:

$$Q_A = H_{A,x2} - H_{A,x1} + H_{A,y2} - H_{A,y1} \quad (2.3)$$

With  $H_A$  being the advective transport of sensible heat through the respective wall of the volume ( $x1$  and  $x2$  are the walls in  $x$ ,  $y1$  and  $y2$  those in  $y$  direction). Therefore, nine 16 m long transects were defined across each side of the volumes' footprint as shown in figure 2.4. Temperatures were interpolated for locations spaced every 2 m equidistantly across the transects based on all horizontal temperature readings of the fiber. Interpolation was done by inverse distance weighting after Shepard (1968) with a power of  $p = 2$ , using the R-package 'phylin' (Tarroso et al., 2019). A linear model was fitted through all points of each respective transect, using the R function 'lm', based on Wilkinson and Rogers (1973). The slope of the returned linear equation served as the temperature gradient  $\Gamma$  for the point, where the transect crossed the wall of the volume. The corresponding wind component orthogonal to the respective wall ( $u$  as wind from west and  $v$  as wind from south) was interpolated similar to the temperatures, based on the three USAs.

The temperature gradient was defined relative to the wind direction, such that a temperature increase in the direction of the respective wind component always returned a positive gradient and vice versa. The differences of the product of wind and gradient between the opposing sides were then integrated in  $x$ - and  $y$ -direction respectively, summed and converted into energetic units as follows:

$$Q_A = \frac{1}{L_e} \left( \int_{i=0}^{i=L_e} (\Gamma_{x2,i} \cdot u_{x2,i} - \Gamma_{x1,i} \cdot u_{x1,i}) dx + \int_{i=0}^{i=L_e} (\Gamma_{y2,i} \cdot v_{y2,i} - \Gamma_{y1,i} \cdot v_{y1,i}) dy \right) \rho c_p \quad (2.4)$$

With  $Q_A$  resolved, it can now be excluded from the residual term  $\epsilon$ , modifying the energy balance (Eq. 2.2) to

$$-Q_S^* = Q_H + Q_E + Q_G + Q_A + \epsilon_m \quad \text{and} \quad (2.5)$$

$$\epsilon_m = -Q_S^* - Q_H - Q_E - Q_G - Q_A \quad \text{respectively} \quad (2.6)$$

with  $\epsilon_m$  being the modified residual without  $Q_A$ .

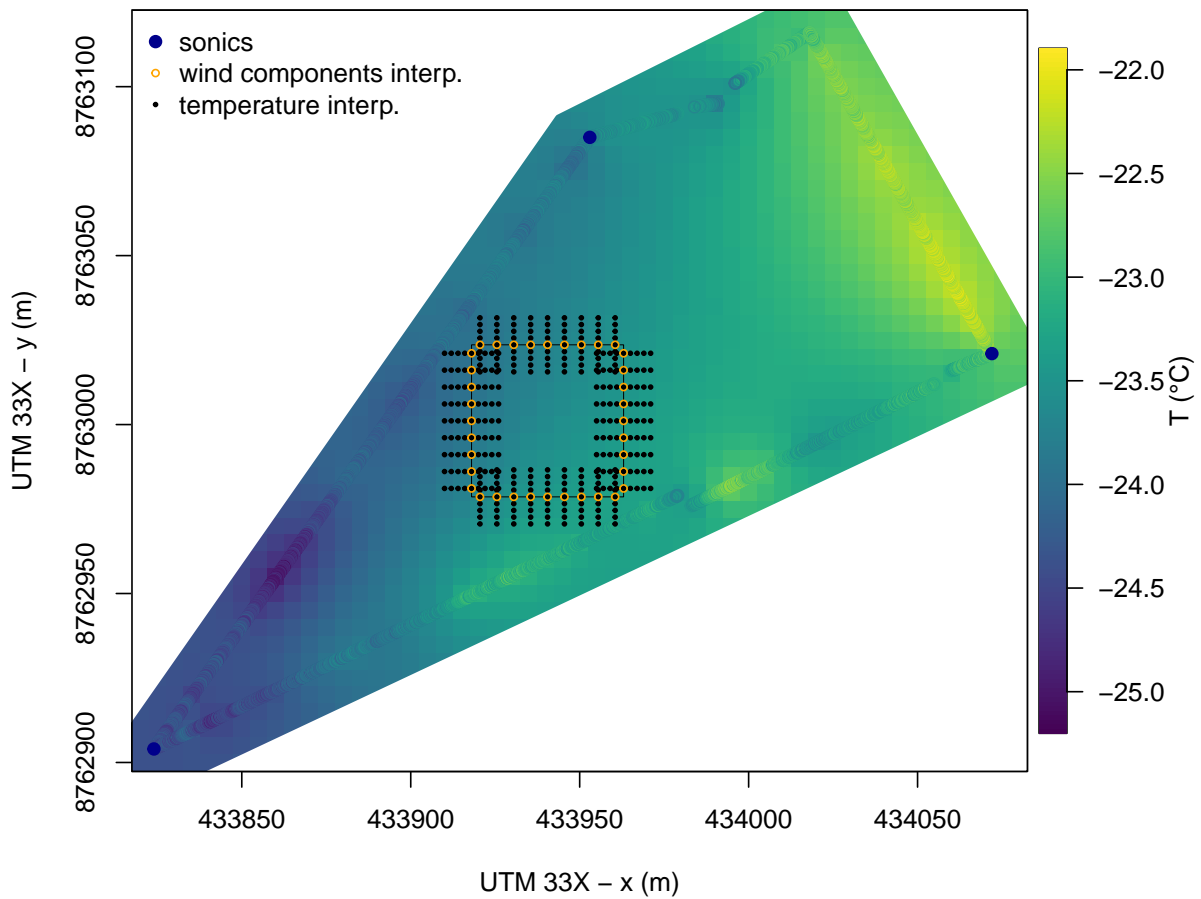


Figure 2.4.: Map of interpolated temperatures based on all horizontal temperature readings by the optical fiber for 2 min on 26.02.2020. The spatial resolution is  $5 \times 5$  m. The colored points are the original readings, dark blue points mark the locations of the ultrasonic anemometers (USAs). The black square shows the footprint of the reference plane for estimating  $Q_A$ . Temperatures are interpolated for all black points to calculate gradients while wind components are interpolated for the location of the orange rings.

### 2.5.2. Flux-gradient-similarity

A local first order closure was applied to calculate the sensible heat flux based on local flux-gradient similarity theory after Monin and Obukhov (1954):

$$\overline{w'T'} = -\frac{\kappa \alpha_0 u_* \delta T}{\varphi_H(\zeta) \delta \ln(z)} \quad (2.7)$$

$\kappa$  is the dimensionless von Kármán constant of 0.4 while  $\alpha_0$  usually refers to the inverse Prandtl number  $Pr = 0.85$ . The employed universal functions (see below), however, require  $\alpha_0$  to equal 1 (Högström, 1988, p. 76).  $u_*$  is the friction velocity, here retrieved from the USA at the BSRN tower. The logarithmic temperature profile  $\delta T/\delta \ln(z)$  is obtained from the FODS profile at the BSRN tower, applying a linear model to  $dT/d \ln(z)$ . The universal functions  $\varphi_H(\zeta)$  from Businger et al. (1971) were used, normalized according to Högström (1988, p. 76):

$$\varphi_H = 0.95 (1 - 11.6\zeta)^{-1/2} \quad \text{for } \zeta < 0 \quad (2.8)$$

$$\varphi_H = 0.95 + 7.8\zeta \quad \text{for } \zeta > 0 \quad (2.9)$$

$\zeta$  is a dynamic-stability parameter with positive values indicating stable and negative values unstable conditions. It is defined as the ratio  $z/L$  with  $z$  being the height of observation (here the USA at the BSRN tower at 1.5 m a.g.l.).  $L$  refers to the Obukhov length, described as “[...] the height of the sub-layer of dynamic turbulence” (Monin and Obukhov, 1954). It is calculated as follows:

$$L = -\frac{u_*^3}{\kappa \frac{g}{T} \frac{Q_H}{\rho c_p}} \quad (2.10)$$

with  $g$  being the gravitational acceleration of  $9.83 \text{ m}^2 \text{ s}^{-2}$  (Breili et al., 2017) and  $T$  the dry bulb temperature. However, the sonic temperature measured by the USA was used since the difference between sonic and dry bulb temperature is assumed negligible in the cold and dry atmospheric environment. The buoyancy flux  $Q_H$  was recorded by the USA at the BSRN tower.  $c_p$  and  $\rho$  are defined as outlined above.

Applying these equations to solve equation 2.7,  $\overline{w'T'}$  was retrieved and then converted to  $Q_H$  (from kinematic to energetic units of  $\text{W m}^{-2}$ ) by multiplying it with  $\rho$  and  $c_p$ .

The result is sensitive to the estimate of  $Q_H$  in eq. 2.10 (retrieved from the USA). Hence, the computation was iterated using the calculated  $Q_H$  as new input until the maximum difference between the time series of consecutive iterations fell below  $|0.1| \text{ W m}^{-2}$ , resulting in 98 iterations.

### 2.5.3. Defining boundary layer regimes

To allow for meaningful bulk statistics, the main campaign period (26.02. to 10.03.2020) was classified using BL regimes based on different meteorological parameters. The classification was applied to windows of about 77 min length, matching the time windows on which the

multi-resolution decomposition (MRD) (see Sect. 2.5.5) was later applied, allowing to sample the MRD conditionally by said regimes. The classification was based on wind speed  $U$ , wind direction  $\varphi$ , longwave incoming radiation  $I \downarrow$ , static stability and meandering intensity with their categories listed in table 2.1.

Table 2.1.: The regime parameters wind speed ( $U$ ), wind direction( $\varphi$ ), longwave incoming radiation ( $I \downarrow$ ), static stability and meandering and their categories applied to form boundary layer (BL) regimes.

category	cat. 1	cat. 2	cat. 3	cat. 4
$U$ ( $\text{m s}^{-1}$ )	$\leq 2.5$	$> 2.5$		
$\varphi$ (-)	NE ( $320^\circ$ to $80^\circ$ )	SE ( $80^\circ$ to $170^\circ$ )	SW ( $170^\circ$ to $275^\circ$ )	NW ( $275^\circ$ to $320^\circ$ )
$I \downarrow$ ( $\text{W m}^{-2}$ )	$\geq -175$	$-175$ to $-245$	$< -245$	
static stab. ( $\text{K}/\ln \text{m}$ )	$< -0.06$	$-0.06$ to $0.06$	$> 0.06$	
meandering ( $^\circ$ )	$\leq 15$	$15$ to $30$	$30$ to $56$	$> 56$

A site-specific threshold value for wind-speed categorization was derived after Sun et al. (2012) by relating the wind speed and turbulence intensity. In deviation from Sun et al. (2012), the friction velocity  $u_*$ , computed from the total shear, was used as a metric for turbulence intensity instead of the turbulent kinetic energy  $TKE$ . Weak wind was defined as the wind-speed range where turbulence is mainly generated by local shear instability and, as a result,  $u_*$  does not scale with  $U$ . Strong wind, in contrast, is the velocity range where turbulence is mainly generated by the bulk shear which is closely tied to wind speed. The velocity where  $u_*$  starts to increase about linearly with  $U$  therefore served as the threshold between weak and strong wind.

This threshold was found to be  $2.5 \text{ m s}^{-1}$ , being consistent for the observations of the USAs at all three towers (see Fig. 2.5) and is used as threshold from here on.

Sun et al. (2012) found the threshold to increase about logarithmically with the height of observation. They obtained thresholds of  $1$ ,  $1.6$  and  $3 \text{ m s}^{-1}$  for heights of  $0.5$ ,  $1.5$  and  $5 \text{ m}$  a.g.l. respectively over flat grass land in the Cooperative Atmospheric Surface Exchange Study 1999 (CASES-99). Pfister et al. (2019) applied the same method and observed a threshold value of  $1.2 \text{ m s}^{-1}$  at  $1 \text{ m}$  a.g.l. for the Shallow Cold Pool Experiment (SCP), which corresponds well to this height-velocity relationship observed for CASES-99. The threshold for the NYTEFOX site, however, deviates from that pattern: While we observed a threshold of  $2.5 \text{ m s}^{-1}$  at  $1.4 \text{ m}$  a.g.l., Sun et al. (2012) obtained a threshold of only  $1.6 \text{ m s}^{-1}$  at almost the same height. Conversely, the NYTEFOX threshold, obtained at  $1.4 \text{ m}$  a.g.l., corresponds to a height of about  $3.5 \text{ m}$  a.g.l. for CASES-99. This might be due to the lower surface roughness of the snow-covered soil in comparison to the grass land in both CASES-99 and SCP. Hence, the roughness of the snow-covered surface of Ny-Ålesund seems to impact momentum transport during winds of  $2.5 \text{ m s}^{-1}$  as much as the roughness of grass land for a wind speed of  $1.6 \text{ m s}^{-1}$ . In other words: over snow, a higher time averaged wind speed is needed to couple the momentum flux to the surface.

This promotes typical weak-wind phenomena such as submeso-scale motions and the tendency to strong stratification during a wider range of synoptic conditions compared to vegetated areas.

Wind direction was categorized based on the distribution of directions at the EDDY tower. This tower was chosen since it was the one farthest away from and, hence, least impacted by buildings. The sectors were defined such that the density peaks at both directions along the fjord (SE and NW) and the direction down the Zeppelin Mountain and Brøgger glacier (SW, see Fig. 2.1) were in different sectors (see Fig. 2.6). The NE-sector is the remainder that almost never occurred.

$I \downarrow$  categorization is based on observations of AWIs BSRN. Thresholds were set such that they separate the three main density peaks in the distribution of  $I \downarrow$  (see App. A.2).

Static stability was calculated based on fiber optic temperature profile observations at all three towers of the FODS array. First, the profiles were transformed to potential temperature relative to the lowest observation of each profile, assuming a dry-adiabatic lapse rate of  $9.8 \text{ K km}^{-1}$ . A linear model was then applied to the logarithmic altitude over temperature. The resulting slopes of all towers were averaged, yielding a gradient with the temporal resolution of the FODS observations (9 s). All gradients  $< -0.06 \text{ K ln m}^{-1}$  were considered statically unstable while gradients  $> 0.06 \text{ K ln m}^{-1}$  are referred to as statically stable. The range from  $-0.06$  to  $0.06 \text{ K ln m}^{-1}$  was, hence, defined as neutral. The threshold values were retrieved from observations during the Large-eddy Observatory Voitsumra Experiment 2019 (LOVE19) (Lapo et al., 2021), in personal communication (Thomas, 2020).

For all these four parameters a regime window was assigned a category if at least 90 % of its data were within the respective category. If that did occur for no category, it was assigned category 0 for the respective parameter. This does not apply for meandering since it was directly computed based on each window.

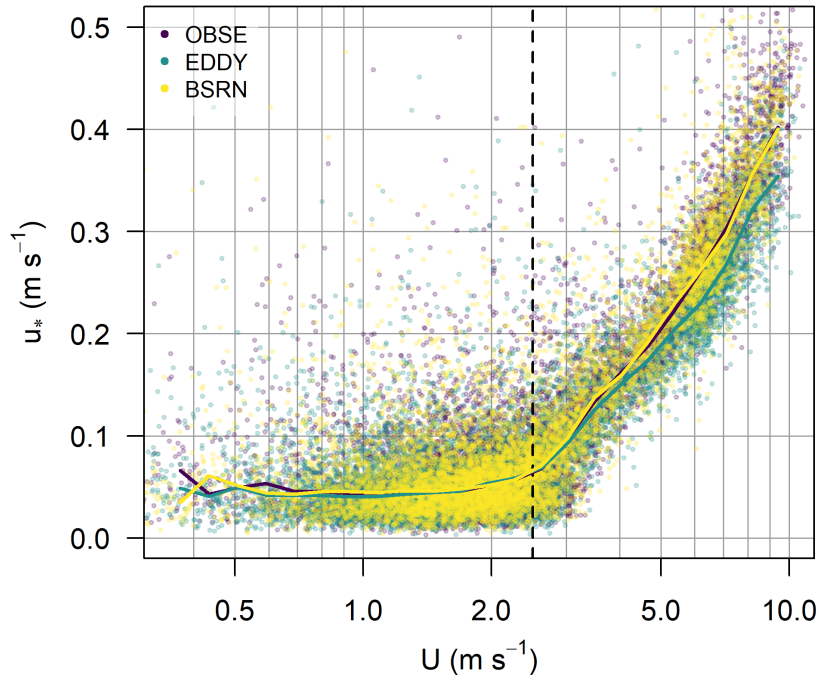


Figure 2.5.: Friction velocity  $u_*$  over wind speed on log axis recorded by the ultrasonic anemometers (USAs) at all towers, covering the whole measuring period (26.02. – 10.03.2020). Colored lines are bin averages (method: median) for the respective tower of equal width in log space. The dashed line visualizes the wind speed threshold of  $2.5 \text{ m s}^{-1}$ .

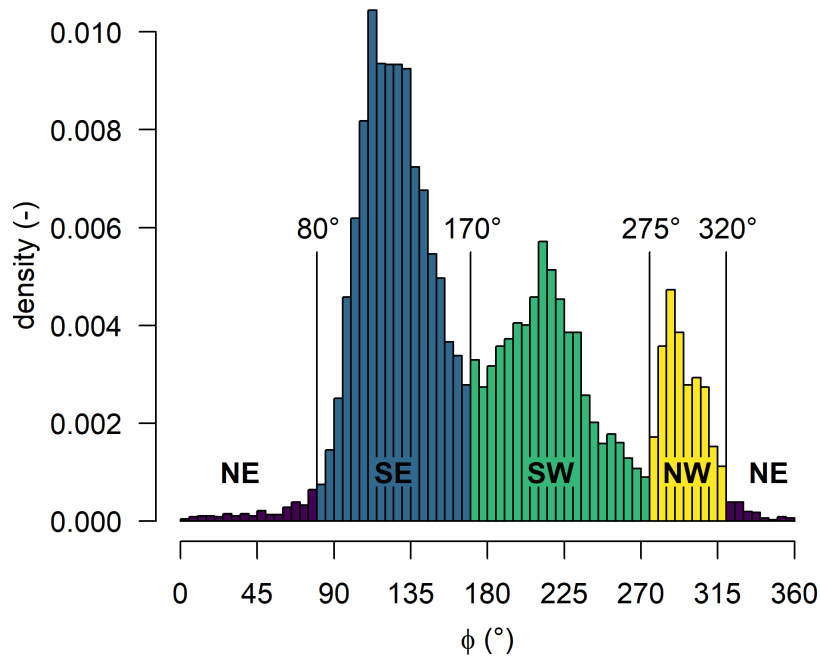


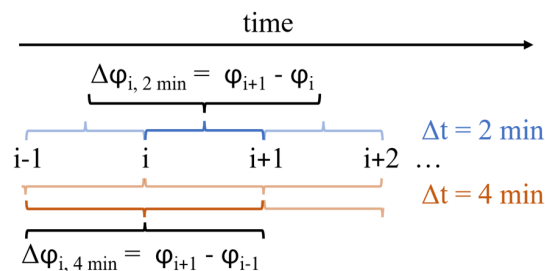
Figure 2.6.: Density distribution of wind direction  $\varphi$  recorded by the ultrasonic anemometer (USA) at the EDDY tower (latter ‘e’ in Fig. 2.2) with a perturbation time scale of 2 min. The plot covers the whole measuring period from 26.02. – 10.03.2020. The direction sectors for regime categorization (see Sect. 2.5.3) are expressed by colors and sector names (*NE*, *SE*, *SW* and *NW*) according to the sectors main direction. The labeled vertical lines depict the sector boundaries.

### 2.5.4. Detecting meandering

For detection of meandering, the constancy-method after Freundorfer (2017) was tested, which relates the vector-averaged and scalar-averaged wind speed for a defined time window. However, this method was not able to detect the specific kind of meandering occurring at the site, where directional changes were relatively small, ranging from only about  $60^\circ$  to  $100^\circ$ . Therefore, a new routine for detection and classification of meandering was developed with adjustable thresholds, allowing for various conditions.

The method relies on the distribution of directional changes  $d\varphi/dt$  during a given time window and the principle can be summarized as follows: A time window is considered a meandering interval if a defined minimum fraction of its time steps features directional changes  $|\Delta\varphi|$  exceeding a minimum threshold.

For compatibility with the BL regimes, the categorization was based on the same windows of 77 min length. 2 min wind direction data of the USA at the EDDY tower were used to determine  $d\varphi/dt$ . Since the method should also account for directional changes on time scales larger than 2 min, the  $\Delta\varphi$  for each instant  $i$  along the time series was calculated for a  $\Delta t$  of 2 min as well as 4 min according to the following schematic:



The largest of the two  $\Delta\varphi$ , being  $\Delta\varphi_i = \max(\Delta\varphi_{i, 2 \text{ min}}, \Delta\varphi_{i, 4 \text{ min}})$ , was then passed on to the next step.

Even higher values for  $\Delta t$  would further improve detection of directional changes on long time scales. With increasing  $\Delta t$ , however, a single, strong  $\Delta\varphi$  influences an increasing number of time steps, distorting the distribution. Hence, a maximum  $\Delta t$  of 4 min was selected since it yielded the largest gain in terms of largest detected  $\Delta\varphi$  per 2 min-increase of maximum  $\Delta t$  (see App. A.3).

The increase of  $\Delta t$  above the temporal recording resolution allowed for  $|\Delta\varphi|$  being larger than  $180^\circ$ : If e.g. the wind direction over a  $\Delta t$  of 4 min turned from north to south-east, the 2 min data might show that the wind turned over west ( $|\Delta\varphi| = 225^\circ$ ) instead of east ( $|\Delta\varphi| = 135^\circ$ ). The applied steps yielded 37  $\Delta\varphi$  values per 77 min window to evaluate the distribution of directional shifts. The small sample size of the distribution prevented a precise determination its percentiles which could serve as a meandering criterion. Hence, for each window a student's t-distribution was fitted to the distribution of  $\Delta\varphi$  values of which the  $5^{\text{th}}$  and  $95^{\text{th}}$  percentile was computed. The distribution and model fit for one example window are shown in appendix A.4. Assuming a symmetric distribution, the absolute percentiles were then averaged, yielding the

mean magnitude of this interpercentile range. For simplicity, this is referred to as IPR from here on, even though it describes a magnitude instead of a range.

Now, every window was represented by one IPR value. To derive meaningful thresholds to determine the meandering intensity of each window based on its IPR, the IPR was also calculated for the bulk of all strong wind conditions, where no meandering was assumed and all weak-wind conditions, where meandering was expected to be possible (Fig. 2.7).

The reference IPR was about  $56^\circ$  for weak and  $15^\circ$  for strong winds, yielding two thresholds for

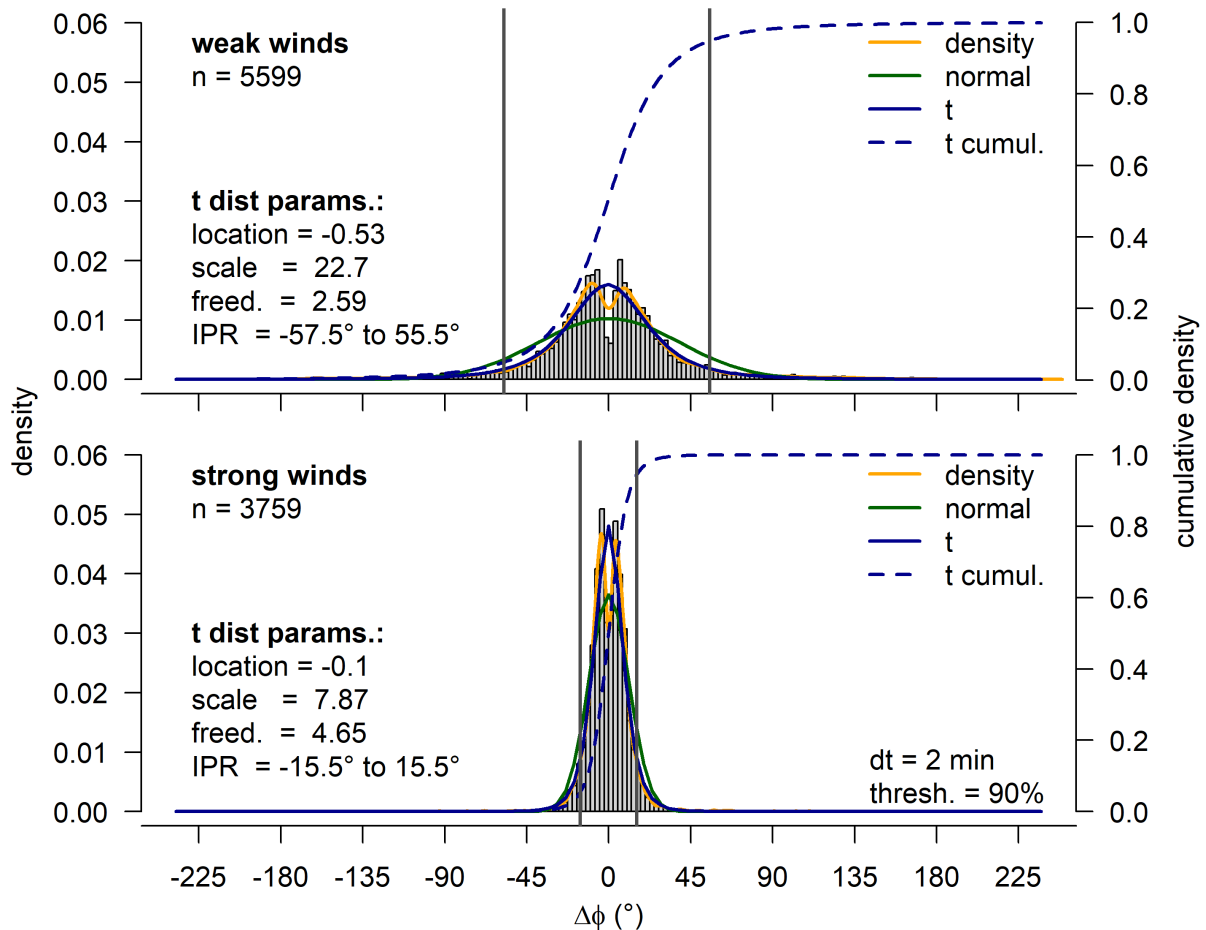


Figure 2.7.: Distribution of  $\Delta\varphi$  calculated with a maximum  $\Delta t$  of 4 min (see Sect. 2.5.4). The top panel shows only weak-wind data with  $U \leq 2.5 \text{ m s}^{-1}$  while the bottom panel shows all data with higher wind speeds. The orange lines are the density functions and the green lines the normal distribution. The blue solid lines show a student's t-distribution fitted to the respective data while the dashed lines are the related cumulative density. The respective fit parameters are listed under 't dist. params.'. The grey vertical lines mark the 5<sup>th</sup> and 95<sup>th</sup> percentile with the respective  $\Delta\varphi$  values listed as interpercentile range (IPR).

the categorization. Accordingly, windows with an  $\text{IPR} \leq 15^\circ$  were considered non-meandering windows while those with  $\text{IPR} > 56^\circ$  were expected to show strong meandering. However, the windows with  $15^\circ < \text{IPR} \leq 56^\circ$  still comprised very different meandering characteristics. Hence, a third threshold was visually derived and introduced at  $\text{IPR} = 30^\circ$ , resulting in four meandering categories:

Table 2.2.: Explanation of the meandering categorization applied on windows of 77 min length according to section 2.5.4.

IPR	category	meaning
$\leq 15^\circ$	1	no meandering
$15^\circ$ to $30^\circ$	2	weak meandering
$30^\circ$ to $56^\circ$	3	medium meandering
$> 56^\circ$	4	strong meandering

### 2.5.5. Multi-resolution decomposition

To investigate the temporal scales of the dynamics of spatial temperature and wind-speed distributions, an multi-resolution decomposition (MRD) was performed on the horizontal FODS observations. The MRD in time decomposes a time series orthogonally into subrecords of dyadic length  $n = 2^m$  and averages them unweighted.  $m = 0, 1, \dots, M$  refers to the respective decomposition mode with  $M + 1$  being their total number. Hence,  $2^M$  is the length of the longest mode as well as the length of an individual MRD window which contained  $2^9 = 512$  data points in this thesis. This corresponds to 46:48 min based on a temporal resolution of 9s. The length of each analyzed data set, therefore, had to equal this length or be a multiple.

For each mode the unweighted mean of the respective subrecords is computed and subtracted from the time series before the next, higher-frequent mode is applied. Hence, the perturbations displayed by each mode only contain the variability not covered by the lower-frequent modes, satisfying Reynolds averaging. In contrast to transform methods relying on the periodicity of a signal, the MRD also captures solitary or aperiodic events making it an ideal tool to study the often erratic SBL processes.

The results of the MRD can be used to calculate scale-dependent two-point correlation coefficients  $R_X$  between the points  $i$  and  $j$  for all points along a fiber transect with

$$R_{X,ij} = \frac{\overline{X'_i X'_j}}{\sigma_{X_i} \sigma_{X_j}}. \quad (2.11)$$

$X$  is a placeholder for either temperature  $T$  or wind speed  $U$ ,  $\sigma$  is the standard deviation. The mean spectrum density  $D_X$  was calculated for each point along the fibers according to

$$D_{X_m} = \frac{1}{2^{M-m}} \sum_1^{2^{M-m}} X_m^2 \quad (2.12)$$

to get variance spectra of  $X = T$  and  $U$ . The applied software function was written in R by Linhardt (2021) based on the code by Thomas (2011), written in Matlab.

## 3. Results and discussion

This chapter starts with an overview over the general atmospheric conditions during the measurement campaign. All following content is arranged according to the research questions and hypotheses introduced in section 1.2.

### 3.1. General characteristics

#### 3.1.1. Air temperature and wind speed

The measuring period stands out with exceptionally cold air temperatures down to  $-29^{\circ}\text{C}$  measured at 2 m a.g.l. (Fig. 3.1a). The average temperature of  $-17^{\circ}\text{C}$  was also well below the inter-annual mean of  $-12^{\circ}\text{C}$  for February and March from 1993 until 2011 (Maturilli et al., 2013) and the even warmer years of 2012 to 2019 with monthly averages of  $-8^{\circ}\text{C}$  and  $-10^{\circ}\text{C}$  for February and March (Norwegian Center for Climate Services).

Wind velocities at 2.5 m a.g.l. ranged up to about  $10\text{ m s}^{-1}$  (Fig. 3.1b) but stayed below  $3\text{ m s}^{-1}$

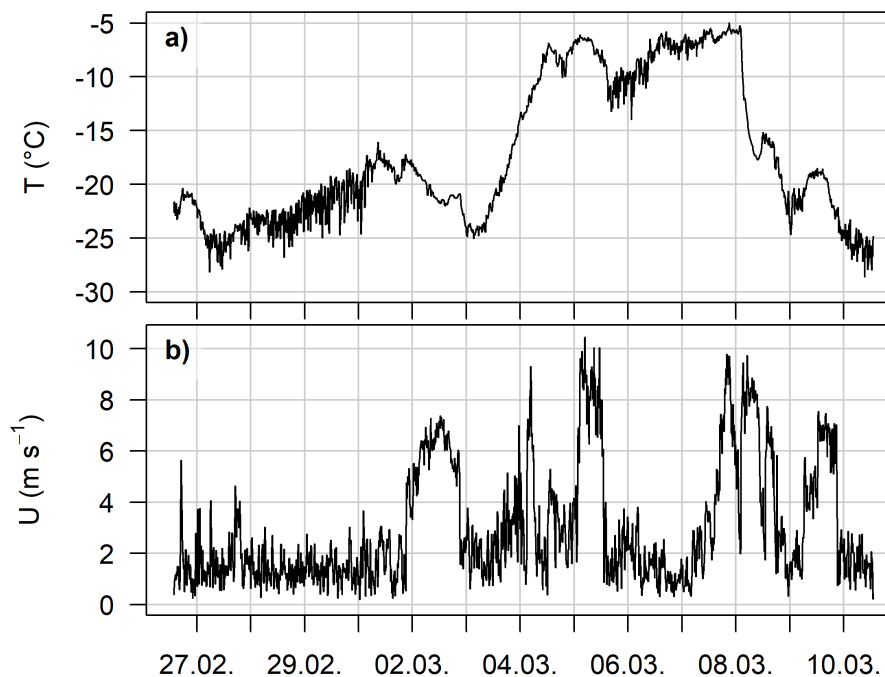


Figure 3.1.: a) temperature at 2.1 m a.g.l. and b) wind speed at 2.5 m a.g.l. recorded by slow response sensors at AWT's EC-station for the whole measuring period (26.02. - 10.03.2020). Data were collected at 0.5 Hz, aggregated to 10 min.

for a long periods of times, indicating extensive periods of weak synoptic forcing. During these intervals, the temporal temperature fluctuations increased strongly.

Further review of wind velocities was given in section 2.5.3 while wind directions close to the

ground are analyzed in section 3.2.1.

During most of the calm periods wind speeds remained low also in greater height (see Fig. 3.2a). A low-level jet could, hence, not be observed up to the maximum resolved height of almost 300 m a.g.l..

However, an increase of wind speed with height occurred during periods of strong synoptic

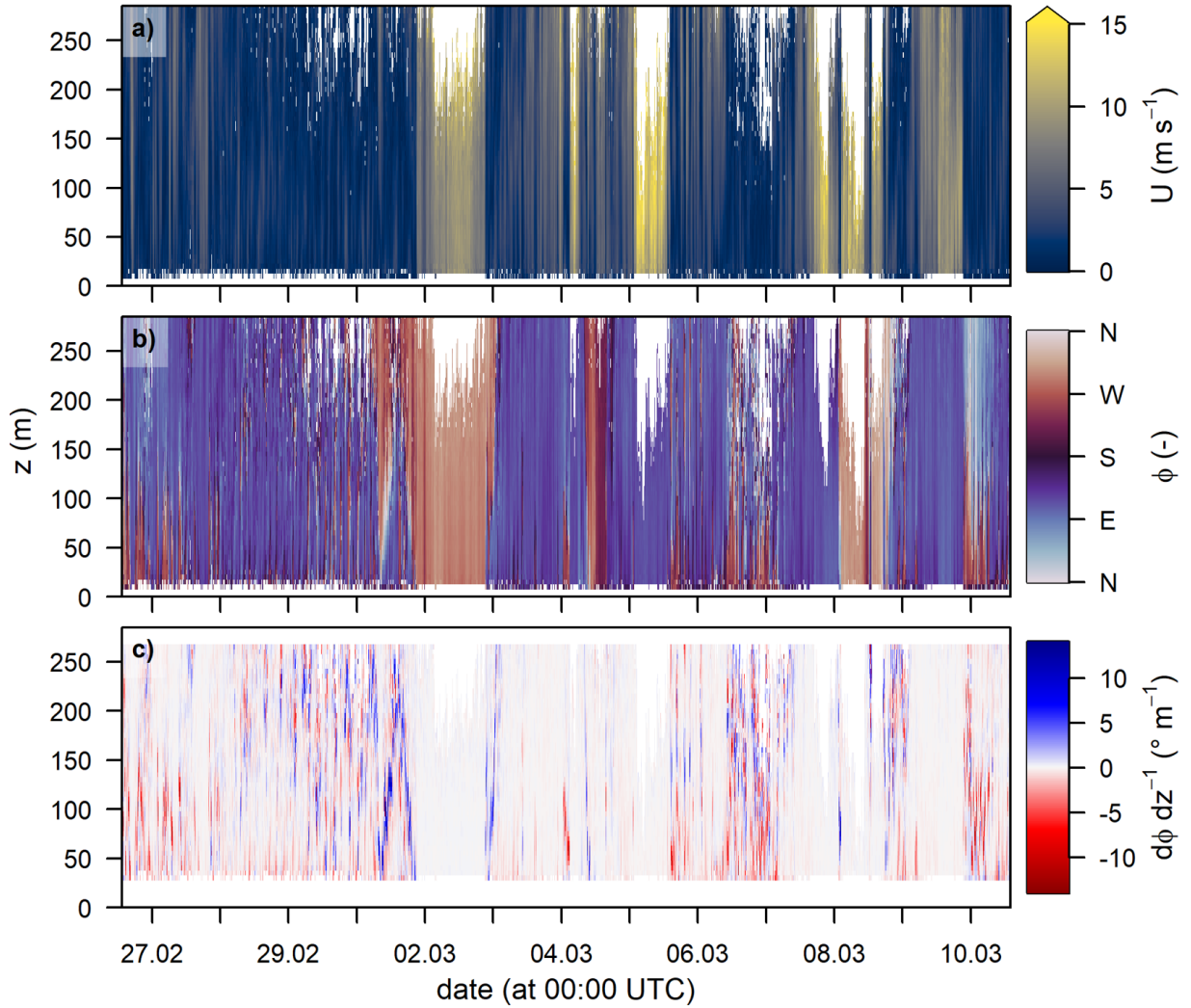


Figure 3.2.: Wind speed  $U$  (a), wind direction  $\phi$  (b) and vertical wind direction change (c) across height  $z$  for the whole measuring period (26.02. - 10.03.2020). Data are measured by the sound detection and ranging (SODAR) (latter ‘f’ in Fig. 2.2), vertically aggregated to a resolution of 5 m and temporally averaged to 10 min. White areas indicate missing data due to an insufficient signal. While wind speeds ranged up to almost  $23 \text{ m s}^{-1}$  the range displayed in (a) is limited to  $15 \text{ m s}^{-1}$  for better distinguishability of lower velocities. The vertical wind direction change in (c) is computed as difference between running block differences of 20 m height. Blue colors indicate a clockwise directional change with increasing height while red represents counter-clockwise turns.

forcing with velocities up to almost  $23 \text{ m s}^{-1}$  (see Fig. 3.2b and explanation in the caption). This is due to the decreasing impact of surface stress with height.

Wind directions were spatially steady with height during strong winds while substantial turns

appeared during calm periods, often reversing flow directions at the ground (see Fig. 3.2c). The height at which these changes took place varied across the whole observed range. However, conditions where weak winds close to the ground came from SW down the slopes of the adjoining mountains often showed a turn towards easterly winds at around 50 to 150 m. These presumably density-driven flows, hence, appeared to be local deviations from the regional flow field.

Since the surrounding mountains surmounted the maximum measurement height by 200 to 500 m it is conceivable that a low-level jet during weak winds and directional changes during strong winds occurred further above. The latter will be investigated in section 3.2.1.

### 3.1.2. Radiation and energy balance

Situated at the end of polar night the measuring period's radiation regime was still dominated by longwave radiative transfer. The radiation balance, recorded by the BSRN station (Fig. 3.3a) shows an increasing daily maximum global radiation  $K \downarrow$  of  $21 \text{ W m}^{-2}$  to  $81 \text{ W m}^{-2}$  while absolute longwave radiation (both incoming and outgoing) ranged between  $130 \text{ W m}^{-2}$  and  $290 \text{ W m}^{-2}$ .

In consequence, the net radiation  $Q_s^*$  (see Eq. 1.1) was mostly defined by longwave radiative cooling of the surface ( $I_{net}$  in Fig. 3.3b), resulting in positive (upward)  $Q_s^*$  during more than 90% of the time and up to  $75 \text{ W m}^{-2}$ . Exceptions are a few daytime periods where  $I_{net}$  was close to zero and diffuse shortwave radiation gained significant impact, lowering  $Q_s^*$  down to  $-10 \text{ W m}^{-2}$ . Direct shortwave radiation only occurred during two short periods on 09.03. and 10.03.2020.

The albedo ( $\alpha = \left| \frac{K \uparrow}{K \downarrow} \right|$ ) was calculated for each day's highest 5% of  $K \downarrow$  to avoid unrealistic values when the magnitudes converged to zero. The resulting daily average ranged from 0.70 to 0.85 with no significant trend ( $p$ -value = 0.44). These values match the observations of former years in Ny-Ålesund during the spring months, mostly ranging between 0.7 and 0.9 (see Fig. 8 in Maturilli et al., 2015) and correspond to tabular values, lying slightly below the expected albedo of clean snow (0.75 to 0.98, see Geiger et al., 1995, Tab. 4-2).

As outlined, net radiation mostly indicated an energy loss, cooling the surface. During periods especially at the beginning and end of the campaign, most of the respective energy was provided by soil heat flux, ranging down below  $-50 \text{ W m}^{-2}$  (Fig. 3.4). This is surprising since  $Q_G$  below a snow cover has been observed to range from only  $-2 \text{ W m}^{-2}$  to  $-15 \text{ W m}^{-2}$  in midwinter in Canada (Helgason and Pomeroy, 2012) with an average of  $-8.3 \text{ W m}^{-2}$ . Iwata et al. (2008) observed similar values for snow depths less than 15 cm and flux from only  $-1 \text{ W m}^{-2}$  to  $-5 \text{ W m}^{-2}$  for more than 30 cm thick snow cover in Japan.

However,  $Q_G$  under snow not only depends on snow thickness but also on its density with new, light snow having a 17 times lower thermal molecular conductivity than old snow (Foken, 2017, Ch. 1.4.2 after Stull, 1988, App. C, p. 643). Since no measurements of snow depth and density are available, it might be valuable for further investigations to verify the results with other soil sensors close by.

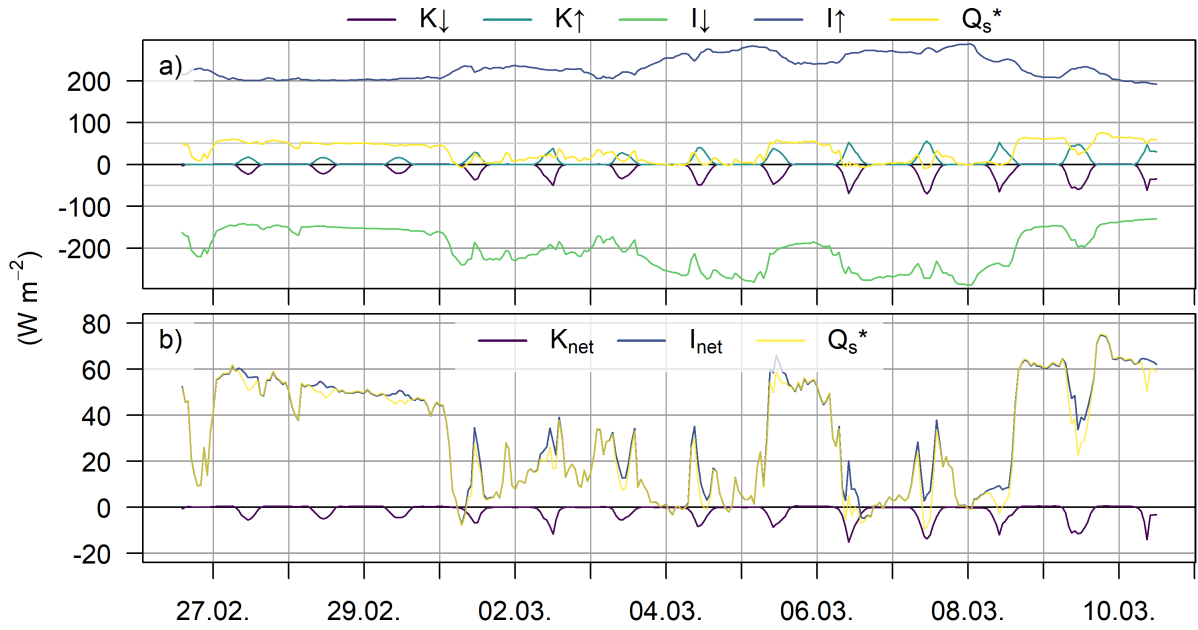


Figure 3.3.: Radiation data recorded by the baseline surface radiation network over the whole measuring period (26.02. - 10.03.2020). a) shows the radiation balance with shortwave incoming radiation ( $K_{\downarrow}$ ), the shortwave reflex radiation ( $K_{\uparrow}$ ), incoming and outgoing longwave radiation ( $I_{\downarrow}$  and  $I_{\uparrow}$ ) and the net radiation ( $Q_s^*$ ). b) displays the shortwave and longwave net radiation, supplemented by  $Q_s^*$ . The data fulfill the sign convention of positive fluxes away and negative towards the surface and are aggregated from 1 min to 60 min.

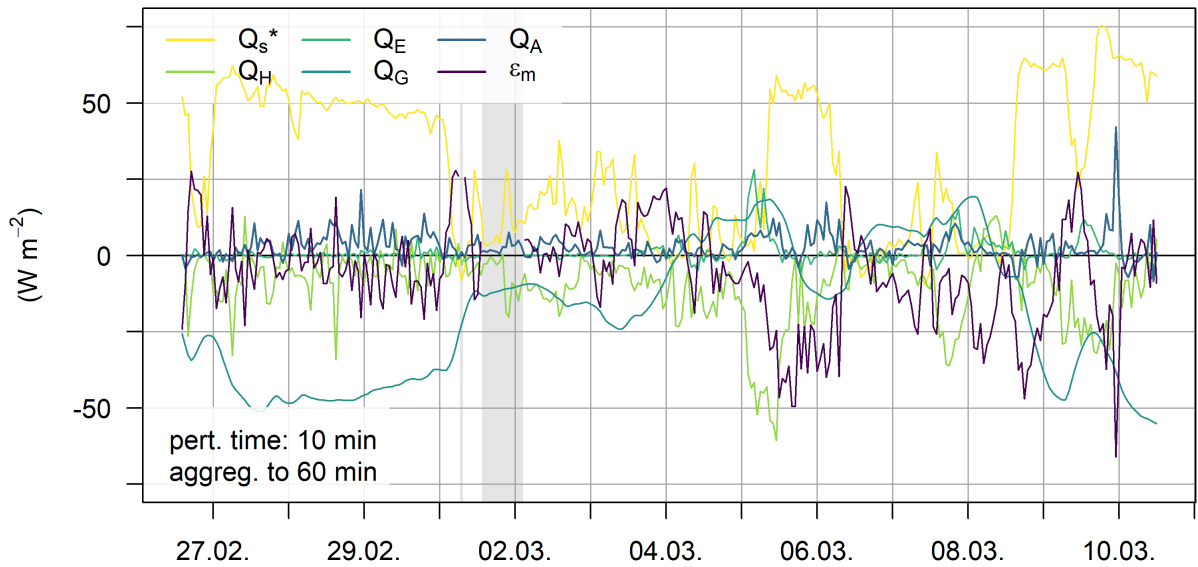


Figure 3.4.: Time series of the surface energy balance (see Eq. 2.5) for the whole measuring period (26.02. - 10.03.2020). The components are net radiation  $Q_s^*$ , turbulent sensible and latent heat flux  $Q_H$  and  $Q_E$ , respectively, soil heat flux  $Q_G$  and horizontal advection of sensible heat  $Q_A$ , calculated according to equation 2.4. The turbulent quantities were computed with 10 min perturbation time scale and  $Q_A$  was calculated on a temporal resolution of 2 min. All other quantities were recorded with 1 min resolution. All time series were then aggregated to a 60 min resolution on which the residual term  $\epsilon_m$  was computed according to equation 2.6. The gaps in  $Q_E$  and  $\epsilon$  on 01.03. and 02.03.2020 are caused by instrument failure, marked by the light-grey vertical bars. The data fulfill the sign convention of positive fluxes away from and negative towards the surface.

The turbulent sensible heat flux  $Q_H$  was mostly directed towards the surface, ranging down to  $-60 \text{ W m}^{-2}$ , and took essential part in compensating the radiative cooling whenever it was large. An exception are the first days until the 29.02.2020 when the flux was small despite a large upward  $Q_S^*$ , forcing large heat flux from the soil. The only period with constantly positive  $Q_H$  was observed on 08.03.2020, where a low-pressure system advected cold air from the North Pole region (App. A.12). This cold-air advection caused an abrupt temperature drop of more than 13 K within 8 h (Fig. 3.1a and App. A.11), resulting in colder air above a warmer snow surface (App. A.9d) and hence a reversed gradient and positive (upward)  $Q_H$ .

The turbulent latent heat flux  $Q_E$  contributed least to the surface energy balance, which was to be expected due to the low temperatures and hence low humidity. There were, however, some exceptions with larger upward  $Q_E$ . These periods with strong positive latent heat flux mostly went along with winds along the fjord axis, predominantly from ESE (see App. A.5a). While this direction also featured high values for specific humidity  $Q$  (see App. A.5b), large  $q$  could only explain part of the high latent heat fluxes (see App. A.6). Hence, the generally stronger winds along the fjord and hence stronger turbulence were mostly responsible for the larger magnitudes of  $Q_E$ .

Horizontal advection of sensible heat ( $Q_A$ ) was mostly positive, depicting a heat drainage from the site. The 5<sup>th</sup> and 95<sup>th</sup> percentile on the raw resolution (2 min, see App. A.7) were  $-10$  and  $19 \text{ W m}^{-2}$  respectively with  $4 \text{ W m}^{-2}$  being the median absolute magnitude. The distribution of  $Q_A$  shows a dependence on wind direction with largest magnitudes associated with presumably katabatic flows from SSW, down the slopes of the Zeppelin mountain and Brøgger glacier (see App. A.7). While this sector featured some fluxes of large heat gain ( $Q_A < 0 \text{ W m}^{-2}$ ), atypical for katabatic flows, the majority of the large fluxes refers to a drainage of heat, corresponding to the expectation of down-slope density currents.

$\epsilon_m$  (see Eq. 2.5) shows the imbalance of the surface energy balance. During the first part of the campaign it fluctuated around or below zero, followed by periods where  $\epsilon_m$  was positive. Hence, only considering the displayed quantities, less energy was transported away from the surface than towards it. From 05.03.2020 on this was mostly inverted. This lack of energy at the surface, causing a non-closed surface energy balance is termed ‘runaway cooling’ and is a common issue in land surface models (Foken, 2008).

Including  $Q_A$  in the balance generally did not reduce the non-closure of the surface energy balance since the residuum with  $Q_A$  excluded ( $\epsilon_m$ ) was not systematically smaller than the residuum still containing  $Q_A$  ( $\epsilon$ , see App. A.8). This was evident in the relation between  $Q_A$  and  $\epsilon$ : Assuming  $Q_A$  to be the major contributor to the residual ( $Q_A \approx \epsilon$ ), one would expect a positive correlation between  $Q_A$  and  $\epsilon$  which was not found (see Fig. 3.5a). Instead, most of the largest magnitudes of  $Q_A$  coincided with small magnitudes of  $\epsilon$ . Consequently,  $\epsilon$  appears to be determined by at least one of the remaining, not resolved components, whose sum  $\epsilon_m$  (see Eq. 2.6) is anti-correlated to  $Q_A$  (see Fig. 3.5b). These components are mainly heat storage, vertical divergence of radiation and flux and uncertainties of the measurements. Regarding the latter it has to be noted that computing the surface energy balance was not originally intended and hence the setup not ideal: The radiation measurements at the BSRN were separated from the turbulence station for  $Q_H$  by 50 m and for  $Q_E$  and the soil heat flux plate by about 300 m

while  $Q_A$  was computed for a location in between. The resulting different depicted footprints in the presence of a horizontally heterogeneous surface might well contribute to a non-closure of the surface energy balance.

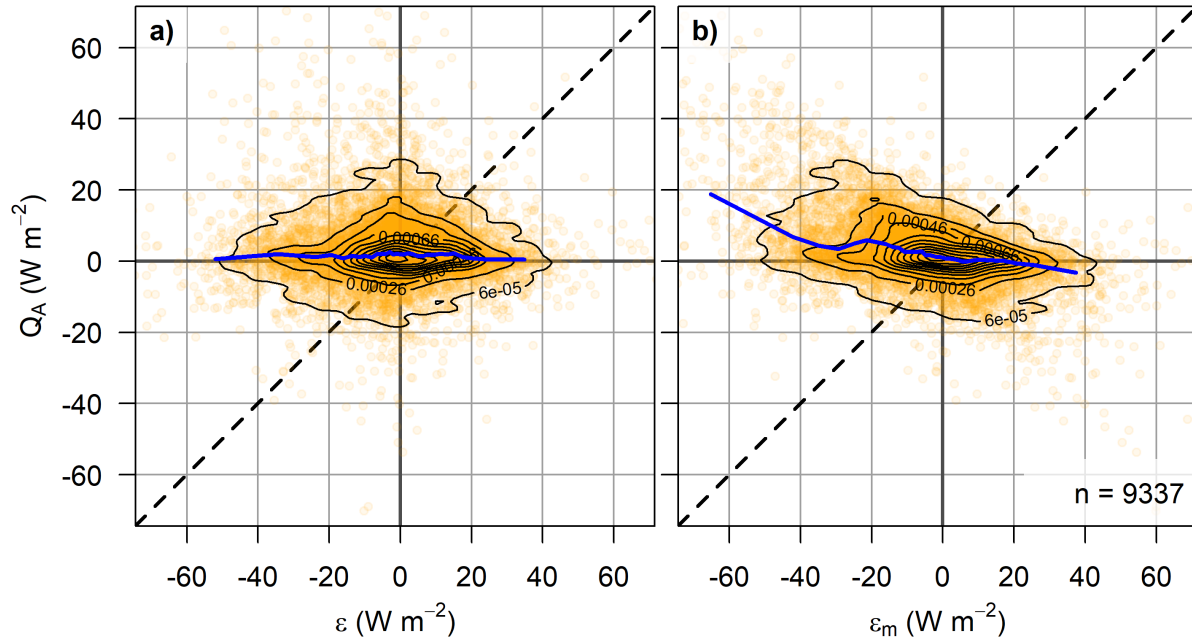


Figure 3.5.: Horizontal advection of sensible heat  $Q_A$  (see Eq.2.4), against (a) the residual of the surface energy balance  $\epsilon$  (see Eq. 2.2) and (b) the modified residual  $\epsilon_m$  (see Eq. 2.6) from which  $Q_A$  is excluded. The contour lines depict the point density while the blue solid lines are bin medians with a bin width of 300 data points. The black, dashed line is the 1:1 relation.  $n$  represents the sample size, which covers the whole measurement period from 26.02. until 10.03.2020 with a temporal resolution of 2 min.

## 3.2. Boundary layer regimes (RQ 1)

### 3.2.1. Topography as wind determinator (H 1.1)

All dominant wind directions at the research site lay between around  $80^\circ$  and  $320^\circ$  (see Fig. 3.6). Northerly winds have been found to occur only during the summer months when the snow-free land surface heats up, establishing a sea breeze (Maturilli et al., 2013).

Wind velocity and direction were strongly interconnected: While winds from the open ocean in the NW ( $270^\circ$  to  $320^\circ$ ) were almost exclusively above  $4 ms^{-1}$ , the opposite direction from ESE featured strong as well as medium winds around and below  $2.5 ms^{-1}$ . The directions of strong winds were well aligned with the orientation of the fjord that channeled the synoptic flow between the adjoining mountain ridges. The weaker flows from the SE-sector had a slightly more southerly direction than the strong winds. According to Beine et al. (2001), these are katabatic flows from the Kongsvegen glacier at the inner end of the fjord, about 10 km south-east of Ny-Ålesund (bottom right in Fig. 2.1a).

Southerly and south-westerly directions corresponding to the SW-sector showed predomi-

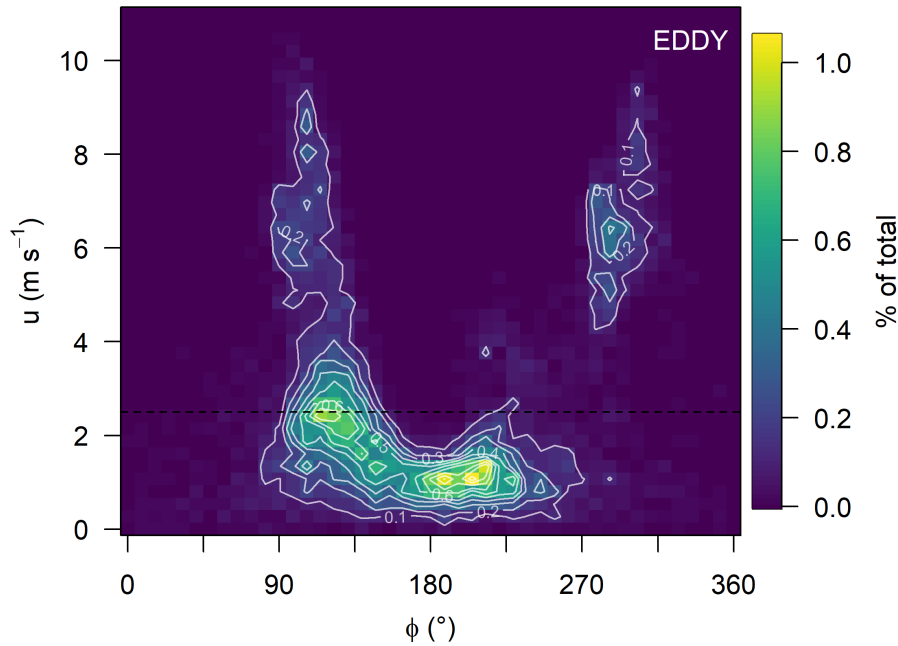


Figure 3.6.: 2D histogram of wind speed and direction recorded by the ultrasonic anemometer (USA) at the EDDY tower, covering the whole measuring period (26.02. - 10.03.2020). The pixel size is  $x = 8^\circ$  and  $y = 0.25 \text{ m s}^{-1}$ . The color indicates the percentage of total with a distance between contour lines of  $0.1 \%$ . The dashed line visualizes the wind speed threshold of  $2.5 \text{ m s}^{-1}$  (see Sect. 2.5.3).

nantly weak winds of around  $1 \text{ m s}^{-1}$  coming down the slopes of the Zeppelin mountain and Brøgger glacier (see Fig. 2.1a) and prompting katabatic flows. These directions have also been observed by Jocher et al. (2012) and Maturilli et al. (2013). Especially Maturilli et al. (2013), however, found south-westerly winds to be less frequent, specifically for the spring months that correspond to the observational period in this thesis. Since the measurement location of Maturilli et al. (2013) was located at the BSRN, being farther away from the mountain slopes than the NYTEFOX site, this hints towards katabatic flows being increasingly superimposed by along-fjord flows with increasing distance from the mountain slopes.

Further insight is provided by the BL regimes, categorizing the campaign period in windows by their wind speed  $U$ , wind direction  $\varphi$ , longwave incoming radiation  $I \downarrow$ , static stability and meandering intensity, as outlined in section 2.5.3. Out of the 960 possible combinations of these parameters 67 occurred during the campaign (see App. A.13). 32 regimes occurred at least twice, covering 84% of the windows and are shown in figure 3.7.

The most frequent regime represents classic weak synoptic forcing, expressed by low wind speeds and low  $I \downarrow$ , implying clear sky and facilitating radiative surface cooling (see Fig. 3.7). Thus, it is characterized by statically stable conditions. The wind direction varied between more than one sector, corresponding to the high meandering intensity.

When taking all weak-wind windows into account, not just regime # 1, the vast majority (88%) had varying wind direction while steady winds from the SW-sector from Zeppelin mountain and Brøgger glacier covered 9%. 3%, corresponding to three windows, featured along-fjord winds, all from the SE-sector. This wind direction, however, is not represented by the synoptic



A comparison between the wind direction close to the ground and at higher altitude allows to evaluate, whether the along-fjord flows were a channeling effect of the mountains or just coincided with synoptic forcing along the fjord axis. The SODAR shows along-fjord winds as dominant direction during strong winds even up to the maximum observation height of 250 m a.g.l. (see Fig. 3.2), not proving a channeling influence. Hence, a visual evaluation of the large-scale synoptic wind direction above the BL over the Kongsfjord was done for all strong wind windows with along-fjord flow at the surface, based on the ECMWF Reanalysis v5 (ERA5) for the 850 hPa level. Windows, where north-westerly flows were observed near the ground, also showed synoptic flows from NW and NNW at higher altitudes. Since these directions align, a channeling effect can not be confirmed. For the periods, where strong winds near the surface were observed from SE, however, the direction of synoptic flows at 850 hPa varied: A large portion of flows came from SSE to SSW, supplemented by winds from N and NNE and even WSW to WNW. None of the windows showed the easterly or south-easterly winds that were observed at the surface. The wide variety of synoptic directions rules out the Ekman spiral as cause for the directional difference (Holton, 2004, Sec. 5.3.4), leading to the conclusion, that all strong wind periods from the SE-sector were subject to redirecting and channeling effects of the island's topography.

The evidence from the direct relation of wind speed and direction (see Fig. 3.6) as well as the regime constitution confirms both parts of hypothesis H 1.1:

- a) Strong winds almost exclusively blew along the fjord, mostly channeled by the surrounding mountains.
- b) For almost all weak-wind cases, winds came either down the slopes of the Zeppelin mountain and the Brøgger glacier or had variable direction. Local topography appears to have been the driving force since the wind directions during weak winds observed close to the ground were often in contrast to those observed in greater heights (Fig. 3.2). The heights of the transition between directions ranged across the whole height spectrum of the SODAR (up to 250 m a.g.l.).

The density-driven currents during calm conditions are likely to occur at the entire glacier-covered mountain range along the Kongsfjord. Assuming that all adjoining mountains drain air towards the fjord, whose only outlet is towards the ocean in the NW, one might imagine the fjord valley to act like a watershed. The air currents cumulate at the fjord where they are redirected towards NW, joining the draining flows from the Konsvegen glacier at the fjord's inner end.

This scenario would explain the lower frequency of south-westerly flows closer to the fjord by Maturilli et al. (2013). It would also add to the explanation of the frequent weak winds from SE (see Fig. 3.6), which so far were assumed to be katabatic currents solely from the Konsvegen glacier (Beine et al., 2001).

The high frequency of varying wind directions during weak winds further suggests that the research site was located in the area where the downhill current from SW meets the weak

along-fjord flows. A varying relation of their strengths would result in an alternating dominance at the location of measurement, resulting in meandering motions and hence changing wind direction. This will be discussed in further detail in section 3.2.3.

As outlined, this behavior may be limited to the location of the measurement, though, which is separated from the foot of Zeppelin mountain by about 0.9 km and 2.4 km from the snout of the Brøgger glacier. Closer to the steep slopes the drainage flows might prevail while the opposite applies for locations further away as supported by the less frequent observations of south-westerly flows closer to the fjord.

While the discussed weak- and strong-wind regimes covered two thirds of the campaign period, the remaining third showed intermittent wind speeds (category 0). Some of these have winds coming from ESE along the fjord, presumably weaker synoptic flows which were still strong enough to superimpose gravity-driven density currents perpendicular to the fjord. Most of these windows, however, had varying direction, suggesting dominant katabatic flows of low velocity interrupted by stronger gusts along the fjord axis.

These intermittent periods are included in all analyses not specifically sub-setting for wind-speed regimes. However, the individual wind-speed characteristics of these windows are not specifically investigated which might be subject to subsequent studies.

#### **3.2.2. Wind speed and cloud cover as proxy for submeso-scale motions (H 1.2)**

The time scale-dependent spatial variance (power spectrum) in temperature and wind speed along the horizontal fiber-optic cables is used as an indicator for motions on the respective time scales.

The power spectra for regimes with  $I \downarrow$  category 2 and 3 showed very similar characteristics (compare left and right column in App. A.17) and were combined for the subsequent analyses. This combination will hereafter be called ‘cloudy’ in contrast to ‘clear sky’ for  $I \downarrow$  category 1. The temperature variance on the smallest scale of 9 s was almost constant across all regimes irrespective of wind speed and cloudiness (Fig. 3.8a - d) while it diverged between conditions with increasing scale: During calm, clear-sky conditions the variance increased to a maximum at about 10 min (Fig. 3.8a) while it decreased until about 5 min for strong-wind, cloudy conditions (Fig. 3.8d). Calm but cloudy periods showed a wide range of characteristics, covering those of both before-mentioned regimes (Fig. 3.8b) and suggesting an influence of wind speed and  $I \downarrow$  on temperature variance on the same order of magnitude. Windows with clear skies during strong winds occurred only twice with variance within the range of weak-wind, cloudy conditions (compare Fig. 3.8b and c). The small sample size, however, does not allow for a meaningful interpretation.

The variance in horizontal wind speed showed a different characteristic. Small-scale variances were generally higher than for temperature with a large increase towards strong-wind conditions (Fig. 3.8e - h). Hence, the small-scale variance that was not resolved by the temperature field increased with increasing wind speed due to intensifying shear-generated mixing which diminished all spatial temperature differences. With increasing time scale, however, the char-

acteristic differences between temperature and wind-speed variance converged. Motions on submeso scales, larger than about 1 min, hence, were far better represented by the temperature field than the short-lived convective turbulence.

While wind speed variance in the strong-wind, cloudy regime decreased monotonically, it had a local minimum during calm conditions at around 36 s and 1:12 min. The power increased from there, indicating submeso-scale processes on time scales of more than 1 min. While many of the windows during calm and cloudy conditions showed a maximum power around 20 min, this power increased up to the maximum resolved time scale of almost 40 min during the majority of calm, clear-sky windows. Clear-sky conditions, hence, seem to favor proportionally longer-lasting structures even though this is not expressed in the temperature variance. This finding hints at differences in the space-time behavior between scalar variables such as temperature and vector variables like wind speed.

In spite of the prominent role of submeso-scale processes in the weak-wind regime, the absolute power on these scales was still not larger than during many strong-wind windows (compare Fig. 3.8e and h). This confirms the existence of submeso-scale processes under all conditions (Anfossi et al., 2005; Mahrt, 2010), though potentially of different character and not represented in the homogeneous temperature field (see Fig. 3.8d) due to convectively dissolved temperature heterogeneity. Relative to the power of short-lived turbulence, however, they only become important in the weak-wind regime.

The effect of wind speed and cloudiness can as well be seen in the MRD-scale dependent spatial Pearson correlation coefficients  $r_p$  of temperature for the different regimes, adding spatial information (see Fig. 3.9). When expressed relative to the  $r_p$  of weak-wind, clear-sky conditions, the correlation of cloudy and weak- as well as strong-wind periods about equaled 1 for time scales  $\geq 19$  min, irrespective of the separation distance (see Fig. 3.9b and c). On these scales wind speed and cloud cover, hence, had little impact on the correlations. For all shorter time scales, however,  $r_p$  decreased with increasing wind speed and cloudiness for all separation distances as shown by the relative correlations being  $< 1$ . For separation distances of up to around 50 m,  $r_p$  of the short time scales was diminished especially strong by cloud cover and even more by strong winds while this difference showed a local minimum at around 80 m. This pattern indicates enhanced structures of several but less than 80 m in the horizontal temperature field during calm, clear-sky conditions that persisted for up to around 0.5 min. All scales from 1 min to 10 min showed decreasing ratios with increasing separation distance and decreasing  $r_p$ . Hence, temperature structures of at least 220 m and on the order of minutes were favored by calm and clear-sky conditions as well.

Absolute correlations for all respective regimes are shown in appendix A.18 including correlations of horizontal wind speed observations.

During weak winds cloud cover reduces the power in all resolved time scales, most notably in the submeso-scale range. The omnidirectional  $I \downarrow$  reduces differences in surface temperature and temperature of the near-surface air that might be caused by e.g. varying  $I \uparrow$  depending on the local surface. This effect can be seen in appendix A.19 and A.20. It explains the reduction

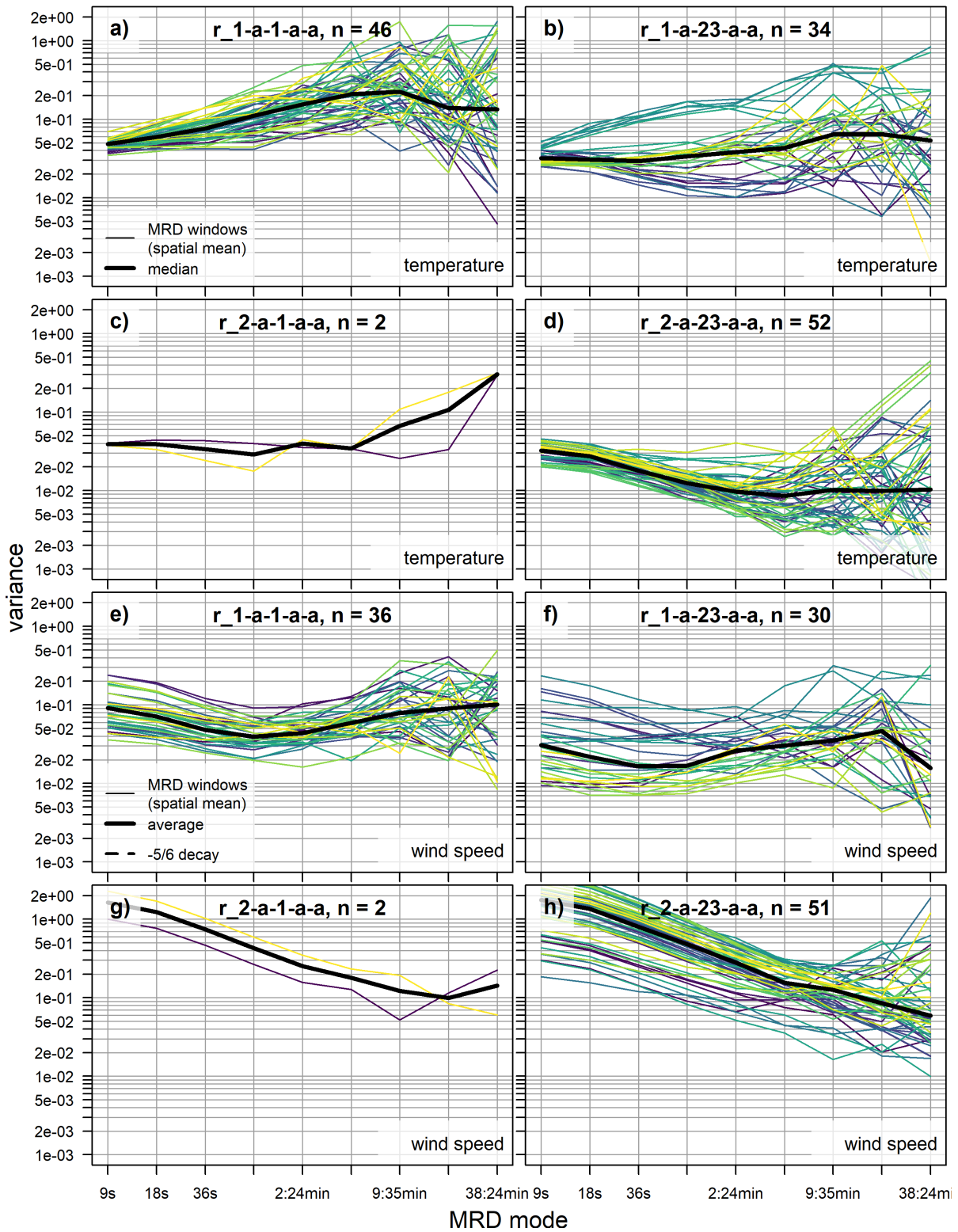


Figure 3.8.: Power spectra of fiber-optic distributed sensing (FODS) temperature (a to d) and wind speed (e to h), combined for all horizontal fiber transects except between latter (a) and (d) in figure 2.2. The data are conditionally sampled by regimes with the respective regimes categories according to table 2.1 stated by each plot's title: The parameters (wind speed, wind direction, longwave downwelling radiation, static stability and meandering intensity) are separated by hyphens. 'a' refers to all categories (no sub-sampling), two digits to two categories. Hence, the rows subset by wind speed (1 = weak vs. 2 = strong) and the columns by longwave downwelling radiation (1 = weak vs. 23 = medium and strong). The variance on the y-axis is plotted logarithmically, the x-axis shows the dyadic multi-resolution decomposition (MRD) modes. The colored lines are the variances of single MRD windows, colored chronologically to reveal temporal effects. The bold line connects the medians of each mode.

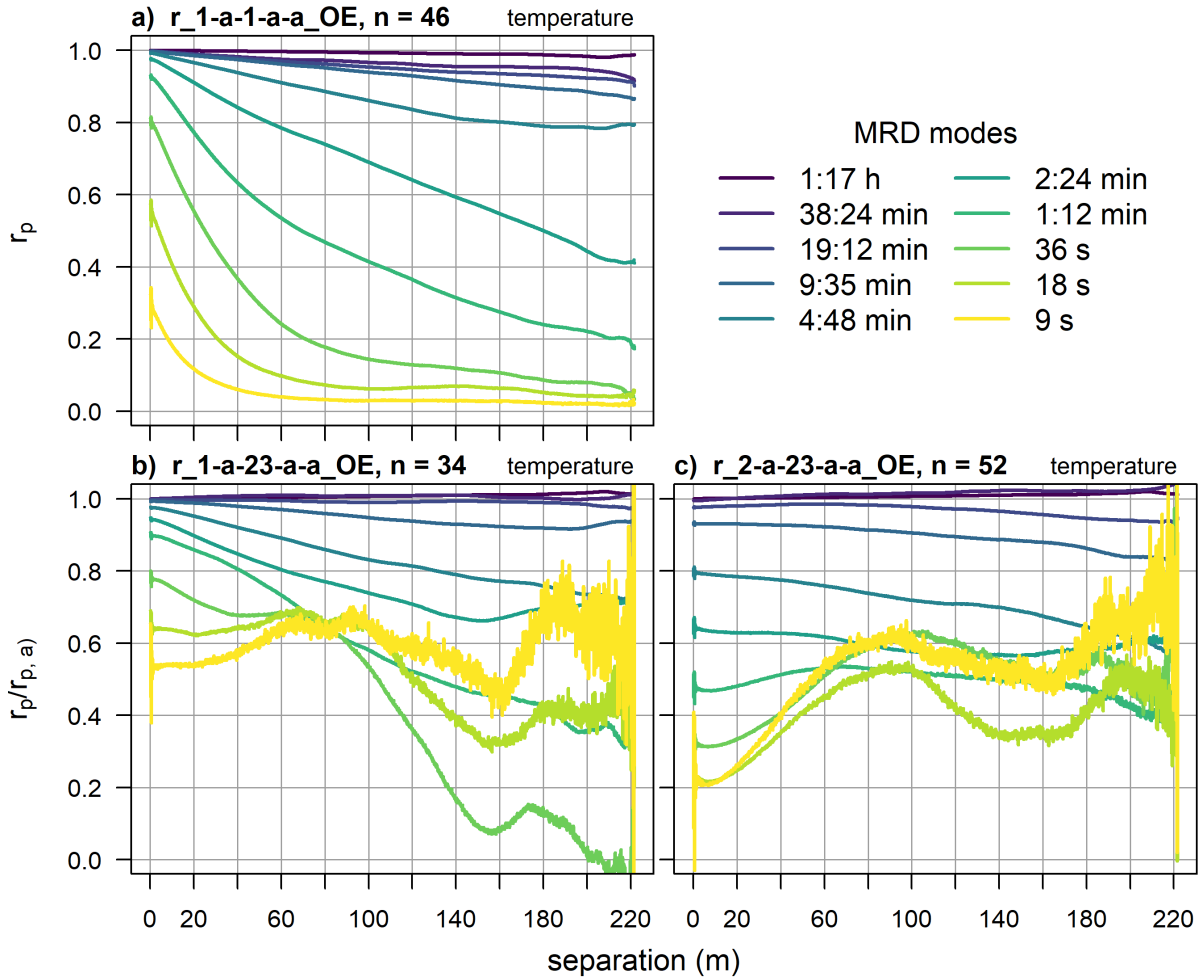


Figure 3.9.: Spatially aggregated Pearson correlation coefficients  $r_p$  for the fiber-optic distributed sensing (FODS) temperature observations of the transect OBSE-EDDY by separation distance and for the different multi-resolution decomposition (MRD) modes. The regime encoding is as described below figure 3.8. Absolute  $r_p$  is plotted for weak wind and weak longwave downwelling radiation (a) while for medium to high radiation and weak (b) as well as strong winds (c) the correlation is plotted as ratio:  $r_p$  of the respective regime divided by  $r_p$  of a.

of motions driven by local temperature gradients since it limits their available energy. It also explains the especially large impact of cloud cover on temperature variance in contrast to wind speed variance since it reduces the temperature signature of the motions that can be generated. High wind speeds also reduce the temperature variance. However, the power in the motions themselves, which is better expressed by the wind-speed variance, is larger or equal during strong winds for even most of the submeso-scale range. Hence, strong winds do not reduce the power in motions on most part of the submeso scale. However, in contrast to short time scales, the power on longer scales is not reduced during calm conditions, resulting in a relative increase of structures on these scales and their importance for BL processes.

These relatively enhanced structures were found on spatial scales of decameters to several hundreds of meters and time scales of several seconds up to around 10 min for the temperature field and minutes to at least 40 min for the wind field.

The hypothesis that weak winds and clear skies promote motions on the submeso-scale (H 1.2) was, hence, partly confirmed. Both drivers enhanced the temperature variance on longer time scales and the assumed impact of cloud cover was also verified for wind speed variance across the whole resolved submeso-scale range. Weak winds, however, only proved to favor the relative contribution of motions on the submeso scale while the expected impact on the absolute power was just found for the largest time scales.

#### **3.2.3. Occurrence and generation of meandering (H 1.3)**

A phenomenon that might introduce variance on the submeso scale are abrupt wind-directional changes termed meandering. Periods with meandering motions were identified based on the BL regime windows according to section 2.5.4.

Strong meandering (cat. 3 and 4, see Tab. 2.1) occurred during 89% of weak-wind windows while it was detected during only 2% of the strong-wind windows. Since strong winds force the flow along a predominant axis, they suppress meandering motions. During weak winds, however, different flow-generating mechanisms with different or varying direction may occur on the same order of power with alternating dominance.

Meandering, however, was also detected for 67% of the windows with intermittent weak and strong winds, emphasizing the assumption that wind speed intermittency promotes meandering wind directions. This may either be due to gusts which interrupt e.g. katabatic flows from a different direction (see Sect. 3.2.1) or due to a synoptic flow intermittently and locally becoming weaker than a katabatic current.

The wind direction distribution during meandering periods varied greatly from periods with no or weak meandering. While the latter showed narrow peaks at the directions along the fjord axis (Fig. 3.10a) and a minor for winds from Zeppelin mountain (Fig. 3.10b), the meandering regimes featured a broad and almost continuous range from easterly to southerly and westerly winds with maxima at SE (along the fjord) and SW to SSW (from Zeppelin mountain and Brøgger glacier) (Fig. 3.10c and d).

Wind-directional shifts between the SW-sector (downhill) and the SE- or NW-sector (along the fjord) were far more frequent during meandering intervals. While such changes only happened

around every 2 h to 5 h during weak or no meandering (cat. 2 and 1), they occurred on average every 26 min for meandering category 3 and every 18 min during category 4. These shifts, however, included higher frequent oscillations across the sector margin during some of the main direction shifts and hence overestimate the frequency of the meandering strokes. During two 24 h example periods (Fig. 3.11), the visually determined frequency appears to have been rather around 0.5 h for both category 3 and 4 meandering.

Said example periods showed directional changes during category 4 meandering often spanning and exceeding the complete SE- and SW-sectors (Fig. 3.11a). Category 3 meandering only ranged between around 120° and 220°, alternating between the core zones of the SE-sector (along the fjord) and SW-sector (downhill) (Fig. 3.11b).

The winds from the SW-sector were characterized by exceptional cold temperatures, qualifying these as gravitational driven katabatic currents down the adjoining slopes (see App. A.2.1 and A.21). The SE-sector was aligned with flows from the Kongsvegen glacier, whose draining cold-air currents are known to cause southeasterly flows in Ny-Ålesund (Beine et al., 2001). That these flows arrived as relatively warm air at the measurement site (see App. A.21) is explained by their 10 km travel across the warmer fjord.

The outlined results confirm hypothesis H 1.3. Meandering required periods of weak wind to develop which, however, might optionally be interrupted by stronger winds.

The observations further prompted the necessity of two flow-generating mechanisms which, at least locally, alternate in dominance, to develop meandering in the given environment. This may be:

- a weaker synoptic flow and a local, submeso-scale flow. This presumably caused meandering during the periods with intermittent winds where a synoptic flow along the fjord was temporarily and locally weaker than katabatic flows down the adjoining slopes.
- two local, submeso-scale phenomena such as the two competing katabatic currents of different origin, found during calm conditions.

The suggested necessity of two flow mechanisms does not apply for conditions where e.g. vortex shedding might create a meandering wind direction downstream of a topographic flow obstacle. However, the distribution of wind directions during meandering periods indicated no such mechanism for this study.

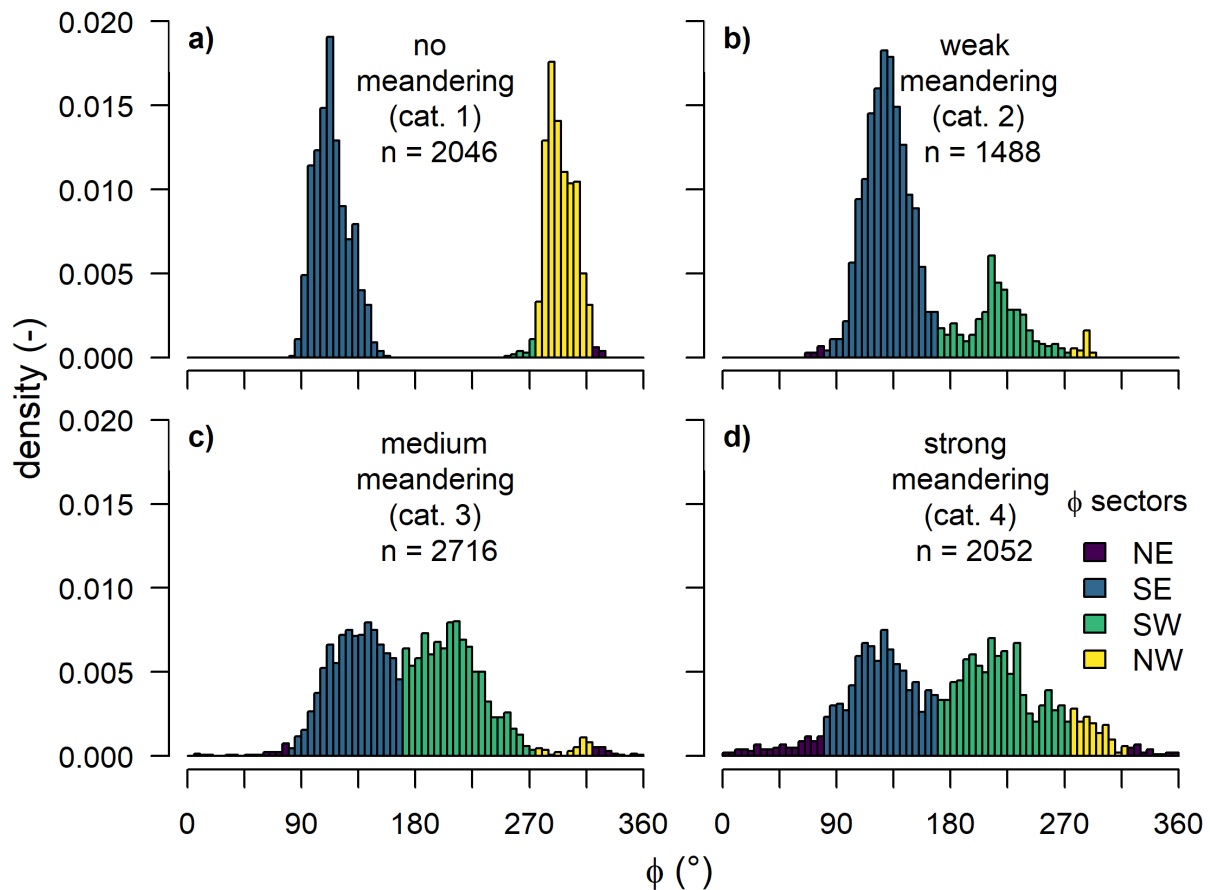


Figure 3.10.: Density histogram of wind directions for all regime windows with meandering category 1 to 4 (see Tab. 2.1) in sub-figure a to d respectively. Directions are recorded by an ultrasonic anemometer at the EDDY tower with a perturbation time scale of 2 min. Colors denote the wind direction sectors, also listed in table 2.1 while  $n$  is the number observations in each sub-figure.

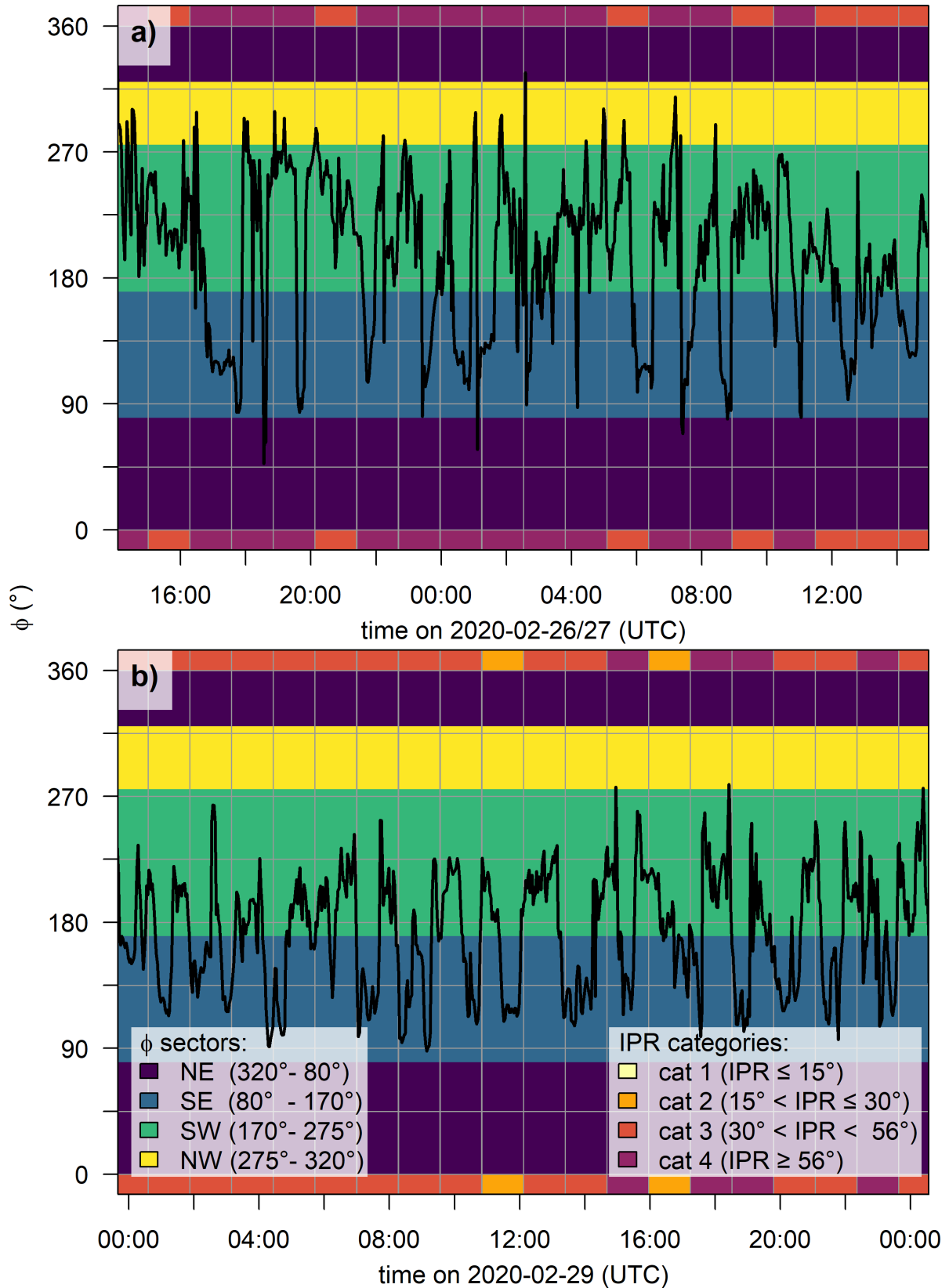


Figure 3.11.: Time series of wind direction  $\phi$  on the 26/27.02.2020 (a) and 29.02.2020 (b). Directions have a temporal resolution of 2 min and were recorded by the ultrasonic anemometer at the EDDY tower. Wind direction sectors are marked by horizontal, meandering category by vertical colored bars, visible at the top and bottom.

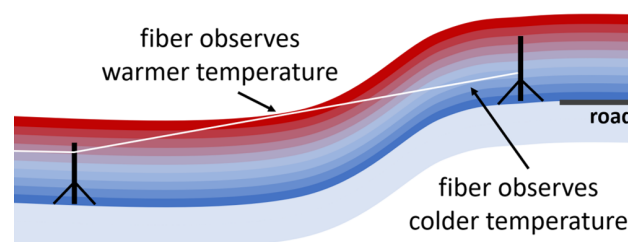
### 3.2.4. Varying influence of local topography (H 1.4)

The time-averaged spatial temperature deviations along the fiber transect between EDDY and BSRN showed a distinct spatial pattern during weak winds (Fig. 3.12a) with a range of 0.79 K. This pattern was almost eroded by strong winds (Fig. 3.12b), where the amplitude of the average across the transect was only 0.17 K. Both cases had an overall trend of higher temperatures towards the BSRN tower at the eastern end of the transect, though much weaker during strong winds. Since the study site was located east of the northward outflow of the Brøgger glacier, this trend especially during weak winds with frequent katabatic flows (Sect. 3.2.1) may be caused by the western end being stronger influenced by cold air draining the glacier.

Also the dominant smaller-scale deviations were tied to orographic features. The trend of increasing temperature with distance from the EDDY tower was reversed for the 70 m before the first road (100 m to 170 m in Fig. 3.12a), while temperatures were higher again across the road. This points towards accumulation and northward diversion of draining cold air from the Zeppelin mountain and Brøgger glacier by the road embankment, which obstructed the flow. Said mechanism might also explain the temperature depression centered between the roads (215 m to 235 m).

This temperature depression, however, could also be influenced by the locally reduced snow cover (see bottom panel in Fig. 2.2). During daylight conditions one would expect the opposite effect with higher temperatures above bare soil than snow due to the positive snow-albedo feedback (Schlögl et al., 2018), resulting in a warming surface. However, during polar night and a radiative cooling of the surface (see Sect. 3.1.2), the soil cools the near surface air where it lacks an isolating snow cover. This effect was also visible at around 80 m to 100 m, where the transect crossed an old railroad track running in a shallow, snow-filled indentation. While temperatures were lower over a slightly elevated section uphill, where the snow had been blown off, the track itself protruded with higher temperatures. This impact of patchy snow cover was mostly homogenized during strong winds (see Fig. 3.12b).

The drastic temperature drops towards the thickly snow-covered road embankments, preceded by local temperature optima, seem to object the proposed coherence of air temperature and snow cover. The deviating characteristic is also not explained by cold-air pooling since it was a two-sided effect on both the up- and down-hill sides of the roads. Instead, these temperature perturbations were most likely an artifact of the fiber height a.g.l.: The tightly strung fibers did not closely follow the surface. To partly compensate for the concave surface towards the roads, fibers at the crossings were mounted slightly lower than average while they still hang higher above the feet of the embankments, as sketched below:



Assuming stable stratification during weak winds and hence an increasing temperature with height, this translates into higher observed temperatures above depressions such as the embankment feet and lower above elevations like the roads.

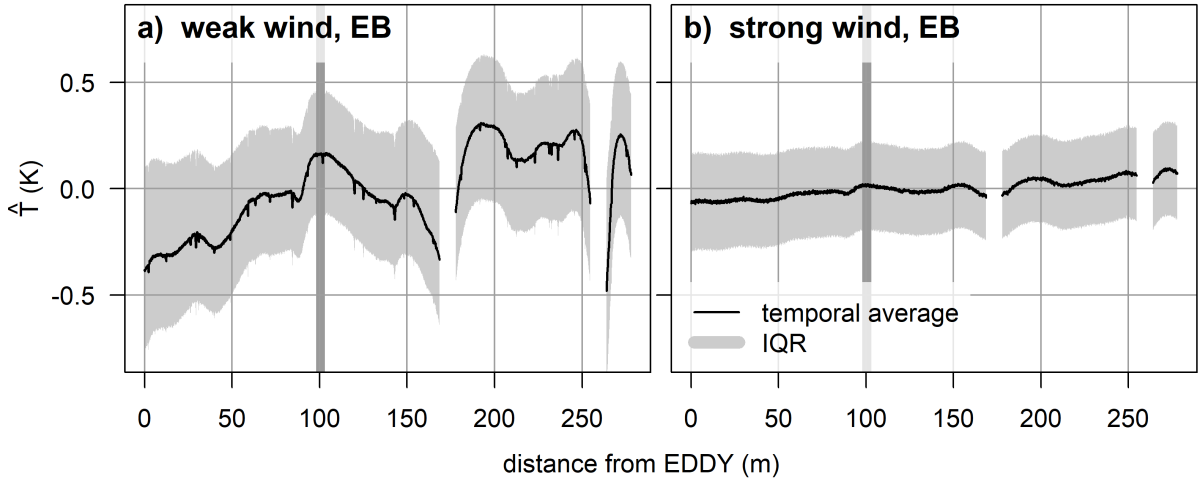


Figure 3.12.: Temperature deviation from the spatial average ( $\hat{T}$ ) for the fiber-optic distributed sensing transect from the EDDY tower to the BSRN tower. The grey areas mark the interquartile range (IQR) while the solid line is the temporal average. a) covers all time windows with weak winds ( $U \leq 2.5 \text{ m s}^{-1}$ ), b) all with strong winds ( $U > 2.5 \text{ m s}^{-1}$ ). The gaps show where the transect crossed two roads and no data are available while the vertical grey bar marks the fiber section crossing an old railroad embankment running in a shallow, snow-filled indentation.

The course of MRD-scale dependent correlation coefficients of temperature and wind speed provides insight onto the impact of small-scale topography on the dynamics of the near surface air. Correlations were calculated between the ends and each bin of the transect between the EDDY and BSRN tower (see Fig. 3.13).

The correlations were independent of spatial scale and hence small-scale topography for strong winds (see Fig. 3.13c, d, g and h). During weak winds, however, the cold air channel along the first road with its deepest point at around 150m shows distinct, yet opposing, tendencies on different time scales: The temperature correlation with the EDDY tower, which stood exposed to winds from all directions, decreased for the 1:12 min time scale, indicating a decoupling, and increased for the 4:48 min scale (Fig. 3.13a). The latter generally seems to be the time scale that was most influenced by the roads with opposing direction between temperature and wind speed correlations (compare Fig. 3.13a and e). The deviations in the correlation with the BSRN tower were strongest over the road embankment instead of the gully beneath (Fig. 3.13b and f) and occurred on all scales from 1 min to 40 min, suggesting an effect of the discussed height artifact. This artifact might also explain the drop in temperature correlation right next to the second road on larger time scales.

Implications of varying snow cover were mainly visible during weak winds above the bare soil section next to the railroad where temperature as well as wind speed correlations with the EDDY tower were higher for time scales from about 5 min to 40 min (Fig. 3.13a and e). No such consistent effect can be seen for the correlation with the BSRN tower since it may be

subject to air from a different origin.

Conditionally sampled by wind direction, the temperature correlations differed largely between sectors (see Fig. 3.14). Weak winds with flows solely coming from the SW-sector (downhill from Zeppelin mountain and Brøgger glacier) approached the flow-obstructing roads about orthogonally. The respective temperature correlation coefficients on the 38:24 min time scale performed sudden drops at both roads the transect from the EDDY to the BSRN tower crossed and remained low behind them (see Fig. 3.14b). No such pattern occurred for the transect from EDDY to OBSE which was unobstructed by topographic barriers (see Fig. 3.14a). Hence, the roads acted as a barrier for motions on time scales of around 40 min. To weak winds from all other directions the roads had no such effect (see Fig. 3.14d). They caused only local perturbations in the correlation coefficients with no particular effect on the 38:24 min time scale. The extraordinary impact of the roads on specific scales, therefore, depended on the direction of inflow.

In conclusion, local topography showed little impact on the temperature field during strong winds where intense mixing homogenized spatial differences. In calm conditions, however, stationary patterns evolved, caused by topographic structures on different spatial scales:

- large-scale spatial trend by glacier outflow from close-by mountain ridge
- small-scale cold air pools or channels in front of shallow flow barriers
- small-scale temperature variations where orography caused snow cover to vary in space

The correlation coefficients also proved an impact of these features on the temperature dynamics. Local perturbations appeared on time scales larger than about 1 min to 4 min depending on the underlying process. These findings confirm hypothesis H 1.4, that topographic features gain importance for the local flow when winds and, hence, convective mixing are weak. Additionally, an impact of the orientation of obstacles towards the mean flow was shown, especially for the time scale of around 40 min.

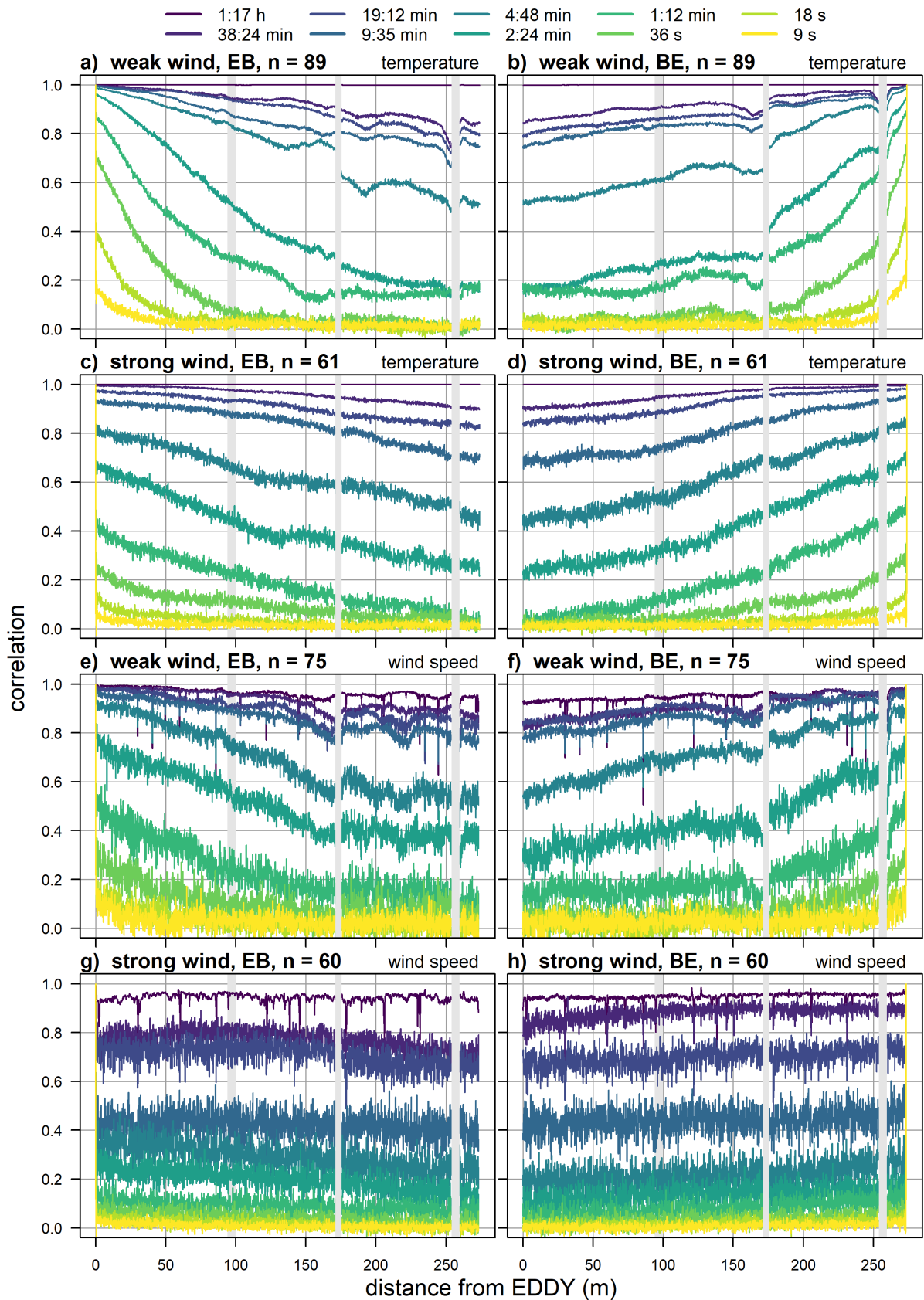


Figure 3.13.: Pearson correlation coefficients  $r_p$  between the EDDY tower (left column) and BSRN tower (right column) and all bins along the fiber-optic distributed sensing transect between those towers. Correlations for separate multi-resolution decomposition modes are represented by separate lines. a) to d) show correlations of temperature, e) to h) of wind speed data along the fiber-optic cable. The labels indicate whether all time windows with weak winds ( $U \leq 2.5 \text{ m s}^{-1}$ ) or strong winds ( $U > 2.5 \text{ m s}^{-1}$ ) are included as well as their respective number  $n$ . The spatial gaps and the vertical grey bar at around 100m are explained in figure 3.12.

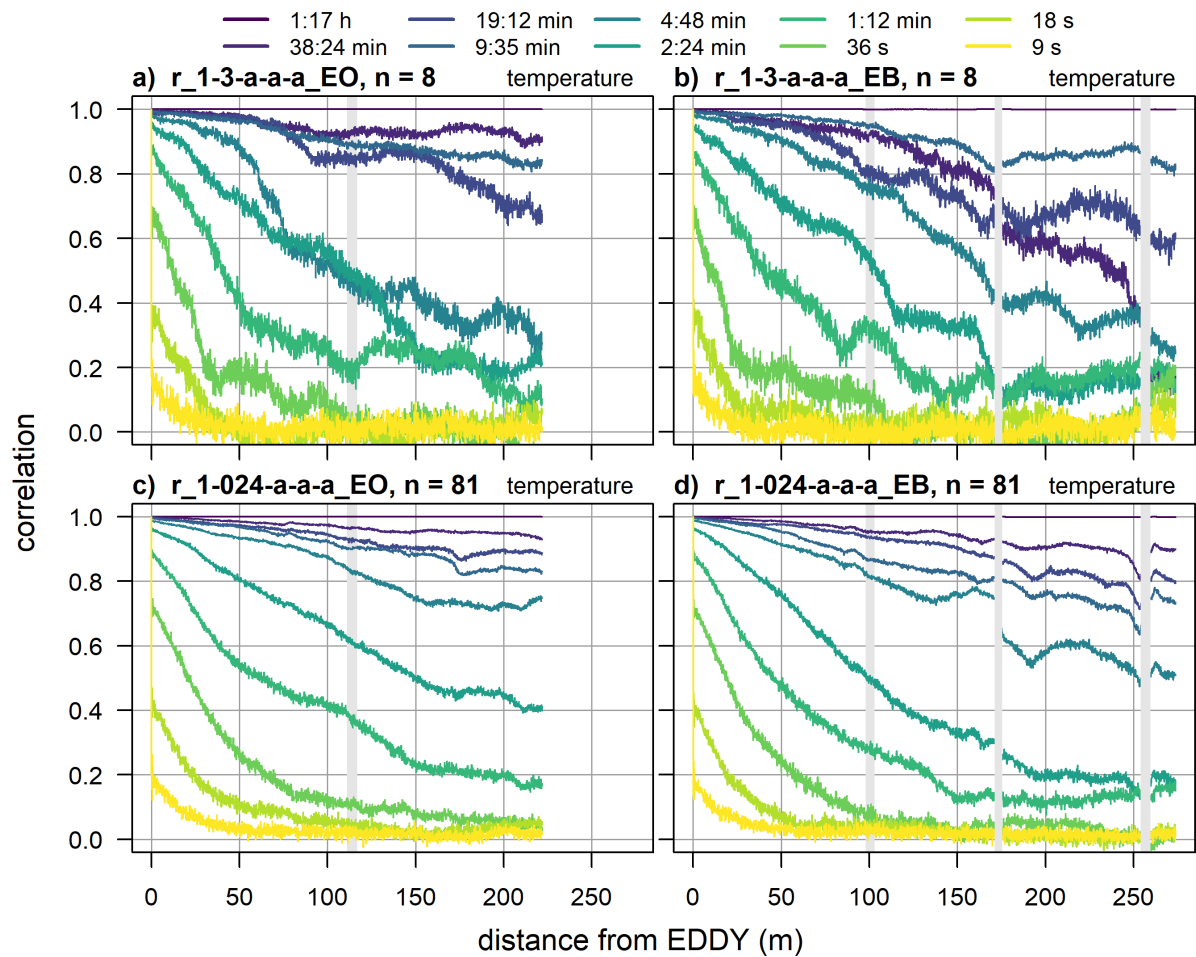


Figure 3.14.: Pearson correlation coefficients  $r_p$  as explained in figure 3.13 for the transect from EDDY to OBSE (left column) and EDDY to BSRN (right column). The first row includes all time windows with weak winds ( $U \leq 2.5 \text{ m s}^{-1}$ ) from the SW-sector (see Tab. 2.1) while the second contains all other weak-wind windows. The gaps and vertical bar in the right column are as described in figure 3.12. The grey bar in the left column marks where the railroad track crosses the transect EDDY-OBSE.

### 3.2.5. Drivers of sensible heat flux (H 1.5)

The turbulent sensible heat flux  $Q_H$  contributed significantly to the surface energy balance with high variability in time (see Fig. 3.4). Wind velocity  $U$  explained part of that variability (see Fig. 3.15a). In the weak-wind range below  $2.5 \text{ m s}^{-1}$ , where turbulence scaled little with wind speed (see Sect. 3.1.1), the line of binned medians shows a weak slope, indicating a weak coherence between  $U$  and the median  $Q_H$ . The relation between the friction velocity  $u_*$  and  $Q_H$  was stronger, with a steeper slope for small values of  $u_*$  (compare Fig. 3.15a and b). In weak winds  $Q_H$  was, hence, limited by turbulent transport. A strong, about linear, increase of downward  $Q_H$  with  $U$  appears between  $2.5 \text{ m s}^{-1}$  and  $4 \text{ m s}^{-1}$ , while for larger  $U$  the flux again scales little with wind speed. In this last range  $Q_H$  was limited by the lack of a sufficiently steep temperature gradient, which, by then, had already been mixed away. This is evident in appendix A.10a and b, proving that gradients steeper than around  $0.4 \text{ K ln m}^{-1}$  were almost only sustained for  $u_*$  below about  $0.1 \text{ m s}^{-1}$  and  $U$  below  $3.5 \text{ m s}^{-1}$  to  $4 \text{ m s}^{-1}$ . Consequently,  $Q_H$  scaled about linearly with the gradient in the very-strong wind range where it was limited by this gradient (yellow points in Fig. 3.15e).

Even though the median flux during weak winds was weak, many of the fluxes with especially large magnitude occurred during very weak winds while they did not occur during low  $u_*$  (compare Fig. 3.15a and b). This is evidence for the generation of turbulent motions from mechanisms other than bulk shear, which is represented by the mean time averaged wind speed. Hence, even though wind speed was a strong determinant of  $Q_H$ , other factors, too, must have had a large share in determining the flux.

The impact of the remaining regime parameters (wind direction  $\varphi$ , longwave incoming radiation  $I \downarrow$ , static stability  $d\Theta/d\ln z$  and meandering intensity IPR, see Sect. 2.5.3) on  $Q_H$ , however, was difficult to distinguish from indirect effects of wind speed:

- $\varphi$ : While the along-fjord wind directions featured larger fluxes than the other directions (see Fig. 3.15c), this was due to their higher proportion of strong winds. The relation between  $Q_H$  and  $U$ , however, differed little between direction sectors, at least in weak winds (see Fig. 3.16). Especially the dominant weak-wind sectors (SE- and SW-sector) behaved similar. Hence, wind direction did not impact the mean sensible heat flux during weak winds.

Only during strong winds, flows from the SE-sector (along-fjord) featured larger magnitudes of  $Q_H$  than from the opposite direction (NW-sector). This might be mainly due to the earlier discussed event of cold-air advection on the 08.03.2020, approaching from NW.

- $I \downarrow$ : There is no distinct pattern relating  $Q_H$  and  $I \downarrow$  (see Fig. 3.15d).
- $d\Theta/d\ln z$ : During the almost constantly statically stable campaign period the temperature gradient was largely determined by the mixing intensity (see App. A.10b), which, at least in strong winds, scaled with  $U$ . However, the gradient introduced a threshold for  $Q_H$  since gradients above about  $0.4 \text{ K ln m}^{-1}$  could only be sustained during weak and medium winds (see Fig. 3.15e). Hence, the gradient also had an independent impact on  $Q_H$ , causing the flux-limiting behavior discussed above.

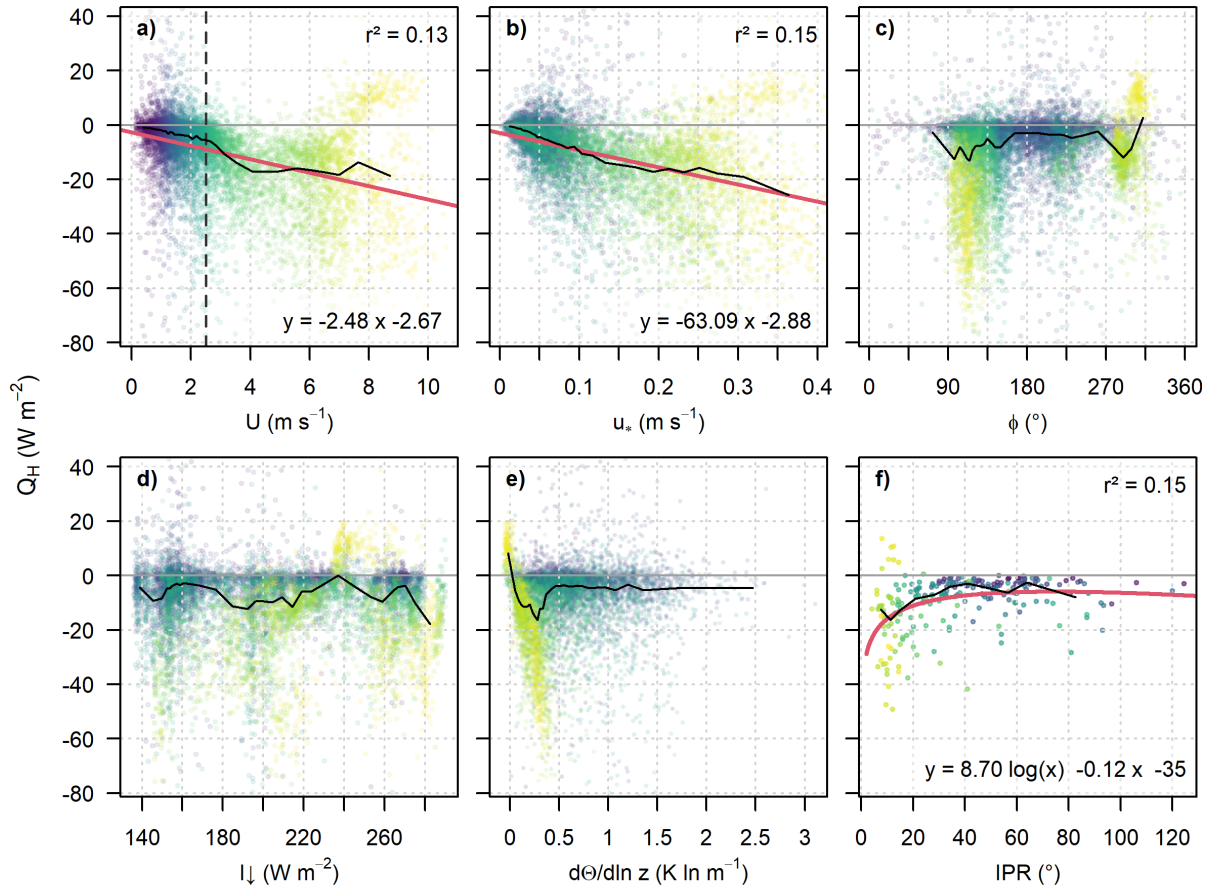


Figure 3.15.: Scatter plot of the sensible heat flux  $Q_H$  vs (a) wind velocity, (b) friction velocity, (c) wind direction, (d) longwave downwelling radiation, (e) static stability and (f) the meandering indicator interpercentile range (see Sect. 2.5.4). (a) to (e) are based on values aggregated to 2 min. (f) is based on the multi-resolution decomposition (MRD) windows with a length of 77 min (see Sect. 2.5.3), determining the temporal resolution for IPR. The y-axis is set so that the 0.25<sup>th</sup> to 99.75<sup>th</sup> percentile of the 2 min  $Q_H$  is shown, cutting off extreme outliers. Data points are colored by wind speed with (a) serving as reference. The black lines show bin averages with widths of 300 values for (a) to (e) and 20 for (f). The red lines show regression models, which are linear for (a) and (b) and logarithmic for (f), with the  $r^2$  and model formula printed in the plot. The vertical dashed line in (a) marks the wind speed threshold of  $2.5 \text{ m s}^{-1}$  (see Sect. 2.5.3).

- **IPR:** The meandering intensity was shown to decrease with increasing wind speed (see Sect. 3.2.3 and Fig. 3.15f). Since the magnitude of  $Q_H$  generally increased with  $U$ , this relation superimposed any potential impact that meandering itself might have had on the flux.

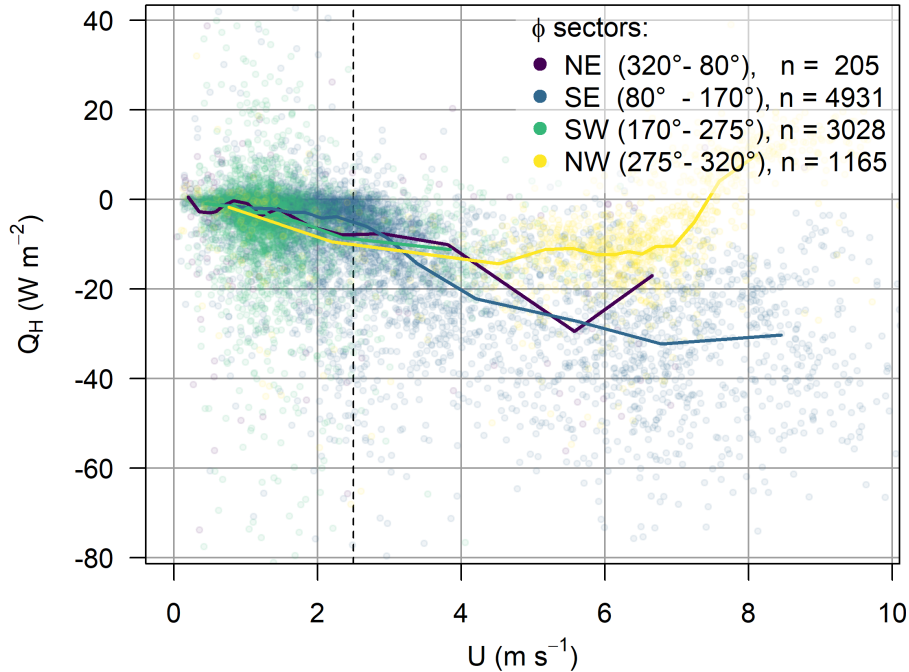


Figure 3.16.: Scatter plot of the buoyancy flux  $Q_H$  vs the wind velocity based on 2 min statistics. The points are colored by the wind direction regimes 1 to 4 according to table 2.1.  $n$  is the number of observations per class. The solid lines show bin averages with widths of 300 values for each direction category while the dashed line marks the wind speed threshold of  $2.5 \text{ m s}^{-1}$  derived in section 3.1.1. The plot area covers the mid 99.5% of  $Q_H$ .

The regimes allowed to isolate the effect of  $U$  on  $Q_H$  from the effect of the other regime parameters. Generally, regimes with weak winds went along with weaker fluxes and strong-wind regimes with strong downward  $Q_H$  while regimes with intermittent winds ranged in between (see Fig. 3.17a).

During strong winds wind direction was a secondary determinant of the flux: Strongest downward  $Q_H$  occurred during seaward flow from the SE-sector and weaker flux for winds from the ocean (NW-sector) or varying direction, agreeing with figure 3.16.

An interruption of the otherwise constantly statically stable conditions resulted in weaker fluxes in spite of strong winds (see Fig. 3.17a, regime # 8 and # 24). Hence, the weaker gradient in less stable conditions limited the flux, as indicated before.

The distributions of the  $I \downarrow$  and IPR categories appear disconnected from the magnitude of  $Q_H$ . However, when regimes are compared that have identical parameters in all other variables, it can be shown that both  $I \downarrow$  and IPR have an individual effect on  $Q_H$ :

- Otherwise identical regimes showed a lower magnitude of  $Q_H$  during higher  $I \downarrow$ . This behavior occurred for seven of the nine cases (see App. A.1).

- The opposite was shown for IPR. A higher meandering category coincided with higher magnitudes of  $Q_H$  in eight of the eleven comparable cases (see App. A.2).

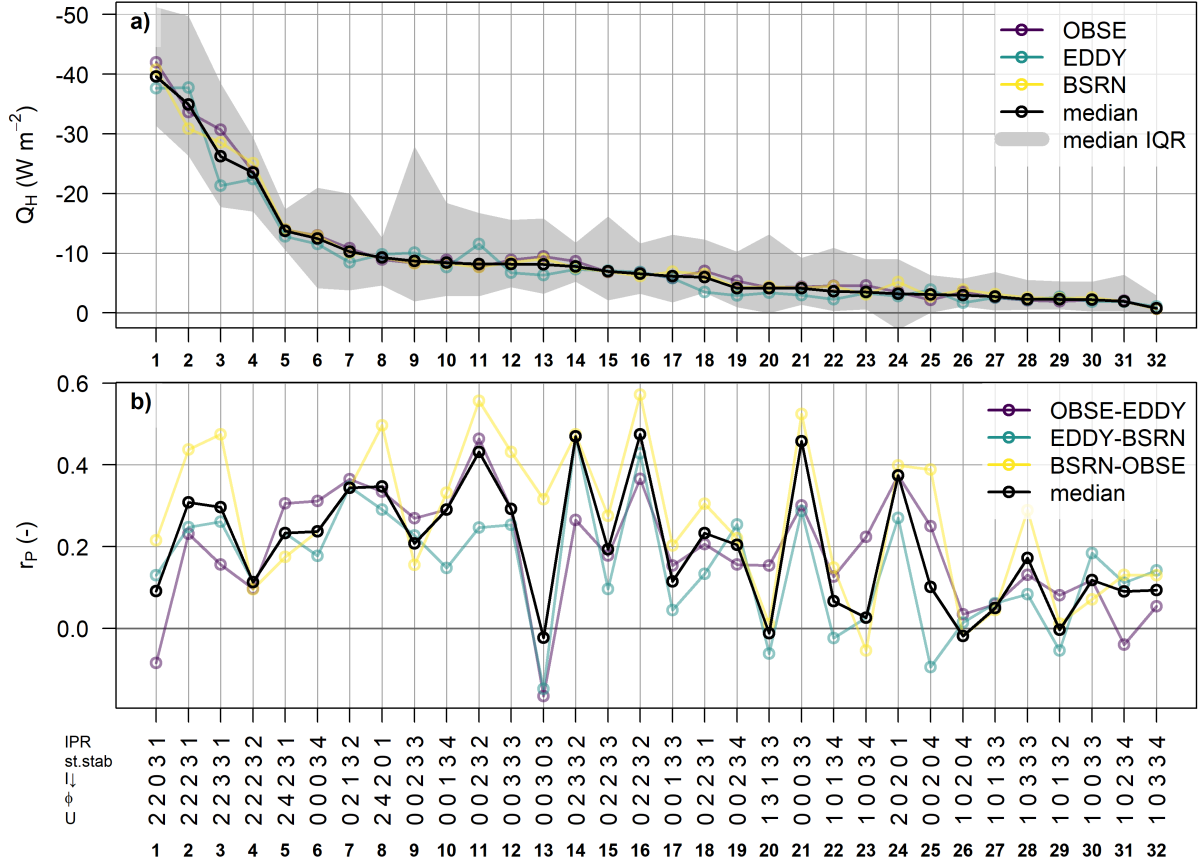


Figure 3.17.: For each of the 32 regimes (see Sect. 2.5.3) that occur at least twice during the measurement campaign: (a) The median sensible heat flux  $Q_H$  for the three ultrasonic anemometers (USAs) at the corners of the fiber-optic distributed sensing (FODS) array (colored points) as well as the median of all USAs (black points). The gray area marks the interquartile range (IQR) (the mid 50% of the data). (b) Pearson correlation coefficient  $r_p$  as median of the correlations of all windows within the respective regime, for each USA (colored points) as well as all data (black points). The regimes are ordered by median  $Q_H$ , the regime categories on the x-axis refer to table 2.1 with zero indicating that no single category occurred during at least 90% of the respective regime. The points are connected by lines for better lucidity, not indicating any conditions between the regimes.

The regimes varied not only in the magnitude but also spatial homogeneity of  $Q_H$  (see Fig. 3.17b). The median Pearson correlation  $r_p$  between the USAs ranged from  $-0.02$  to  $0.47$ . Generally, weak winds featured a lower correlation ( $r_p = -0.02$  to  $0.17$ ) than strong winds ( $r_p = 0.09$  to  $0.37$ ), suggesting motions on the submeso scale to impact the local flux during weak winds. To reduce the correlation between the USAs, these motions' spatial scales must be smaller or equal than the USAs' separation distance (140 m to 280 m) and differently distributed across the observational array. Intermittent winds, however, showed both the lowest and highest correlations ( $-0.02$  to  $0.47$ ), where the lowest coincide with non-stable stratification (regime # 13 and # 25), which seems to have favored spatial flux-heterogeneity. The high correlations might

have been introduced by large-scale wind speed fluctuations or drifts, resulting in simultaneous variation of  $Q_H$  at all USAs.

Concluding, wind speed proved to be the best single slow-response predictor for  $Q_H$ , as long as the vertical temperature gradient did not change sign, allowing prediction of the average flux magnitude. With fast-response observations available, however, the friction velocity  $u_*$  proved to be the better choice, since, in contrast to  $U$ , it was able to differentiate  $Q_H$  also within weak winds. By definition, both proxies failed to narrow down the  $Q_H$  when it was limited by the vertical temperature gradient rather than mixing, and to predict the direction of the flux. This is improved by direct gradient observations, which showed an about linear relation to  $Q_H$  for the strong-wind range where flux was limited by said gradient.

Isolating the impact of single, otherwise superimposed variables by comparing regimes showed that further differentiation of  $Q_H$  is improved considering meandering and  $I \downarrow$ : Meandering amplified  $Q_H$  while higher  $I \downarrow$  due to higher cloud cover generally reduced the magnitude of the flux.

However, the weaker flux during cloudy conditions was supposedly a result of a reduced radiative cooling of the surface and, hence, a reduction of the magnitude of the vertical temperature gradient. It, therefore, stands to question whether  $I \downarrow$  would further improve the predictability of  $Q_H$  when regimes would apply a finer categorization by the gradient.

Hypothesis H 1.5, that the magnitude of  $Q_H$  is primarily forced by wind speed, is confirmed considering the average behavior for the whole campaign period, represented by the bin averages in figure 3.15a. However, a large variability remains within the bins, where the flux is determined by a complex interplay of wind speed, incident flow temperatures (determining the gradient), the longwave-radiation regime and the occurrence of submeso-scale phenomena such as meandering.

### 3.3. Non-local drivers (RQ 2)

This RQ's hypotheses build on two kinds of non-local influence on the sensible heat flux  $Q_H$ :

- drivers of the flux that are not explained by local flux-gradient similarity and
- the impact of horizontal advection of sensible heat.

While the second can be directly analyzed based on the computed advection (see Sect. 2.5.1 and 3.1.2), the first is assumed to be the difference between  $Q_H$  measured by a USA and  $Q_H$  modeled using Monin-Obukhov similarity theory (MOST), which relies on solely local drivers (see Sect. 2.5.2).

The modeled  $Q_H$  using MOST reproduced the temporal pattern of the measured flux but underestimated part of the temporal variability during some of the weak-wind periods (see App. A.23). The relation between the measured and modeled flux shows a large scattering and the average relation is described by a linear model with a slope of 0.83 (Fig. 3.18). A distinct deviation from this model is the denser area in quadrant 1 (top right), which was mostly generated by the elucidated cold air front on 08.03.2020 (see Sect. 3.1.2 and App. A.23), where the model overestimated the upward flux intensity.

Since the modeled flux is based on the vertical FODS temperature gradient, a measured flux in

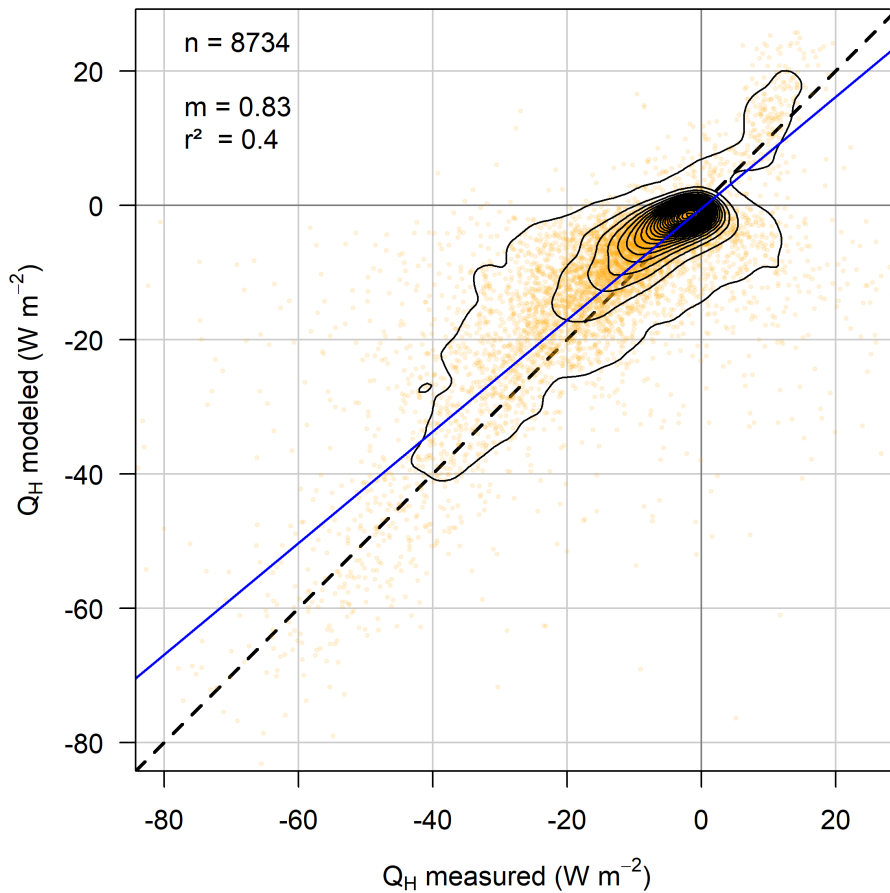


Figure 3.18.: Scatterplot of the sensible heat flux  $Q_H$  modeled with Monin-Obukhov similarity theory (MOST) and measured by the ultrasonic anemometer (USA) at the BSRN tower. The contour lines represent the density of points. The dashed line shows the 1:1 relationship, while the blue solid line depicts a least rectangles linear regression with the model parameters as well as the sample size printed top left. The temporal resolution is 2 min and the plot covers the whole campaign period from 26.02.2020 until 10.03.2020.

the opposite direction implies flux against the gradient and is expressed by points in quadrant 2 and 4 (top left and bottom right). Such so-called counter-gradient fluxes represent events of upward turbulent heat transport in spite of a statically stable stratification and were observed during 12% of the campaign period. Most of these cases occurred during positive measured  $Q_H$  as illustrated by the higher number of points in quadrant 4 than 2. The number of data points in quadrant 4 also exceeded those in quadrant 1 shows, showing that three fourths of all events of upward directed  $Q_H$  occurred in statically stable stratification.

The assumption that the sole reason for these discrepancies between measured and modeled  $Q_H$  are non-local impacts may, however, be violated as discussed in section 1.1. The following contributions are probable:

- The influence of strong non-local drivers, indicating a decoupling of the flux in the height of the USA (1.5 m a.g.l.) from the surface e.g. due to internal BLs (McNaughton and Laubach, 1998) in combination with horizontally heterogeneous fluxes.
- Incorrectly modeled flux due to scaling parameters of the universal functions that do not

represent the specific contribution of non-turbulent motions at the site (Acevedo et al., 2014).

- The differences in recording of the vertical temperature gradient and the actual heat flux: The gradient was computed as unweighted average over 2 min. While the actual heat flux was computed as 2 min-statistics as well, the sampling was done at 20 Hz and the heat change at each point in time was weighted with the instantaneous vertical motion. Hence, a short inversion of the gradient could have had an impact on the flux that was proportionally much larger than its duration if it coincided with a strong vertical motion. This might result in a lacking representation of intermittent motions such as coherent structures by the model.

These possible contributions are to keep in mind when analyzing the respective hypotheses.

### 3.3.1. Non-local influence and wind speed and direction (H 2.1)

#### 3.3.1.1. Monin-Obukhov similarity theory (MOST)

The median difference between measured and modeled sensible heat flux  $Q_H$  was almost zero in weak winds (Fig. 3.19). During strong winds, the model tended to underestimate the downward flux with the bin medians in figure 3.19 ranging from  $-1.7$  to  $-5.5 \text{ W m}^{-2}$ .

To evaluate the probability of strong non-local influences in different conditions, their proportion of large differences between measured and modeled  $Q_H$  was computed. Specifically, the proportions of absolute differences  $> 20 \text{ W m}^{-2}$  and  $> 50 \text{ W m}^{-2}$  were used as measures for large non-local impact (see Tab. 3.1). Large discrepancies between the modeled and measured flux were more frequent in weak than strong winds. Absolute differences above  $20 \text{ W m}^{-2}$  were proportionally 1.6 times more frequent during weak than strong winds (see Tab. 3.1), absolute differences above  $50 \text{ W m}^{-2}$  even 3.5 times more frequent. Hence, the probability for extreme differences and presumably non-local effects increased with decreasing wind speed.

Table 3.1.: Proportion of large differences between measured and modeled sensible heat flux  $Q_H$  during weak winds ( $U \leq 2.5 \text{ m s}^{-1}$ ) and strong winds ( $U > 2.5 \text{ m s}^{-1}$ ) as well as by wind direction sectors during weak winds. The direction sectors are defined according to table 2.1. The first column states the threshold of the absolute difference.

$ Q_{H,measured} - Q_{H,modeled} $	% of all weak winds	% of all strong winds	% of all weak winds from			
			NE	SE	SW	NW
$> 20 \text{ W m}^{-2}$	6.3	3.9	9.4	1.9	9.0	10.1
$> 50 \text{ W m}^{-2}$	1.4	0.4	3.4	0.3	1.9	3.1

The described coherence between non-local influence and wind speed varied between the wind direction sectors (see Fig. 3.20). The following evaluation focuses on the differences during weak winds, where non-local impact was more frequent, as outlined above.

Weak winds occurred frequently both from the SE-sector along the fjord and the SW-sector

down the adjacent slopes (see Fig. 3.20). The proportion of large absolute differences between the measured and modeled  $Q_H$ , however, was much higher during winds from the SW-sector: Absolute differences  $>20 \text{ W m}^{-2}$  were proportionally 4.7 times more frequent (see Tab. 3.1), absolute differences  $>50 \text{ W m}^{-2}$  even 6.3 times.

The NE- and NW-sector showed even higher proportions than the SW-sector (see Tab. 3.1).

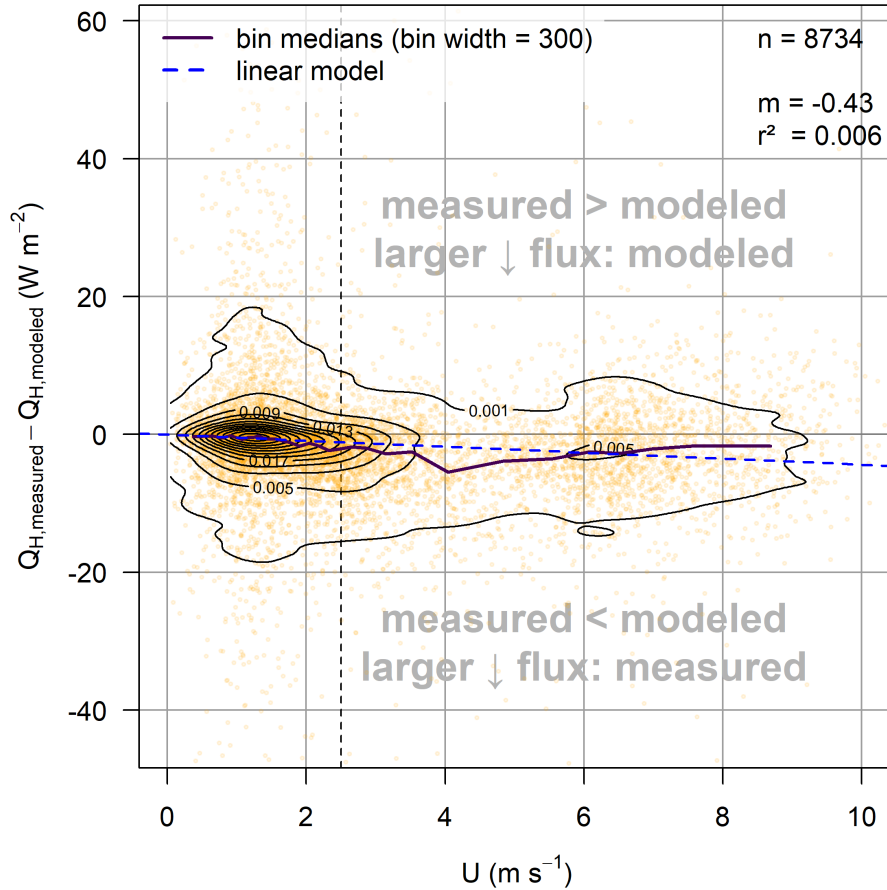


Figure 3.19.: Scatterplot of the difference between measured and modeled sensible heat flux  $Q_H$  (see Fig. 3.18) over wind speed  $U$ . The contour lines show the density of points, the violet solid line connects bin medians with a bin-width of 300. A linear model is represented by the dashed blue line with the model parameters as well as sample size printed top right.

These sectors, however, featured no weak wind regime. The rare weak winds from these directions can, hence, be expected to originate from circulating winds and tell little about the properties of the respective sectors.

These results point towards a higher proportion of non-local influences during katabatic flows compared to equally weak flows traveling along the fjord. This might be explained by shallow currents of cold air running down the adjacent slopes in the SW-sector, causing a strong surface based inversion and vertical decoupling of the flux. While the weak flows from the SE-sector are assumed to be of katabatic origin as well, their long travel along the fjord allowed the cold-air current to mix upward and dissolve the sharp boundary between air layers. It is, however, difficult to distinguish, whether and to what degree the observed effect is affected by incorrectly modeled non-turbulent or intermittent motions. Nevertheless, these results prompt the source

area as a determinant of non-local influence in addition to the strong influence of wind speed.

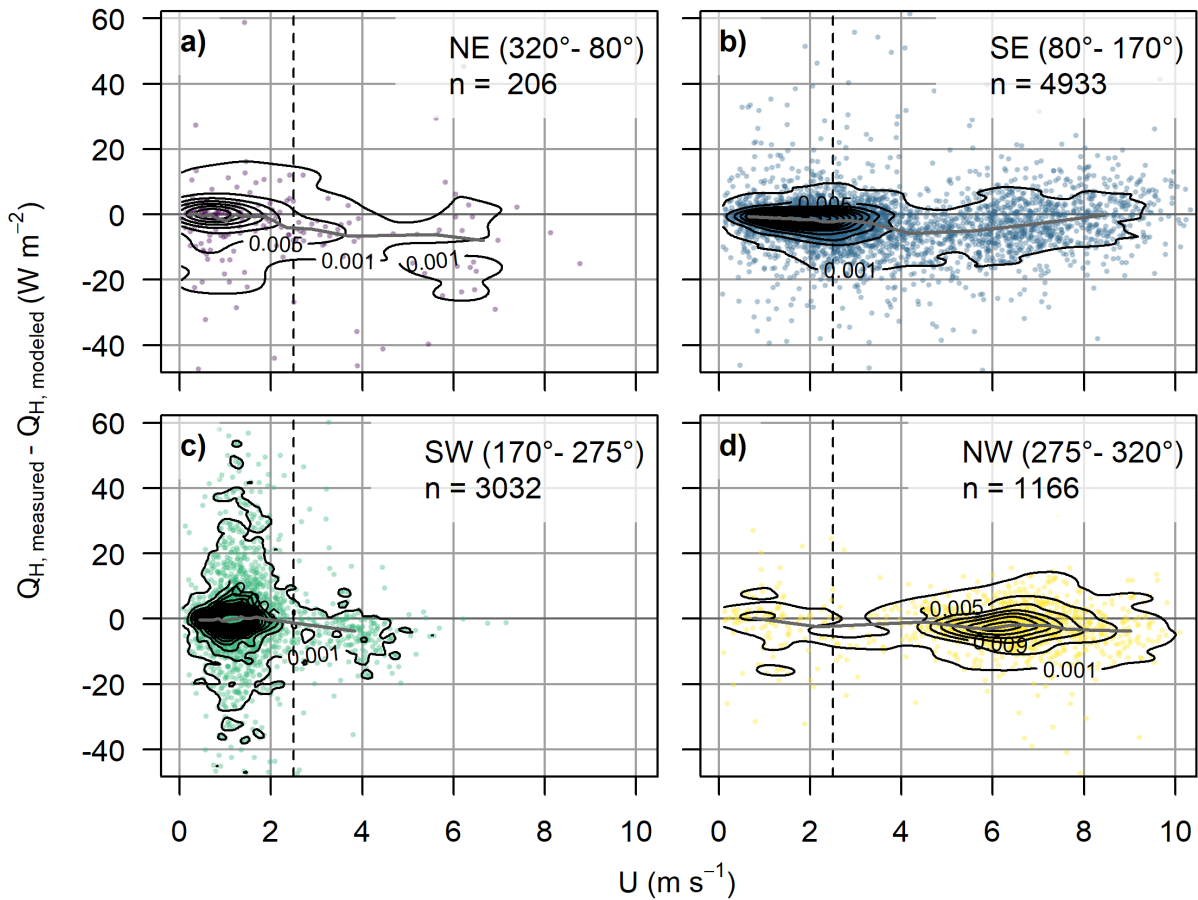


Figure 3.20.: Scatterplots as in figure 3.19 for different wind direction sectors (see Tab. 2.1). The grey solid lines are bin medians with the bin width being the sample size  $n$  divided by 15.

The generally higher proportion of non-local influences on  $Q_H$  during weak compared to strong winds confirms the first part of hypothesis H 2.1. The assumption that the frequency of large non-local impacts for a wind direction sector scales solely with its amount of weak-wind cases, however, was disproved, attesting an influence of the source area of the incident flow. Of the two direction sectors with frequent weak winds, the sector with air coming down the mountains showed an overproportional amount of non-local impacts compared to flow along the fjord.

### 3.3.1.2. Horizontal advection

Like large differences between the measured and modeled  $Q_H$  (see above), large magnitudes of horizontal advection  $Q_A$  also were more frequent in weak than strong winds: during weak winds the magnitude of  $Q_A$  was proportionally twice as often  $> 20 \text{ W m}^{-2}$  compared to strong winds (see Tab. 3.2). The discrepancy was even larger for extreme magnitudes  $> 50 \text{ W m}^{-2}$ , which were proportionally seven times more frequent in weak than strong winds.

As discussed in section 3.1.2 those large magnitudes were predominantly associated with south-westerly flows (see App. A.7 and Fig. 3.21). This is also reflected in the proportions of large

magnitudes of  $Q_A$  during weak winds (see Tab. 3.2): The SW-sector (katabatic winds from Zeppelin mountain and Brøgger glacier) featured by far the highest proportions of absolute  $Q_A$  above both  $20$   $50$   $W m^{-2}$ . Hence, winds from the mountains, again, introduced the largest non-local effects.

This finding, that impacts of advection were stronger during weak flows down the mountain slopes than strong flows along the fjord, emphasizes strong vertical temperature gradients as dominant driver over strong flow.

More than two thirds of the advective fluxes from the SW-sector, that had magnitudes above  $20$   $W m^{-2}$ , were positive, which means an advective heat loss at the site (not shown). A predominant heat loss in the presence of katabatic flows can be expected. The still frequent events of heat gain, however, either suggest an intermittent nature of the cold-air drainage where the density current occasionally tears off or a meandering of the current.

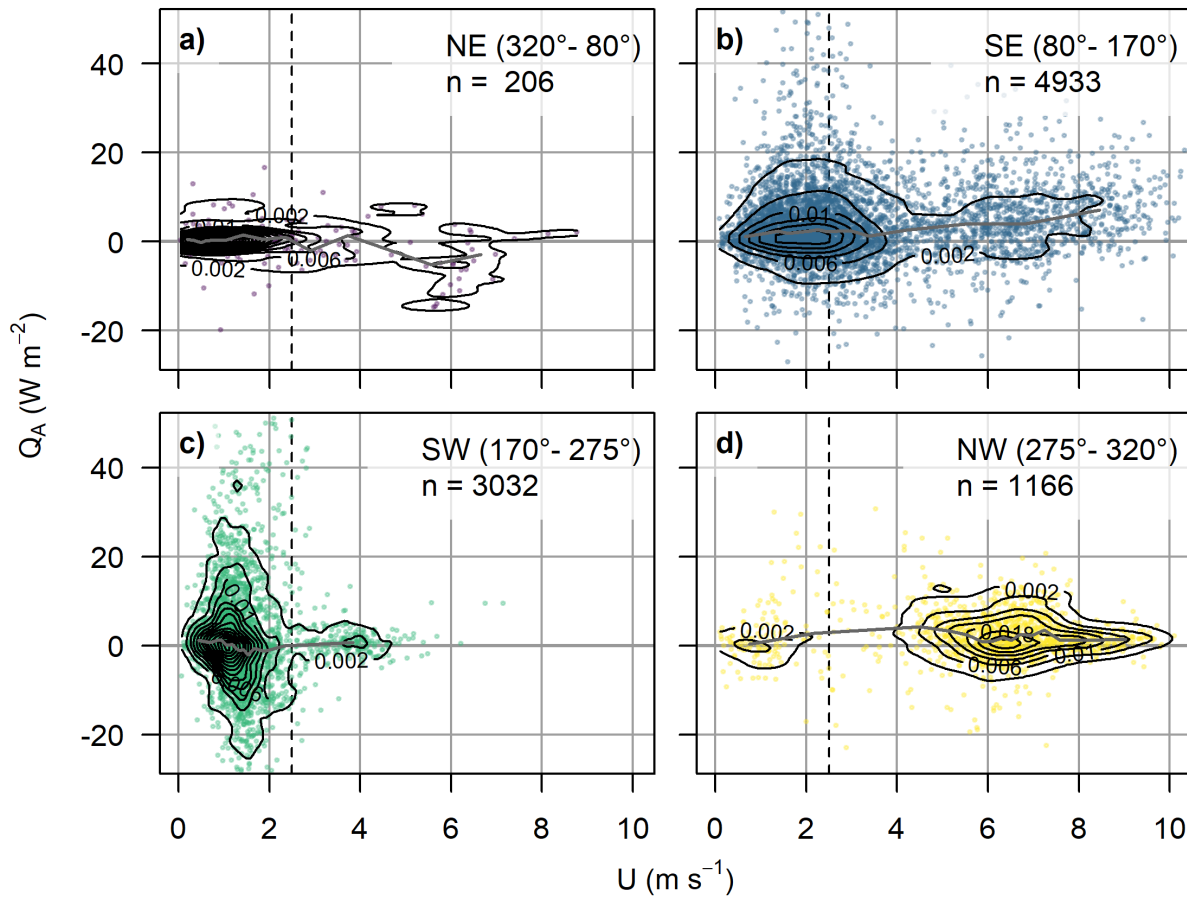


Figure 3.21.: Horizontal advection of sensible heat ( $Q_A$ , see Eq. 2.4) against wind velocity, recorded by the ultrasonic anemometer (USA) at the EDDY tower. Subfigures depict the four wind direction categories (see Tab. 2.1). The dashed vertical line marks the wind speed threshold of  $2.5$   $m s^{-1}$ . The grey solid lines are bin medians with the bin width being the sample size  $n$  divided by 15.

As for 3.3.1.1, the first assumption of hypothesis H 2.1 is confirmed: The impact of non-local influence by advection was increased during low wind speeds and sectors with frequent weak winds also showed more events of non-local influence due to advection. Conditions promoting

Table 3.2.: Proportion of large absolute horizontal advection of sensible heat  $|Q_A|$  during weak winds ( $U \leq 2.5 \text{ m s}^{-1}$ ) and strong winds ( $U > 2.5 \text{ m s}^{-1}$ ) as well as by wind direction sectors during weak winds. The direction sectors are defined according to table 2.1. The first column states the threshold of the absolute difference.

$ Q_A $	% of all	% of all	% of all weak winds from			
	weak winds	strong winds	NE	SE	SW	NW
$> 20 \text{ W m}^{-2}$	7.1	3.5	0.0	5.0	9.5	3.9
$> 50 \text{ W m}^{-2}$	0.7	0.1	0.0	0.4	1.2	0.0

the impact of non-turbulent motions and strong small-scale spatial gradients, hence, seem to favor advection of heat at least in a heterogeneous environment.

The proportions of strong advective impacts, however, varied between sectors even within solely weak winds. Hence, wind speed was not the only determinant of the difference in the magnitude of  $Q_A$  between the direction sectors. The local history, i.e. the source area and properties of the incident flow appear to strongly influence advection as well.

### 3.3.2. Non-local influence and cloud cover (H 2.2)

As shown above, wind speed was a major determinant of non-local influence. To evaluate the possible additional impact of longwave downwelling radiation  $I \downarrow$  as a combined proxy for cloud cover and cloud temperature, its effect on the relation between non-local impact and wind speed is investigated. This, again, is done for non-local influences expressed by the absolute difference between  $Q_H$  measured and modeled according to MOST as well as by horizontal advection of sensible heat.

The relation between  $U$  and the difference between measured and modeled  $Q_H$  scaled with the magnitude of  $I \downarrow$  (Fig. 3.22) where large non-local impacts were more probable during less cloudy intervals than during overcast conditions. The proportions of larger non-local influences were very similar between weak and medium  $I \downarrow$  (category 1 and 2) and differed from strong  $I \downarrow$  (category 3) even though the respective wind speeds rather grouped medium and strong  $I \downarrow$  (category 2 and 3) in contrast to weak  $I \downarrow$  (category 1, see Fig. 3.22).

Hence, in accordance with hypothesis H 2.2, few or cold clouds went along with more frequent, strong non-local influences, while clouds that re-emit larger quantities of longwave radiation tended to diminish these influences. Since re-emittance is omnidirectional it provides a spatially consistent radiative warming that supposedly homogenizes spatial differences in e.g. surface temperature arising from different surface properties or turbulence characteristics as also found in section 3.2.2. However,  $I \downarrow$  had to reach a threshold value of around  $-245 \text{ W m}^{-2}$  to develop said effect.

An equal behavior of weak and medium in contrast to strong  $I \downarrow$  deviates from the findings in section 3.2.2, where medium and strong  $I \downarrow$  showed similar characteristics in distinction to weak  $I \downarrow$ . The discussed threshold value of  $I \downarrow$  to impact the power of submeso-scale motions differs, hence, from the threshold determining non-local influence.

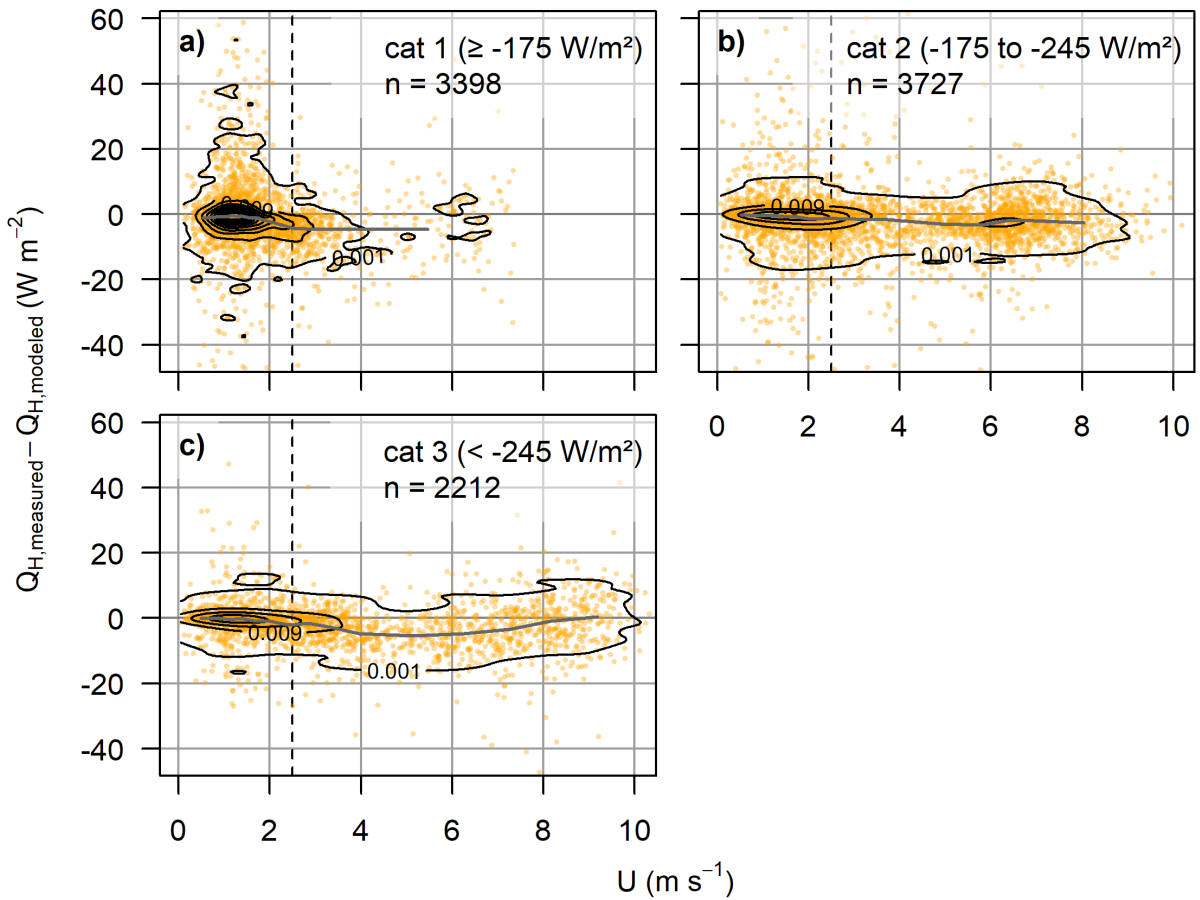


Figure 3.22.: Scatterplot of the difference between measured and modeled sensible heat flux  $Q_H$  (see Fig. 3.18) against wind speed  $U$ , measured by the ultrasonic anemometer (USA) at the EDDY tower. The subfigures a) to c) are subsets for the three regime categories for longwave downwelling radiation  $I \downarrow$ , explained in table 2.1 with the  $I \downarrow$ -range plotted top right. The contour lines show the density of points,  $n$  is the sample size of the respective subset.

The overall pattern connecting the deviation of modeled and measured  $Q_H$  to  $I \downarrow$  was reproduced by the coherence between horizontal advection of sensible heat  $Q_A$  and  $I \downarrow$  (see Fig. 3.23): The proportion of large advective transport scaled inversely with the magnitude of  $I \downarrow$ , clear skies, hence, favored large magnitudes of  $Q_A$ .

Hypothesis H 2.2, thus, appears valid also for non-local effects in terms of horizontal advection.

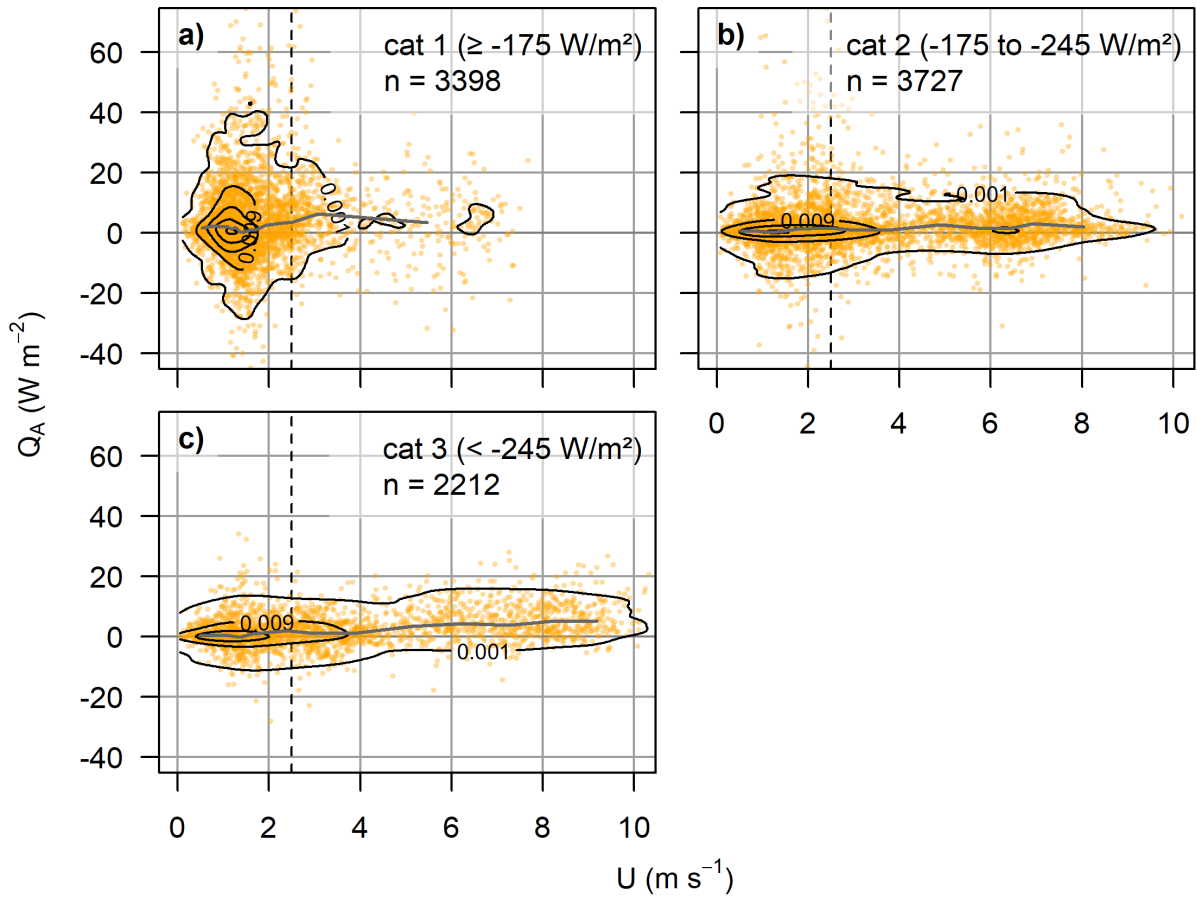


Figure 3.23.: Scatterplot of the horizontal advection of sensible heat  $Q_A$  according to section 2.5.1 against wind speed  $U$ , measured by the ultrasonic anemometer (USA) at the EDDY tower. The subfigures a) to c) are subsets for the three regime categories for longwave downwelling radiation  $I \downarrow$ , explained in table 2.1 with the  $I \downarrow$ -range plotted top right. The contour lines show the density of points,  $n$  is the sample size of the respective subset.

### 3.4. Case study: soliton

A temporally and spatially distinct submeso-scale phenomenon was discovered in the readings of the fiber-optic array for the 05.03.2020. The motion occurred as a solitary mode that moved in south-westerly direction against the wind, observed as cold temperature perturbation sensed by the horizontal fiber array at approximately 1 m a.g.l. (see Fig. 3.24b). The cold section moved along the transect between the EDDY and BSRN tower towards the first and was visible also in the transect between the OBSE and EDDY tower (see App. A.25). When the motion reached the EDDY tower, the high resolution vertical profile detected an upward mixing of cold air directly above the surface, reaching up to the height of the horizontal fiber (see Fig. 3.24d). At this point around 16:46 the wind speed picked up (see Fig. 3.24a) and the feature halted and reversed its path, dissolving on its way. The location of the solitary wave caused an abrupt change in wind speed and/or direction (see Fig. 3.24c and App. A.25). The wind component orthogonal to the horizontal fiber was very weak in front of the motion but enhanced at the location of the temperature perturbation.

The combined observations suggest a submeso-scale feature with horizontal extent of some decameters that advanced against the weak mean wind and disturbed the strong stratification by mixing the air within the lowermost 1.5 m above ground. An increase in wind speed from around  $1 \text{ m s}^{-1}$  to  $1.5 \text{ m s}^{-1}$  was sufficient to erase the feature.

When the motion reached the EDDY tower, the downward sensible heat flux increased from around  $0 \text{ W m}^{-2}$  to  $-20 \text{ W m}^{-2}$  (see Fig. 3.25). While such (and stronger) increases in  $Q_H$  occurred several times in the displayed period, the mentioned event was the only one not directly associated with a major increase in horizontal wind speed. The motion barely reached the EDDY tower where  $Q_H$  was observed and did not pass the station, suggesting, that the flux perturbation was even stronger in the center of this solitary mode.

This case study demonstrates how submeso-scale motions that are unrelated to the mean wind affect the near-surface exchange processes in a way that is missed when solely investigating shear-generated turbulence.

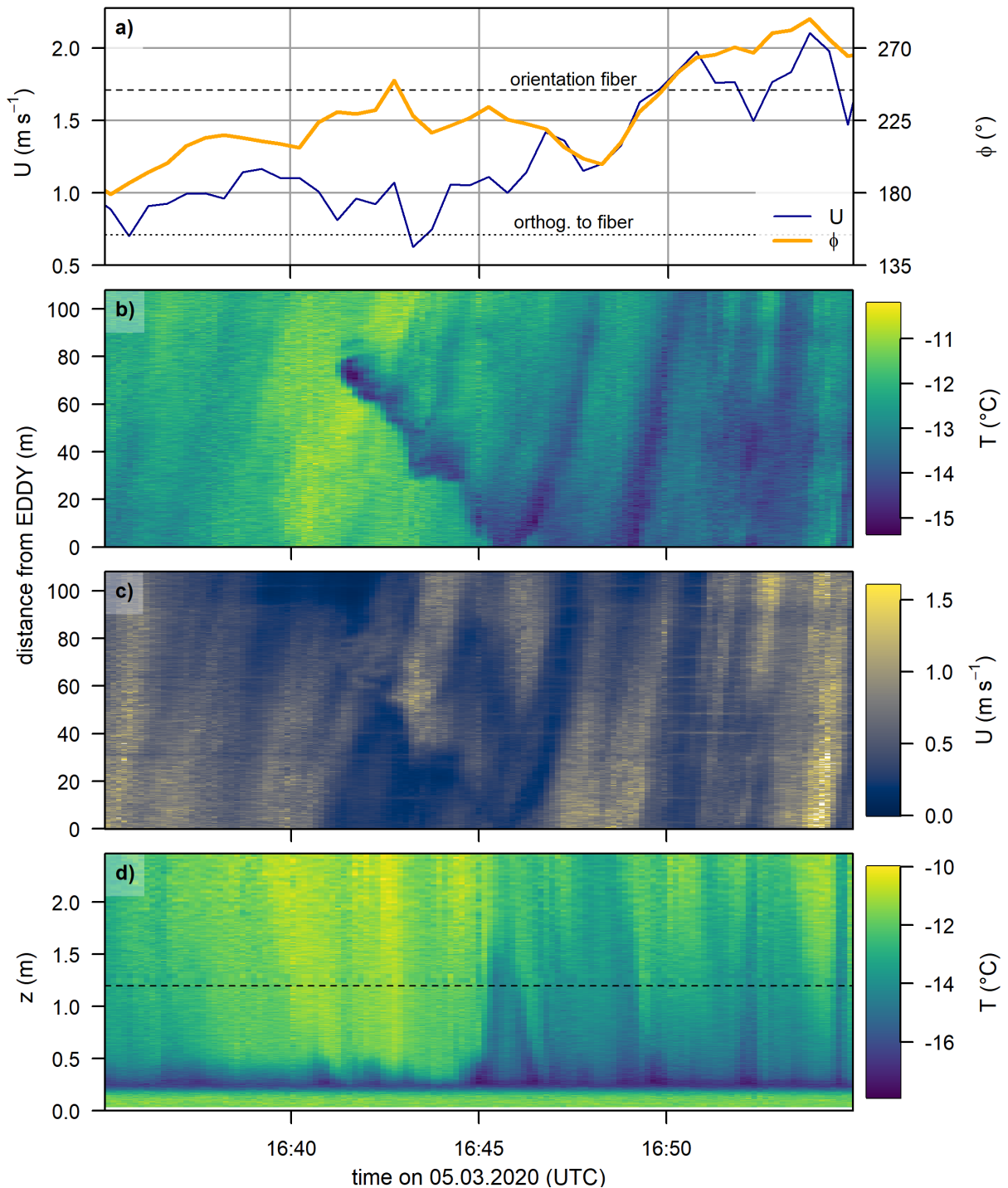


Figure 3.24.: Observations of the fiber-optic distributed sensing (FODS) and ultrasonic anemometer (USA) setup on 05.03.2020 from 16:40 to 16:55. (a) shows wind speed  $U$  and direction  $\varphi$  recorded by the USA at the EDDY tower with a temporal resolution of 30s. The dashed line marks the orientation of the horizontal fiber in (b) and (c) ( $244^\circ$ ) while the dotted line is the direction orthogonal to said fiber ( $154^\circ$ ). (b) and (c) display the first 108 m of horizontal fiber from the EDDY tower towards the BSRN tower where (b) shows temperatures and (c) the wind component orthogonal to the fiber. The horizontal stripes in (c) are artifacts of fiber holders and strips of streamer, added for safety reasons in the field. The three most protruding artifacts were already removed by linear spatial interpolation. (d) displays a temperature profile next to the EDDY tower, measured with a high resolution fiber optic column. The lowest 0.23 m with temporally homogeneous and relatively warm temperatures were within snow. The dashed horizontal line marks the approximate height at which the horizontal fibers in (b) and (c) are mounted.

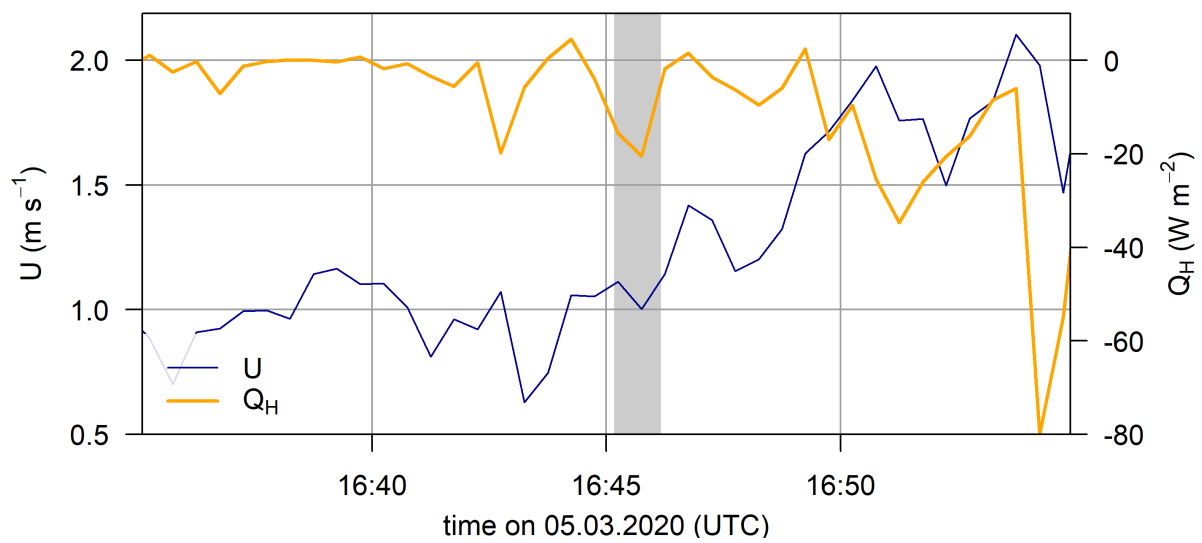


Figure 3.25.: Time series of wind speed  $U$  (blue line) and sensible heat flux  $Q_H$  (orange line) for the 05.03.2020 from 16:40 to 16:55. The period corresponds to figure 3.24. Observations are made by ultrasonic anemometer (USA) at the EDDY tower with a perturbation time scale of 30 s. The grey bar marks the time where the solitary motion displayed in figure 3.24 reaches the EDDY tower.

## 4. Conclusions

The main objective of this thesis was to improve our understanding of the atmospheric processes in the weak-wind Arctic BL with special focus on their drivers, perspective allowing for better parametrization of Arctic SBLs. An additional main objective of the NYTEFOX project was to test the feasibility of a setup that allows to resolve the relevant SBL processes. Therefore, a large multi-system setup was deployed in Ny-Ålesund in a location likewise influenced by a fjord, steep mountain slopes and glacier outflows. A novelty was the installation of a horizontal FODS deployment of several hundreds of meters in an Arctic environment, allowing for temporally and spatially continuous observation of air temperature and wind speed. The setup was completed by USAs for observation of turbulent quantities and a SODAR for a larger-scale context, while measurements of radiation and soil heat flux were taken by the AWIPEV.

The surface energy balance could not be closed despite including direction estimates of horizontal advection computed directly from fiber optic observations. The remaining residual suggests one or a combination of the following scenarios:

- The gap is caused by the still unresolved quantities, which are mostly flux divergence and energy storage in the air as well as the soil layer above the measurement of  $Q_G$ .
- The gap is caused by wrong observation or computation of a quantity.
- The mismatch results from the different footprints the included systems are observing, which are separated by up to 300 m.

To what extent which of those points applies can not be finally ensured although some impact of the last is likely due to the spatially highly heterogeneous environment. A future campaign might benefit from a greater proximity of the systems required for the surface energy balance. The thesis confirmed former observations of a channeling effect of the local topography, forcing strong synoptic winds along the fjord axis. In contrast, calm periods featured varying wind directions as well as frequent katabatic flows towards the fjord. These flows appeared to join currents that drain the fjord valley towards the ocean in the NW. However, many periods were characterized by alternating weak and strong winds of mostly varying direction whose origin might be further investigated in future analyses.

Cloud cover was found to largely determine the power in submeso-scale motions. The re-emitted radiation from clouds spatially homogenized temperatures and wind speeds, dampening processes that are not solely relying on the bulk shear. The effect was most sensitive in the range of low magnitudes of  $I \downarrow$ . Hence, a moderate clouding appears to already notably reduce the power in submeso-scale motions while further increase to overcast conditions adds little impact. Contrary to the expectations, calming of the winds did not generally favor the power in submeso-scale processes on all but the longest time scales. This braces the initially mentioned assumption that processes on the submeso scale are sustained even under convective conditions. Calm conditions, however, raised the importance of submeso-scale phenomena since, in

contrast to micro-turbulence, their power generally did not decline with wind speed.

Meandering as a specific submeso-scale phenomenon, however, required periods of, optionally interrupted, calm conditions. The coexistence of two flows with locally alternating dominance appeared to be a further requirement for meandering in the observed environment. This might be a synoptic and a local, submeso-scale flow or two submeso-scale currents. The area experiencing meandering, hence, appears to be limited to the area where these currents interact.

The observed directional shifts had magnitudes of around  $100^\circ$  to  $200^\circ$  and time scales of about 30 min.

A future setup with continuous observations of wind direction from a mountain foot all the way to the fjord would allow to test the derived explanation of the local generation of meandering. These data could reveal the spatial extent affected by the meandering directions and whether it is indeed generated by the oscillating interface of two competing currents.

Variability on the submeso-scale was not only introduced by large-scale topography but also small-scale surface heterogeneity. While, as expected, local orography impacted both the persistent patterns as well as dynamics of temperature and wind speed, also heterogeneous snow cover showed an effect. The varying cover and thickness of the snow appeared to radiatively affect the air temperature above, resulting in vertical and horizontal gradients. Events of snowfall and thawing are, hence, likely to have a lasting effect on small-scale dynamics in the weak-wind SBL.

Proceeding from a detection of individual drivers to a quantification of their cumulative implication on fluxes, wind speed proved to be an important proxy. It could, however, only predict the median behavior of a turbulent flux, averaged over multiple weeks, and failed to predict the flux magnitude in wind speeds above about  $4 \text{ m s}^{-1}$  where it was limited by the gradient rather than by mixing. Hence, gradient observations are vital in strong winds. Wind speed also could not predict the flux in weak winds where the mean wind was not the main determinant of turbulence. In this range, the flux was driven by a complex interplay of several parameters: Cloud cover was found to limit the flux while it was enhanced by the meandering intensity which could probably be shown for other submeso-scale phenomena as well.

Defining regimes by wind speed and the vertical gradient, hence, allows a coarse classification of exchange processes, while within especially the weak-wind classes a subdivision by radiation parameters and motion detection allows for a more precise prediction of fluxes. Research question 1 can therefore be affirmed: BL regimes do allow predictions about the characteristics of flux and turbulence across the static stability and wind speed ranges.

With the parameters and classes applied in this thesis, the predictions still contain some uncertainty, however, which might be further reduced by inclusion of other parameters and adjustment of some of the regime categories. A truly quantitative flux prediction would e.g. require finer regime classes for the temperature gradient which so far only distinguished between statically unstable, neutral and stable stratification. Quantification of non-turbulent processes other than meandering would better account for turbulence not generated by the bulk shear. It was shown that this could also be achieved by replacing wind speed as a regime parameter with a direct measure of the mixing intensity, such as the friction velocity.

Within weak winds, however, the strong spatial variability of processes limits the spatial repre-

---

sentativeness of the predictions. Further analyses could therefore investigate if the variance on submeso scales along the optical fiber, which integrates over these variabilities, allows spatially representative weak-wind flux predictions.

Also research question 2 can be approved: We did observe periods where local flux-gradient similarity was violated, including instances with flux opposing the local temperature gradient. Turbulence, hence, appeared to sometimes have a memory of the non-local source area of the mean advected flow.

The respective proportions were higher during weak than strong winds. In weak winds, the probability for large non-local influences was further increased during katabatic flows from the adjacent slopes compared to winds along the fjord.

Also cloud cover showed impact on non-locally determined fluxes with overcast skies reducing their probability. Longwave radiation from clouds, though, had to reach a threshold of around  $-245 \text{ W m}^{-2}$  to show notable effect.

However, it could not be ascertained whether the observed effects were truly due to a decoupling of the flux from the local surface. Possible additional drivers are the site-specific nature of non-turbulent processes as well as the difference in the sampling frequency of the gradient and the actual reference heat flux. An impact of the latter would suggest that short-lived intermittent motions have a significant impact on the exchange processes.

The conditions favoring a deviation from local similarity were the same that showed strongest horizontal advection, including the directional dependence. The response to thermal radiation from clouds, however, was more gradual, not displaying the discussed threshold behavior.

This work could confirm the highly non-linear and non-stationary nature of BL processes under the very stable conditions of polar night and prove FODS as an appropriate technique to investigate these processes both with case studies and bulk analyses. A broad overview over several site-specific as well as general drivers of non-turbulent processes was achieved and put into relation, leading the way into further and more specialized analyses as well as new field deployments. These could test the transferability of the gained insights and extend the observational basis.



# Acknowledgements

The NYTEFOX campaign was a large cooperative effort and I am thankful to all the people supporting my work and making this thesis possible.

First of all I would like to thank my main supervisor Christoph Thomas for asking me to take part in this fascinating project and guiding me along the way. Since I have a special affection towards the northern realms I am grateful I could travel to Svalbard and ever so slightly contribute to a better understanding of Arctic conditions.

The successful conduction of the campaign was made possible by the great work of the whole NYTEFOX team: Thank you Marie Zeller, Lena Pfister, Daniela Littmann and the PI's Alexander Schulz and Christoph Thomas for the collaboration and memorable time spent together in the ice and snow! Special thanks go to Alexander Schulz for providing and processing supplementary data. An essential part of the processing and organization of the data was done in cooperation with Marie Zeller. I am thankful for the extensive collaboration, for suggestions, feedback and friendship.

Thanks also goes to the team of the AWIPEV station for their great support in the field and for caring for our safety as well as to the group of the ISLAS project from the University of Bergen and to Irene Suomi for helping with the deployment.

I am grateful for the support of the Micrometeorology group of Bayreuth for helping me with all the questions that came up along my thesis and for the constructive feedback. I especially thank Wolfgang Babel for evaluating this thesis and Johann Schneider for supporting the packing and preparation of all the equipment that we thought of as well as for sending after what we did not think of. Great thanks goes to Karl Lapo who introduced me to the handling of fiber-optic data and guided me through countless iterations and troubleshootings, resulting in a meaningful data set. I thank Tobias Linhardt for providing and explaining his translation of software code and Ruth Adamczewski for proofreading stages of the thesis.

Lastly, I want to thank Judith Eisenbacher for her help and feedback, for discussions and proofreading and for bearing with me also during the harder times of the process.



# Bibliography

- Acevedo, O. C., Moraes, O. L. L., Fitzjarrald, D. R., Sakai, R. K., and Mahrt, L.: Turbulent carbon exchange in very stable conditions, *Boundary-Layer Meteorology*, 125, 49–61, doi:10.1007/s10546-007-9193-6, 2007.
- Acevedo, O. C., Costa, F. D., Oliveira, P. E. S., Puhales, F. S., Degrazia, G. A., and Roberti, D. R.: The Influence of Submeso Processes on Stable Boundary Layer Similarity Relationships, *Journal of the Atmospheric Sciences*, 71, 207–225, doi:10.1175/JAS-D-13-0131.1, 2014.
- Anfossi, D., Oetl, D., Degrazia, G., and Goulart, A.: An Analysis Of Sonic Anemometer Observations In Low Wind Speed Conditions, *Boundary-Layer Meteorology*, 114, 179–203, doi:10.1007/s10546-004-1984-4, 2005.
- Anquetin, S., Guilbaud, C., and Chollet, J.-P.: The Formation and Destruction of Inversion Layers within a Deep Valley, *Journal of Applied Meteorology*, 37, 1547–1560, doi:10.1175/1520-0450(1998)037<1547:TFADOI>2.0.CO;2, 1998.
- Arya, S. P.: Introduction to micrometeorology, This is volume 79 in the International geophysics series, Academic Press, San Diego, 2nd ed. edn., 2001.
- Beine, H. J., Argentini, S., Maurizi, A., Viola, A., and Mastrantonio, G.: The local wind field at Ny-lesund and the Zeppelin mountain at Svalbard, *Meteorology and Atmospheric Physics*, 78, 107–113, doi:10.1007/s007030170009, 2001.
- Belušić, D. and Mahrt, L.: Estimation of length scales from mesoscale networks, *Tellus A*, 60, 706–715, doi:10.1111/j.1600-0870.2008.00328.x, 2008.
- Boike, J., Juszak, I., Lange, S., Chadburn, S., Burke, E. J., Overduin, P. P., Roth, K., Ippisch, O., Bornemann, N., Stern, L., Gouttevin, I., Hauber, E., and Westermann, S.: HRSC-AX data products (DEM and multi channel) from aerial overflights in 2008 over Bayelva (Brøggerhalvøya peninsula, Spitsbergen), doi:10.1594/PANGAEA.884730, 2018.
- Breili, K., Hougen, R., Lysaker, D. I., Omang, O. C. D., and Tangen, B.: Research Article. A new gravity laboratory in Ny-Ålesund, Svalbard, *Journal of Geodetic Science*, 7, doi:10.1515/jogs-2017-0003, 2017.
- Businger, J. A., Wyngaard, J. C., Izumi, Y., and Bradley, E. F.: Flux-Profile Relationships in the Atmospheric Surface Layer, *Journal of the Atmospheric Sciences*, 28, 181–189, doi:10.1175/1520-0469(1971)028<181:FPRITA>3E2.0.CO;2, 1971.
- Cengel, Y. and Ghajar, A.: Heat and Mass Transfer: Fundamentals and Applications, McGraw-Hill Education, New York, USA, 4 edn., 2014.
- Cohen, J., Screen, J. A., Furtado, J. C., Barlow, M., Whittleston, D., Coumou, D., Francis, J., Dethloff, K., Entekhabi, D., Overland, J., and Jones, J.: Recent Arctic amplification and extreme mid-latitude weather, *Nature Geoscience*, 7, 627–637, doi:10.1038/ngeo2234, 2014.

- Curry, J. A., Schramm, J. L., and Ebert, E. E.: Sea Ice-Albedo Climate Feedback Mechanism, *Journal of Climate*, 8, 240–247, doi:10.1175/1520-0442(1995)008<0240:SIACFM>2.0.CO;2, 1995.
- Davy, R. and Esau, I.: Global climate models' bias in surface temperature trends and variability, *Environmental Research Letters*, 9, 114024, doi:10.1088/1748-9326/9/11/114024, 2014.
- Des Tombe, B., Schilperoort, B., and Bakker, M.: Estimation of Temperature and Associated Uncertainty from Fiber-Optic Raman-Spectrum Distributed Temperature Sensing, *Sensors (Basel, Switzerland)*, 20, doi:10.3390/s20082235, 2020.
- Esau, I. and Repina, I.: Wind Climate in Kongsfjorden, Svalbard, and Attribution of Leading Wind Driving Mechanisms through Turbulence-Resolving Simulations, *Advances in Meteorology*, 2012, 1–16, doi:10.1155/2012/568454, 2012.
- Etling, D.: On plume meandering under stable stratification, *Atmospheric Environment. Part A. General Topics*, 24, 1979–1985, doi:10.1016/0960-1686(90)90232-C, 1990.
- Foken, T.: The energy balance closure problem: an overview, *Ecological applications : a publication of the Ecological Society of America*, 18, 1351–1367, doi:10.1890/06-0922.1, 2008.
- Foken, T.: *Micrometeorology*, Springer Berlin Heidelberg, Berlin, Heidelberg, doi:10.1007/978-3-642-25440-6, 2017.
- Freundorfer, A.: Investigating the near-surface airflow and its turbulent and submesoscale statistics for the weak-wind regime from field experiments, *Master thesis, University of Bayreuth, Bayreuth*, 2017.
- Freundorfer, A., Lapo, K., Schneider, J., and Thomas, C. K.: Distributed sensing of wind direction using fiber-optic cables, *Journal of Atmospheric and Oceanic Technology*, doi:10.1175/JTECH-D-21-0019.1, 2021.
- Fritz, A. M., Lapo, K., Freundorfer, A., Linhardt, T., and Thomas, C. K.: Revealing the Morning Transition in the Mountain Boundary Layer Using Fiber-Optic Distributed Temperature Sensing, *Geophysical Research Letters*, 48, doi:10.1029/2020GL092238, 2021.
- Geiger, R., Aron, R. H., and Todhunter, P.: *The Climate Near the Ground*, Vieweg+Teubner Verlag, Wiesbaden, 7th ed. edn., doi:10.1007/978-3-322-86582-3, 1995.
- Hausner, M. B., Suárez, F., Glander, K. E., van de Giesen, N., Selker, J. S., and Tyler, S. W.: Calibrating single-ended fiber-optic Raman spectra distributed temperature sensing data, *Sensors (Basel, Switzerland)*, 11, 10859–10879, doi:10.3390/s111110859, 2011.
- Helgason, W. and Pomeroy, J.: Problems Closing the Energy Balance over a Homogeneous Snow Cover during Midwinter, *Journal of Hydrometeorology*, 13, 557–572, doi:10.1175/JHM-D-11-0135.1, 2012.
- Heusinkveld, B., Jacobs, A., Holtslag, A., and Berkowicz, S.: Surface energy balance closure in an arid region: role of soil heat flux, *Agricultural and Forest Meteorology*, 122, 21–37, doi:10.1016/j.agrformet.2003.09.005, 2004.

- Holton, J. R.: An introduction to dynamic meteorology, vol. 88 of *International geophysics series*, Academic Press, Amsterdam, 4. ed. edn., 2004.
- Holtslag, A. A. M., Svensson, G., Baas, P., Basu, S., Beare, B., Beljaars, A. C. M., Bosveld, F. C., Cuxart, J., Lindvall, J., Steeneveld, G. J., Tjernström, M., and van de Wiel, B. J. H.: Stable Atmospheric Boundary Layers and Diurnal Cycles: Challenges for Weather and Climate Models, *Bulletin of the American Meteorological Society*, 94, 1691–1706, doi:10.1175/BAMS-D-11-00187.1, 2013.
- Huss, J.-M., Zeller, M.-L., Pfister, L., Lapo, K. E., Littmann, D., Schneider, J., Schulz, A., and Thomas, C. K.: NYTEFOX - The NY-Ålesund TurbulencE Fiber Optic eXperiment investigating the Arctic boundary layer, Svalbard, doi:10.5281/zenodo.4335461, 2021.
- Högström, U. L. F.: Non-Dimensional Wind and Temperature Profiles in the Atmospheric Surface Layer: A Re-Evaluation, in: *Topics in Micrometeorology. A Festschrift for Arch Dyer*, pp. 55–78, doi:10.1007/978-94-009-2935-7{\textunderscore}6, 1988.
- Iwata, Y., Hayashi, M., and Hirota, T.: Effects of Snow Cover on Soil Heat Flux and Freezethaw Processes, *Journal of Agricultural Meteorology*, 64, 301–309, doi:10.2480/agrmet.64.4.12, 2008.
- Jocher, G., Karner, F., Ritter, C., Neuber, R., Dethloff, K., Obleitner, F., Reuder, J., and Foken, T.: The Near-Surface Small-Scale Spatial and Temporal Variability of Sensible and Latent Heat Exchange in the Svalbard Region: A Case Study, *ISRN Meteorology*, 2012, 1–14, doi:10.5402/2012/357925, 2012.
- Kanda, M., Inagaki, A., Letzel, M. O., Raasch, S., and Watanabe, T.: LES Study of the Energy Imbalance Problem with Eddy Covariance Fluxes, *Boundary-Layer Meteorology*, 110, 381–404, doi:10.1023/B:BOUN.0000007225.45548.7a, 2004.
- Kang, Y., Belušić, D., and Smith-Miles, K.: Classes of structures in the stable atmospheric boundary layer, *Quarterly Journal of the Royal Meteorological Society*, 141, 2057–2069, doi:10.1002/qj.2501, 2015.
- Lang, F., Belušić, D., and Siems, S.: Observations of Wind-Direction Variability in the Nocturnal Boundary Layer, *Boundary-Layer Meteorology*, 166, 51–68, doi:10.1007/s10546-017-0296-4, 2018.
- Lapo, K., Freundorfer, A., Pfister, L., Schneider, J., Selker, J., and Thomas, C.: Distributed observations of wind direction using microstructures attached to actively heated fiber-optic cables, *Atmospheric Measurement Techniques*, 13, 1563–1573, doi:10.5194/amt-13-1563-2020, 2020.
- Lapo, K., Freundorfer, A., Fritz, A., Schneider, J., Olesch, J., Babel, W., and Thomas, C. K.: The Large-eddy Observatory Voitsumra Experiment 2019 (LOVE19) with high-resolution, spatially-distributed observations of air temperature, wind speed, and wind direction from fiber-optic distributed sensing, towers, and ground-based remote sensing: [preprint], *Earth System Science Data*, doi:10.5194/essd-2020-392, 2021.

- Lapo, K. E. and Freundorfer, A.: pyfocs, doi:10.5281/zenodo.4292491, 2020.
- Li, D., Bou-Zeid, E., and de Bruin, H. A. R.: Monin–Obukhov Similarity Functions for the Structure Parameters of Temperature and Humidity, *Boundary-Layer Meteorology*, 145, 45–67, doi:10.1007/s10546-011-9660-y, 2012.
- LI-COR, Inc.: EddyPro Software, 2021.
- Linhardt, T.: Vertical structure of the lower polar troposphere observed in temperature and wind profiles from fiber-optic distributed sensing on a tethered balloon over Ny-Alesund, Svalbard, the Arctic, Master thesis, University of Bayreuth, Bayreuth, Germany, 2021.
- Lumley, J. L. and Panofsky, H. A.: The Structure of Atmospheric Turbulence, vol. v. 12 of *Interscience monographs and texts in physics and astronomy*, Interscience Publishers, New York, 1964.
- Mahrt, L.: Weak-wind mesoscale meandering in the nocturnal boundary layer, *Environmental Fluid Mechanics*, 7, 331–347, doi:10.1007/s10652-007-9024-9, 2007.
- Mahrt, L.: Variability and Maintenance of Turbulence in the Very Stable Boundary Layer, *Boundary-Layer Meteorology*, 135, 1–18, doi:10.1007/s10546-009-9463-6, 2010.
- Mahrt, L.: Stably Stratified Atmospheric Boundary Layers, *Annual Review of Fluid Mechanics*, 46, 23–45, doi:10.1146/annurev-fluid-010313-141354, 2014.
- Mahrt, L. and Thomas, C. K.: Surface Stress with Non-stationary Weak Winds and Stable Stratification, *Boundary-Layer Meteorology*, 159, 3–21, doi:10.1007/s10546-015-0111-z, 2016.
- Mahrt, L., Vickers, D., Nakamura, R., Soler, M. R., Sun, J., Burns, S., and Lenschow, D. H.: Shallow Drainage Flows, *Boundary-Layer Meteorology*, 101, 243–260, doi:10.1023/A:1019273314378, 2001.
- Mahrt, L., Thomas, C. K., and Prueger, J. H.: Space-time structure of mesoscale motions in the stable boundary layer, *Quarterly Journal of the Royal Meteorological Society*, 135, 67–75, doi:10.1002/qj.348, 2009.
- Mahrt, L., Thomas, C., Richardson, S., Seaman, N., Stauffer, D., and Zeeman, M.: Non-stationary Generation of Weak Turbulence for Very Stable and Weak-Wind Conditions, *Boundary-Layer Meteorology*, 147, 179–199, doi:10.1007/s10546-012-9782-x, 2013.
- Maturilli, M., Herber, A., and König-Langlo, G.: Climatology and time series of surface meteorology in Ny-Ålesund, Svalbard, *Earth System Science Data*, 5, 155–163, doi:10.5194/essd-5-155-2013, 2013.
- Maturilli, M., Herber, A., and König-Langlo, G.: Surface radiation climatology for Ny-Ålesund, Svalbard (78.9° N), basic observations for trend detection, *Theoretical and Applied Climatology*, 120, 331–339, doi:10.1007/s00704-014-1173-4, 2015.

- Mauder, M., Foken, T., and Cuxart, J.: Surface-Energy-Balance Closure over Land: A Review, *Boundary-Layer Meteorology*, 177, 395–426, doi:10.1007/s10546-020-00529-6, 2020.
- McNaughton, K. G. and Laubach, J.: Unsteadiness as a cause of non-equality of eddy diffusivities for heat and vapour at the base of an advective inversion, *Boundary-Layer Meteorology*, 88, 479–504, doi:10.1023/A:1001573521304, 1998.
- Meyers, T. P. and Hollinger, S. E.: An assessment of storage terms in the surface energy balance of maize and soybean, *Agricultural and Forest Meteorology*, 125, 105–115, doi:10.1016/j.agrformet.2004.03.001, 2004.
- Moncrieff, J., Clement, R., Finnigan, J. J., and Meyers, T. P.: Averaging, Detrending, and Filtering of Eddy Covariance Time Series, in: *Handbook of micrometeorology*, edited by Lee, X., Atmospheric and oceanographic sciences library, Kluwer Acad. Publ, Dordrecht, 2004.
- Moncrieff, J. B., Massheder, J. M., de Bruin, H., Elbers, J., Friborg, T., Heusinkveld, B., Kabat, P., Scott, S., Soegaard, H., and Verhoef, A.: A system to measure surface fluxes of momentum, sensible heat, water vapour and carbon dioxide, *Journal of Hydrology*, 188–189, 589–611, doi:10.1016/S0022-1694(96)03194-0, 1997.
- Monin, A. S. and Obukhov, A. M.: Basic laws of turbulent mixing in the surface layer of the atmosphere, *Contrib. Geophys. Inst. Acad. Sci. USSR*, e187, 151–163, 1954.
- Nakamura, R. and Mahrt, L.: A study of intermittent turbulence with cases-99 tower measurements, *Boundary-Layer Meteorology*, 114, 367–387, doi:10.1007/s10546-004-0857-1, 2005.
- Nappo, C. J.: Sporadic breakdowns of stability in the PBL over simple and complex terrain, *Boundary-Layer Meteorology*, 54, 69–87, doi:10.1007/BF00119413, URL <https://doi.org/10.1007/BF00119413>, 1991.
- Norwegian Center for Climate Services: Seklima: Observations and weather statistics, URL <https://seklima.met.no>.
- Norwegian Polar Institute: Svalbardkartet, URL [svalbardkartet.npolar.no/Html5Svb/index.html?viewer=Svalbardkartet](http://svalbardkartet.npolar.no/Html5Svb/index.html?viewer=Svalbardkartet).
- Optis, M., Monahan, A., and Bosveld, F. C.: Limitations and breakdown of Monin-Obukhov similarity theory for wind profile extrapolation under stable stratification, *Wind Energy*, 19, 1053–1072, doi:10.1002/we.1883, 2016.
- Overland, J. E., Dethloff, K., Francis, J. A., Hall, R. J., Hanna, E., Kim, S.-J., Screen, J. A., Shepherd, T. G., and Vihma, T.: Nonlinear response of mid-latitude weather to the changing Arctic, *Nature Climate Change*, 6, 992–999, doi:10.1038/nclimate3121, 2016.
- Peltola, O., Lapo, K., Martinkauppi, I., O’Connor, E., Thomas, C. K., and Vesala, T.: Suitability of fibre-optic distributed temperature sensing for revealing mixing processes and higher-order moments at the forest–air interface, *Atmospheric Measurement Techniques*, 14, 2409–2427, doi:10.5194/amt-14-2409-2021, 2021.

- Pfister, L., Sigmund, A., Olesch, J., and Thomas, C. K.: Nocturnal Near-Surface Temperature, but not Flow Dynamics, can be Predicted by Microtopography in a Mid-Range Mountain Valley, *Boundary-Layer Meteorology*, 165, 333–348, doi:10.1007/s10546-017-0281-y, 2017.
- Pfister, L., Lapo, K., Sayde, C., Selker, J., Mahrt, L., and Thomas, C. K.: Classifying the nocturnal atmospheric boundary layer into temperature and flow regimes, *Quarterly Journal of the Royal Meteorological Society*, 142, 693, doi:10.1002/qj.3508, 2019.
- Pfister, L., Lapo, K., Mahrt, L., and Thomas, C. K.: Thermal Submeso Motions in the Nocturnal Stable Boundary Layer. Part 2: Generating Mechanisms and Implications, *Boundary-Layer Meteorology*, 180, 203–224, doi:10.1007/s10546-021-00619-z, 2021a.
- Pfister, L., Lapo, K., Mahrt, L., and Thomas, C. K.: Thermal Submesoscale Motions in the Nocturnal Stable Boundary Layer. Part 1: Detection and Mean Statistics, *Boundary-Layer Meteorology*, 180, 187–202, doi:10.1007/s10546-021-00618-0, 2021b.
- R Core Team: R: A language and environment for statistical computing, URL <https://www.R-project.org/>, 2021.
- Sandu, I., Beljaars, A., Bechtold, P., Mauritsen, T., and Balsamo, G.: Why is it so difficult to represent stably stratified conditions in numerical weather prediction (NWP) models?, *Journal of Advances in Modeling Earth Systems*, 5, 117–133, doi:10.1002/jame.20013, 2013.
- Sayde, C., Gregory, C., Gil-Rodriguez, M., Tuffiaro, N., Tyler, S., van de Giesen, N., English, M., Cuenca, R., and Selker, J. S.: Feasibility of soil moisture monitoring with heated fiber optics, *Water Resources Research*, 46, doi:10.1029/2009WR007846, 2010.
- Sayde, C., Thomas, C. K., Wagner, J., and Selker, J.: High-resolution wind speed measurements using actively heated fiber optics, *Geophysical Research Letters*, 42, 10,064–10,073, doi:10.1002/2015GL066729, 2015.
- Schlögl, S., Lehning, M., and Mott, R.: How Are Turbulent Sensible Heat Fluxes and Snow Melt Rates Affected by a Changing Snow Cover Fraction?, *Frontiers in Earth Science*, 6, doi:10.3389/feart.2018.00154, 2018.
- Schulz, A.: Untersuchung der Wechselwirkung synoptisch-skaliger mit orographisch bedingten Prozessen in der arktischen Grenzschicht über Spitzbergen, Phd thesis, University of Potsdam, Potsdam, URL <http://nbn-resolving.de/urn:nbn:de:kobv:517-opus4-400058>, 2017.
- Screen, J. A. and Simmonds, I.: The central role of diminishing sea ice in recent Arctic temperature amplification, *Nature*, 464, 1334–1337, doi:10.1038/nature09051, 2010.
- Selker, J. S., Thévenaz, L., Huwald, H., Mallet, A., Luxemburg, W., van de Giesen, N., Stejskal, M., Zeman, J., Westhoff, M., and Parlange, M. B.: Distributed fiber-optic temperature sensing for hydrologic systems, *Water Resources Research*, 42, 1038, doi:10.1029/2006WR005326, 2006.

- Shepard, D.: A two-dimensional interpolation function for irregularly-spaced data, in: Proceedings of the 1968 23rd ACM national conference, pp. 517–524, doi:10.1145/800186.810616, 1968.
- Solomon, S., ed.: Climate change 2007: The physical science basis, vol. contribution of ... to the fourth assessment report of the Intergovernmental Panel on Climate Change ; Working Group 1 of *Climate change 2007*, Cambridge Univ. Press, Cambridge, 2007.
- Stocker, T., Alexander, L., and Allen, M., eds.: Climate change 2013: The physical science basis ; Working Group I contribution to the fifth assessment report of the Intergovernmental Panel on Climate Change, WMO IPCC, Cambridge, United Kingdom and New York, NY, USA, [elektronische ressource] edn., doi:10.1017/CBO9781107415324, 2014.
- Stull, R. B.: An Introduction to Boundary Layer Meteorology, Springer Netherlands, Dordrecht, doi:10.1007/978-94-009-3027-8, 1988.
- Sun, J., Burns, S. P., Lenschow, D. H., Banta, R., Newsom, R., Coulter, R., Frasier, S., Ince, T., Nappo, C., Cuxart, J., Blumen, W., Lee, X., and Hu, X.-Z.: Intermittent Turbulence Associated with a Density Current Passage in the Stable Boundary Layer, *Boundary-Layer Meteorology*, 105, 199–219, doi:10.1023/A:1019969131774, 2002.
- Sun, J., Mahrt, L., Banta, R. M., and Pichugina, Y. L.: Turbulence Regimes and Turbulence Intermittency in the Stable Boundary Layer during CASES-99, *Journal of the Atmospheric Sciences*, 69, 338–351, doi:10.1175/JAS-D-11-082.1, 2012.
- Sun, J., Takle, E. S., and Acevedo, O. C.: Understanding Physical Processes Represented by the Monin–Obukhov Bulk Formula for Momentum Transfer, *Boundary-Layer Meteorology*, 177, 69–95, doi:10.1007/s10546-020-00546-5, 2020.
- Tarroso, P., Carvalho, S. B., and Velo-Antón, G.: Phylin 2.0: Extending the phylogeographical interpolation method to include uncertainty and user-defined distance metrics, *Molecular ecology resources*, 19, 1081–1094, doi:10.1111/1755-0998.13010, 2019.
- Taylor, G. I.: The Spectrum of Turbulence, *Proceedings of the Royal Society of London. Series A - Mathematical and Physical Sciences*, 164, 476–490, doi:10.1098/rspa.1938.0032, 1938.
- Thomas, C. K.: Variability of Sub-Canopy Flow, Temperature, and Horizontal Advection in Moderately Complex Terrain, *Boundary-Layer Meteorology*, 139, 61–81, doi:10.1007/s10546-010-9578-9, 2011.
- Thomas, C. K.: Thresholds for static stability, 2020.
- Thomas, C. K. and Selker, J. S.: Optical fiber-based distributed sensing methods, in: *Handbook of Atmospheric Measurements*, edited by Foken, T., p. 1705 pp., Springer International Publishing, 2021.
- Thomas, C. K., Kennedy, A. M., Selker, J. S., Moretti, A., Schroth, M. H., Smoot, A. R., Tuffiaro, N. B., and Zeeman, M. J.: High-Resolution Fibre-Optic Temperature Sensing:

- A New Tool to Study the Two-Dimensional Structure of Atmospheric Surface-Layer Flow, *Boundary-Layer Meteorology*, 142, 177–192, doi:10.1007/s10546-011-9672-7, 2012.
- Tyler, S. W., Selker, J. S., Hausner, M. B., Hatch, C. E., Torgersen, T., Thodal, C. E., and Schladow, S. G.: Environmental temperature sensing using Raman spectra DTS fiber-optic methods, *Water Resources Research*, 45, 951, doi:10.1029/2008WR007052, 2009.
- van de Wiel, B. J. H., Ronda, R. J., Moene, A. F., de Bruin, H. A. R., and Holtslag, A. A. M.: Intermittent Turbulence and Oscillations in the Stable Boundary Layer over Land. Part I: A Bulk Model, *Journal of the Atmospheric Sciences*, 59, 942–958, doi:10.1175/1520-0469(2002)059<0942:ITAOIT>2.0.CO;2, 2002.
- van Ramshorst, J. G. V., Coenders-Gerrits, M., Schilperoort, B., van de Wiel, B. J. H., Izett, J. G., Selker, J. S., Higgins, C. W., Savenije, H. H. G., and van de Giesen, N. C.: Revisiting wind speed measurements using actively heated fiber optics: a wind tunnel study, *Atmospheric Measurement Techniques*, 13, 5423–5439, doi:10.5194/amt-13-5423-2020, 2020.
- van Rossum, G. and Drake, F. L.: The Python language reference, vol. / Guido van Rossum; Fred L. Drake ed. ; Pt. 2 of *Documentation for Python*, Python Software Foundation and SoHo Books, Hampton, NH and Redwood City, Calif., release 3.0.1 [repr.] edn., 2010.
- Vickers, D. and Mahrt, L.: Observations of the cross-wind velocity variance in the stable boundary layer, *Environmental Fluid Mechanics*, 7, 55–71, doi:10.1007/s10652-006-9010-7, 2007.
- Vila-Guerau de Arellano, J., van C. Heerwaarden, C., van J. H. Stratum, B., and van den Dries, K.: *Atmospheric Boundary Layer*, Cambridge University Press, Cambridge, doi:10.1017/CBO9781316117422, 2015.
- Webb, E. K., Pearman, G. I., and Leuning, R.: Correction of flux measurements for density effects due to heat and water vapour transfer, *Quarterly Journal of the Royal Meteorological Society*, 106, 85–100, doi:10.1002/qj.49710644707, 1980.
- Wilkinson, G. N. and Rogers, C. E.: Symbolic Description of Factorial Models for Analysis of Variance, *Applied Statistics*, 22, 392, doi:10.2307/2346786, 1973.
- Williams, A. G., Chambers, S., and Griffiths, A.: Bulk Mixing and Decoupling of the Nocturnal Stable Boundary Layer Characterized Using a Ubiquitous Natural Tracer, *Boundary-Layer Meteorology*, 149, 381–402, doi:10.1007/s10546-013-9849-3, 2013.
- Zeeman, M. J., Selker, J. S., and Thomas, C. K.: Near-Surface Motion in the Nocturnal, Stable Boundary Layer Observed with Fibre-Optic Distributed Temperature Sensing, *Boundary-Layer Meteorology*, 154, 189–205, doi:10.1007/s10546-014-9972-9, 2015.
- Zeller, M.-L.: Analysis of the spatio-temporal variability of the stable atmospheric boundary layer dynamics at Ny-Ålesund, Svalbard: Results from the NY-Ålesund Turbulence Fibre-Optic eXperiment (NYTEFOX) 2020, Master thesis, University of Potsdam, Patsdam, 2020.

Zeller, M.-L., Huss, J.-M., Pfister, L., Lapo, K. E., Littmann, D., Schneider, J., Schulz, A., and Thomas, C. K.: The NY-Ålesund Turbulence Fiber Optic eXperiment (NYTEFOX): investigating the Arctic boundary layer, Svalbard, *Earth System Science Data*, 13, 3439–3452, doi:10.5194/essd-13-3439-2021, 2021.



# A. Additional figures

## A.1. To methods

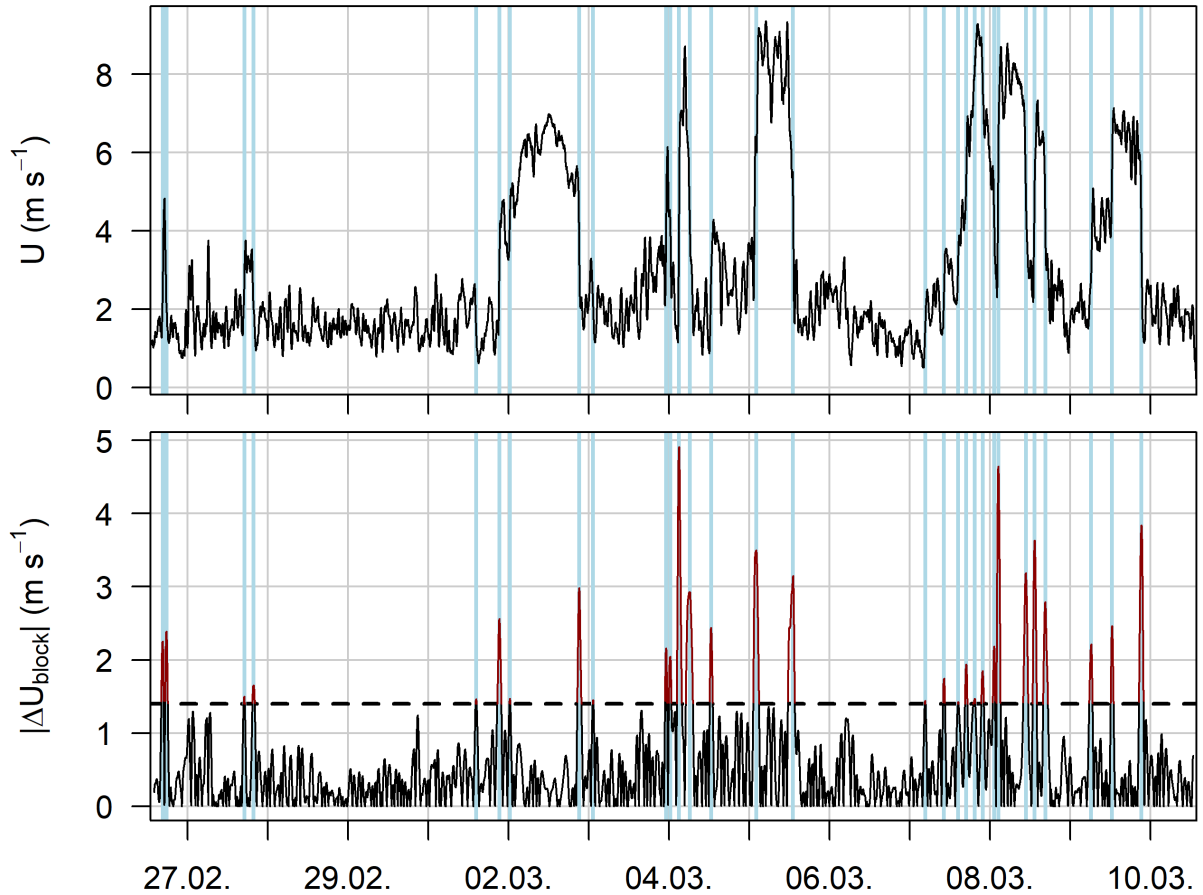


Figure A.1.: Average wind speed  $U$  of the ultrasonic anemometers (USAs) for the whole campaign period (top) and absolute change in wind speed between two averaging blocks ( $|\Delta U_{\text{block}}|$ ) of 60 min length, shifted along the time series (bottom). The dashed horizontal line marks a threshold value of  $1.4 \text{ K}$ . Changes above this threshold, highlighted as red sections of the curve, were used as indicators for strong wind speed changes. The time series was cut into separate blocks for computation of fiber-optic distributed sensing (FODS) wind speeds at the maximum  $dU/dt$  of each of these sections, marked by the light blue, vertical lines (see Sect. 2.4.1.2).

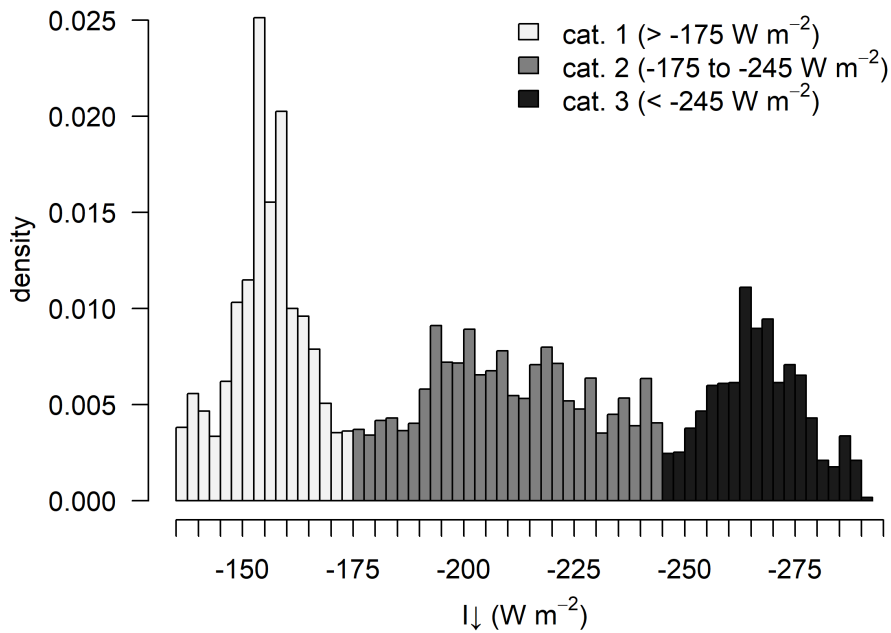


Figure A.2.: Distribution of longwave incoming radiation  $I_{\downarrow}$  for the whole campaign period. Colors indicate the regime categories 1 to 4 as outlined in section 2.5.3).

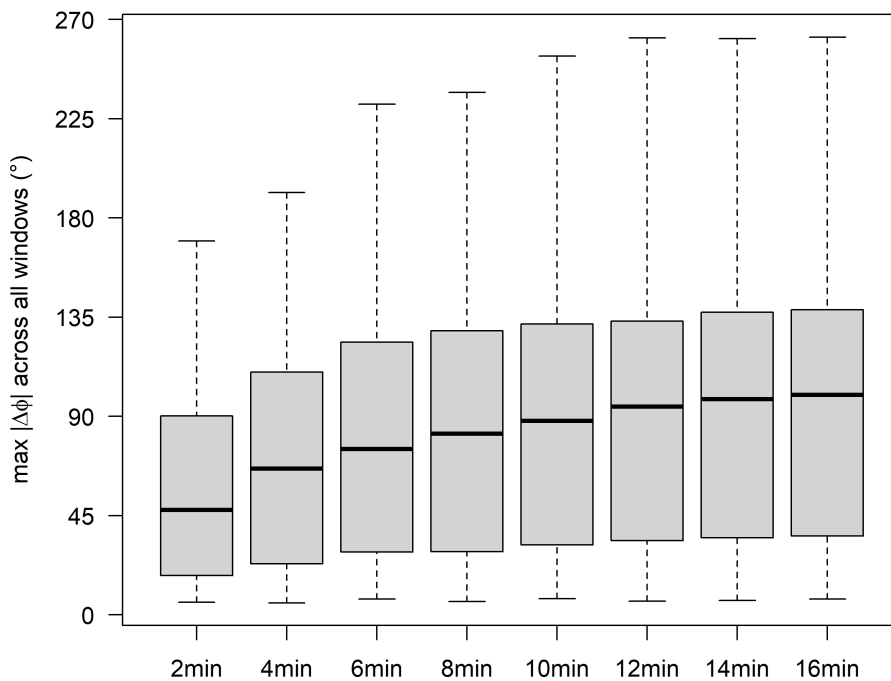


Figure A.3.: Boxplot of the maximum absolute changes in wind direction  $\Delta\phi$  vs. different maximum time window lengths from 2 min to 16 min. The method is applied for 2 min wind direction data measured by the ultrasonic anemometer (USA) at the EDDY tower and covers all windows used for meandering detection (see Sect. 2.5.4).

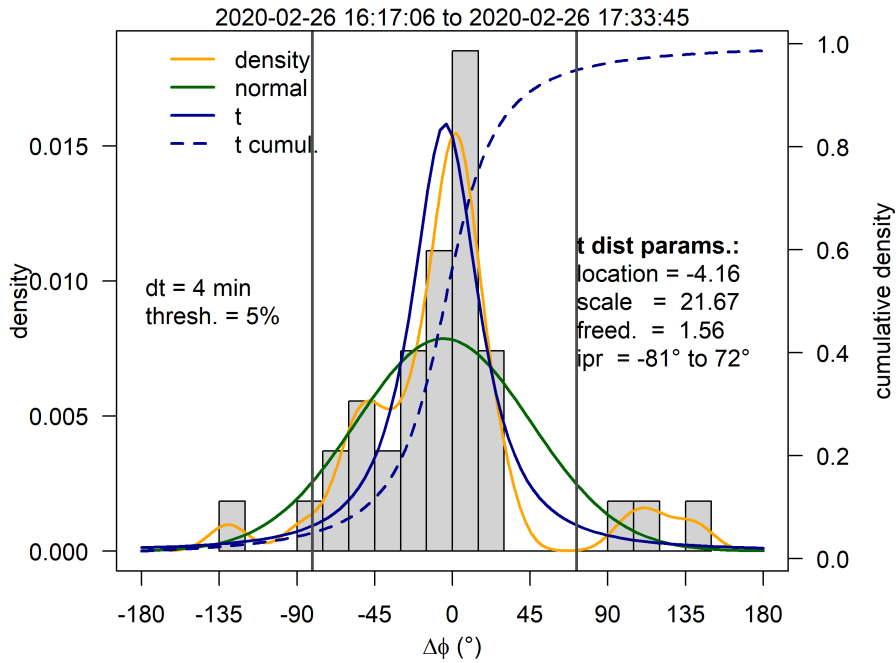


Figure A.4.: Histogram of wind-directional changes  $\Delta\varphi$ , derived as outlined in section 2.5.4 for a 77 min long time window on 26.02.2020. The orange curve visualizes the smoothed density distribution of the directional changes while the green curve shows the density of a normal distribution based on the mean and standard deviation of the directional changes. The blue solid curve is the density of a students t-distribution fitted to the distribution of directional changes while the blue dashed curve is the cumulative density of this students t-distribution. The vertical grey bars indicate the 5<sup>th</sup> and 95<sup>th</sup> percentile of the students t-distribution, indicated by 'thresh. = 5%'. The distributions fitting parameters ('location', 'scale' and 'freed.' for degrees of freedom) as well as the percentiles ('ipr' for interpercentile range) are listed below 't dist params.'. 'dt' sates the maximum time difference over which  $\Delta\varphi$  was computed (see Sect. 2.5.4).

## A.2. To results and discussion

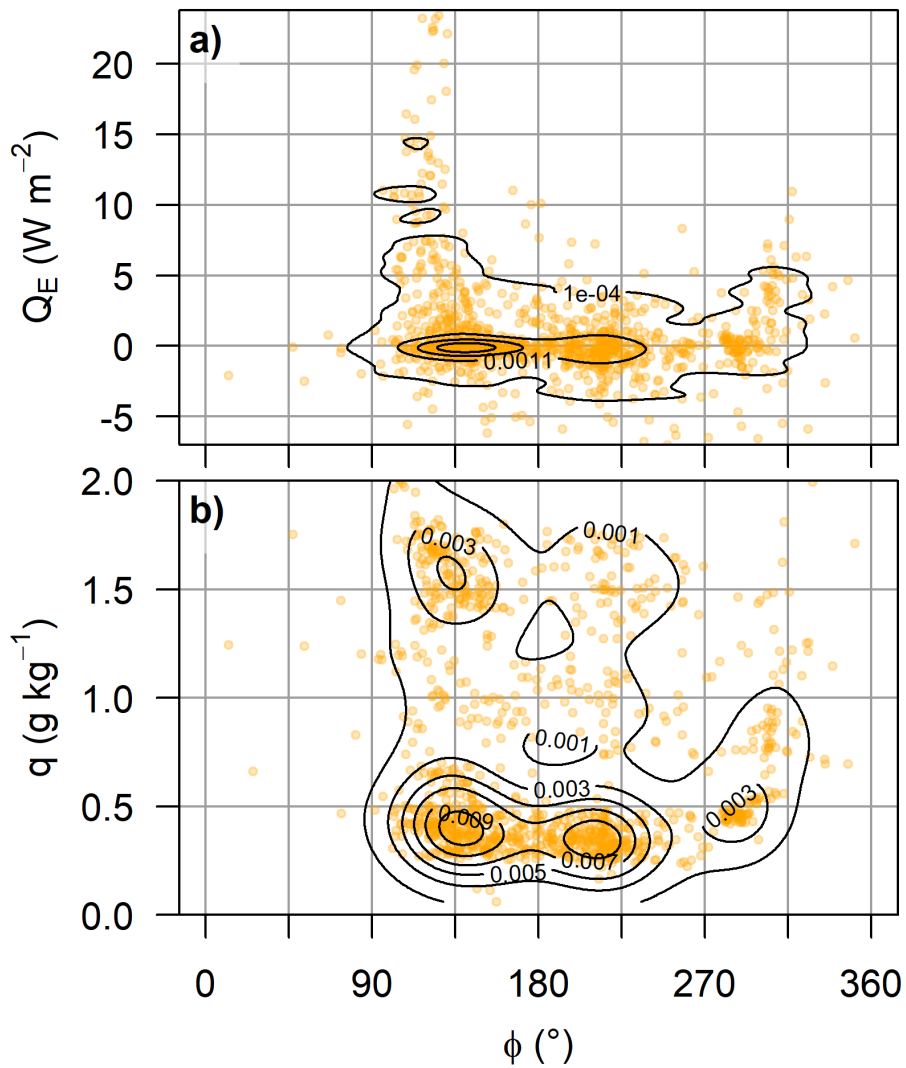


Figure A.5.: Scatter plots of (a) the latent heat flux  $Q_E$  and (b) the specific humidity  $q$  vs wind direction  $\varphi$ , measured by the eddy covariance (EC) station of the Alfred Wegener Institute for Polar and Marine Research (AWI) for the whole measuring period. The perturbation time scale is 10 min. The contour lines display the point densities. The ranges of the y-axes are slightly reduced for better distinguishability of values with small magnitude, cutting off some of the data points with very large magnitudes.

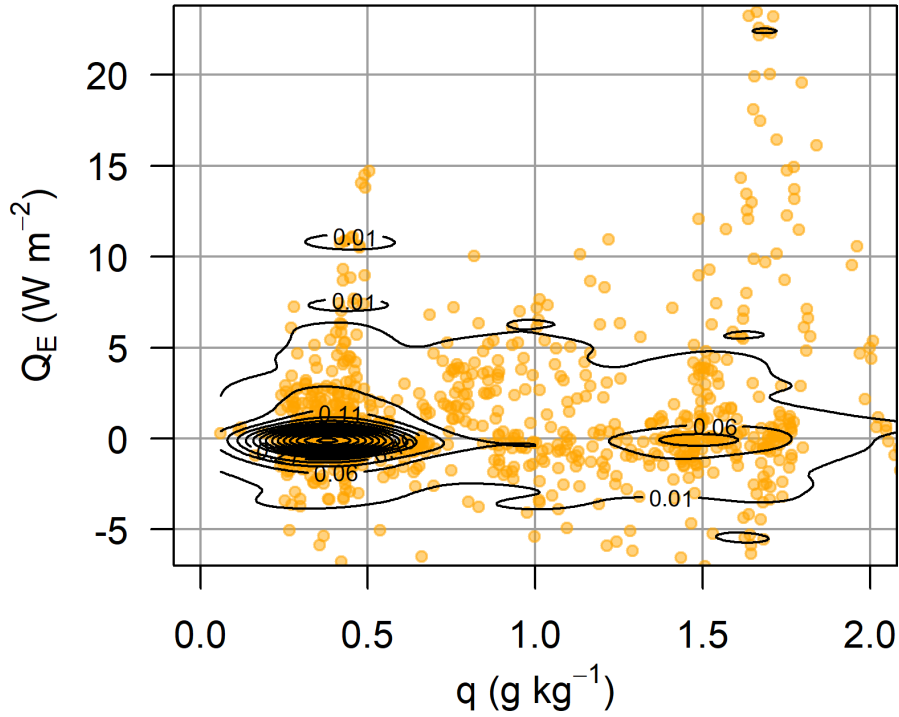


Figure A.6.: Scatter plots of latent heat flux  $Q_E$  over specific humidity  $q$ , measured by the eddy covariance (EC) station of the Alfred Wegener Institute for Polar and Marine Research (AWI) for the whole measuring period. The perturbation time scale is 10 min. The contour lines display the point densities. The ranges of the x- and y-axes are slightly reduced for better distinguishability of values with small magnitude, cutting off some of the data points with very large magnitudes.

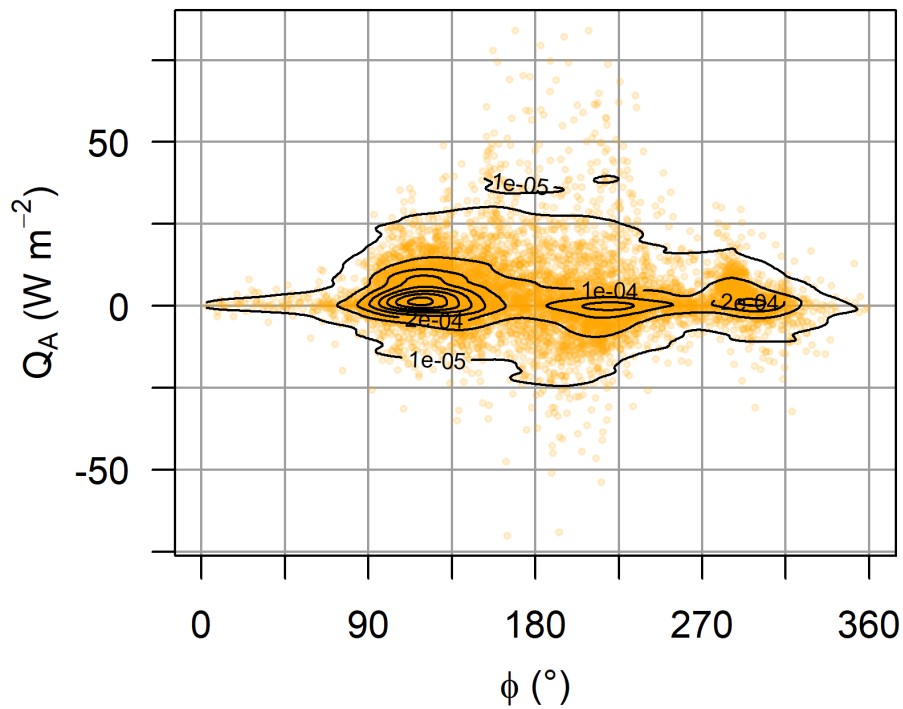


Figure A.7.: Scatter plot of horizontal advection of latent heat  $Q_A$  vs wind direction  $\phi$ , measured by the NYTEFOX EDDY tower for the whole measuring period. The temporal resolution is 2 min. The contour lines display the point densities.

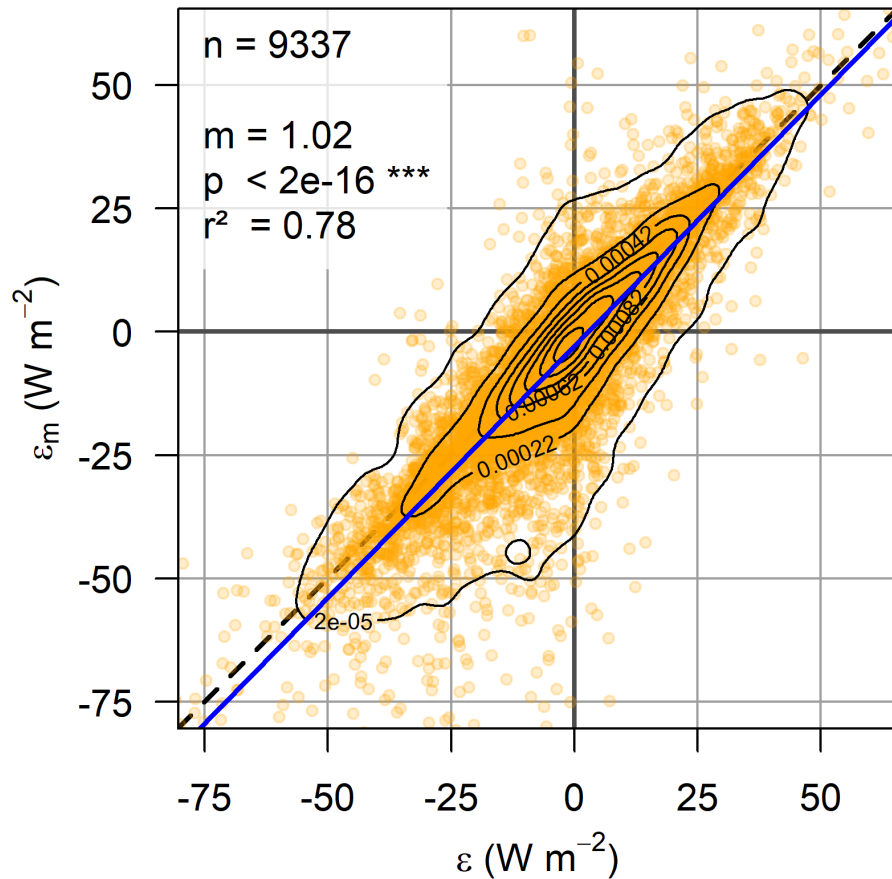


Figure A.8.: Scatter plot between the residual of the surface energy balance with ( $\epsilon$ , see Eq. 2.2) and without ( $\epsilon_m$ , see Eq. 2.6) horizontal advection of sensible heat. The temporal resolution is 2 min and  $n$  is the sample size. The contour lines display the point densities. The dashed black line is the 1:1 relation while the solid blue line represents a linear model with the models slope  $m$  and the respective  $p$ -value as well as the squared person correlation coefficient  $r^2$ .

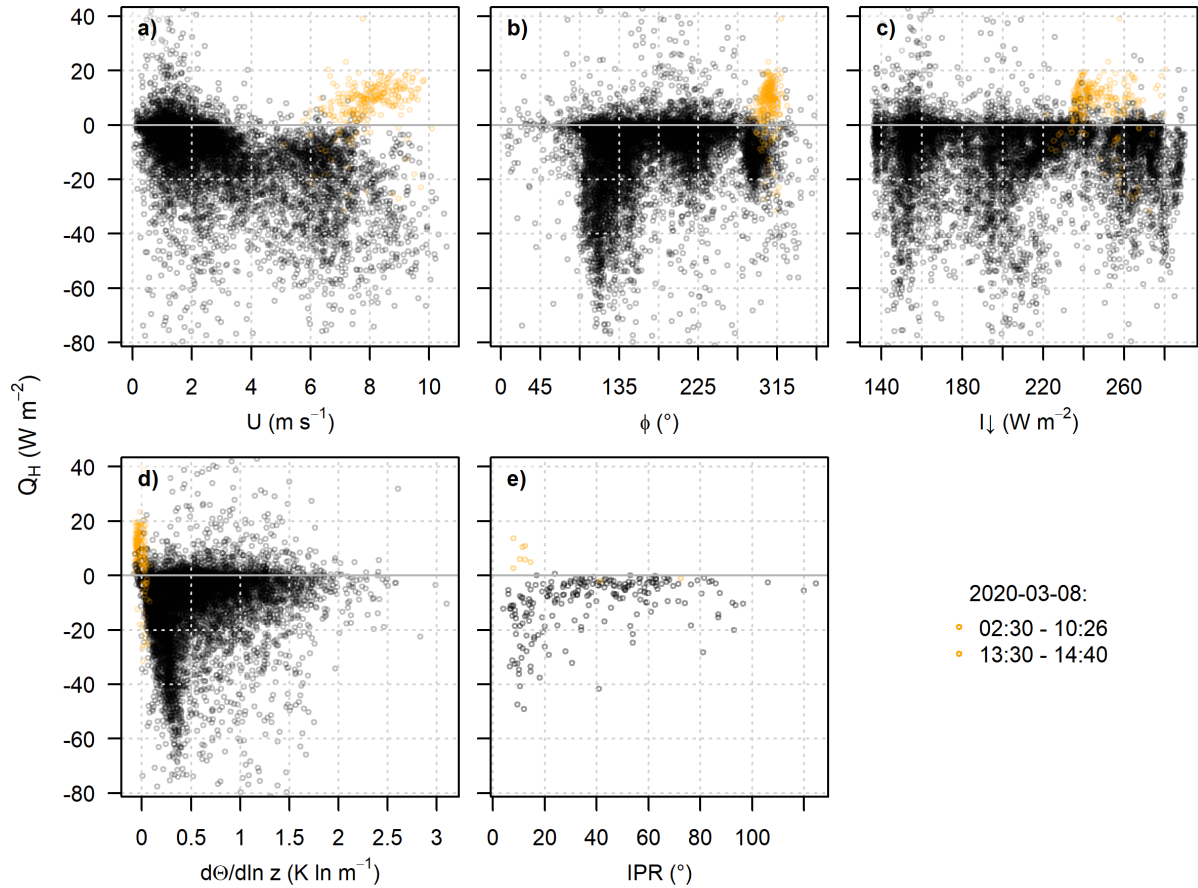


Figure A.9.: Scatter plot of the buoyancy flux  $Q_H$  vs the regime parameters a) wind velocity, b) wind direction, c) long wave downwelling radiation, d) static stability and e) the meandering indicator interpercentile range (IPR) (see Sect. 2.5.3). The y-axis is set so that the 0.1<sup>th</sup> to 99.9<sup>th</sup> percentile are pictured, cutting off extreme outliers. Orange color marks the periods from 08.03.2020, 02:30 to 10:26 and 13:30 to 14:40 UTC.

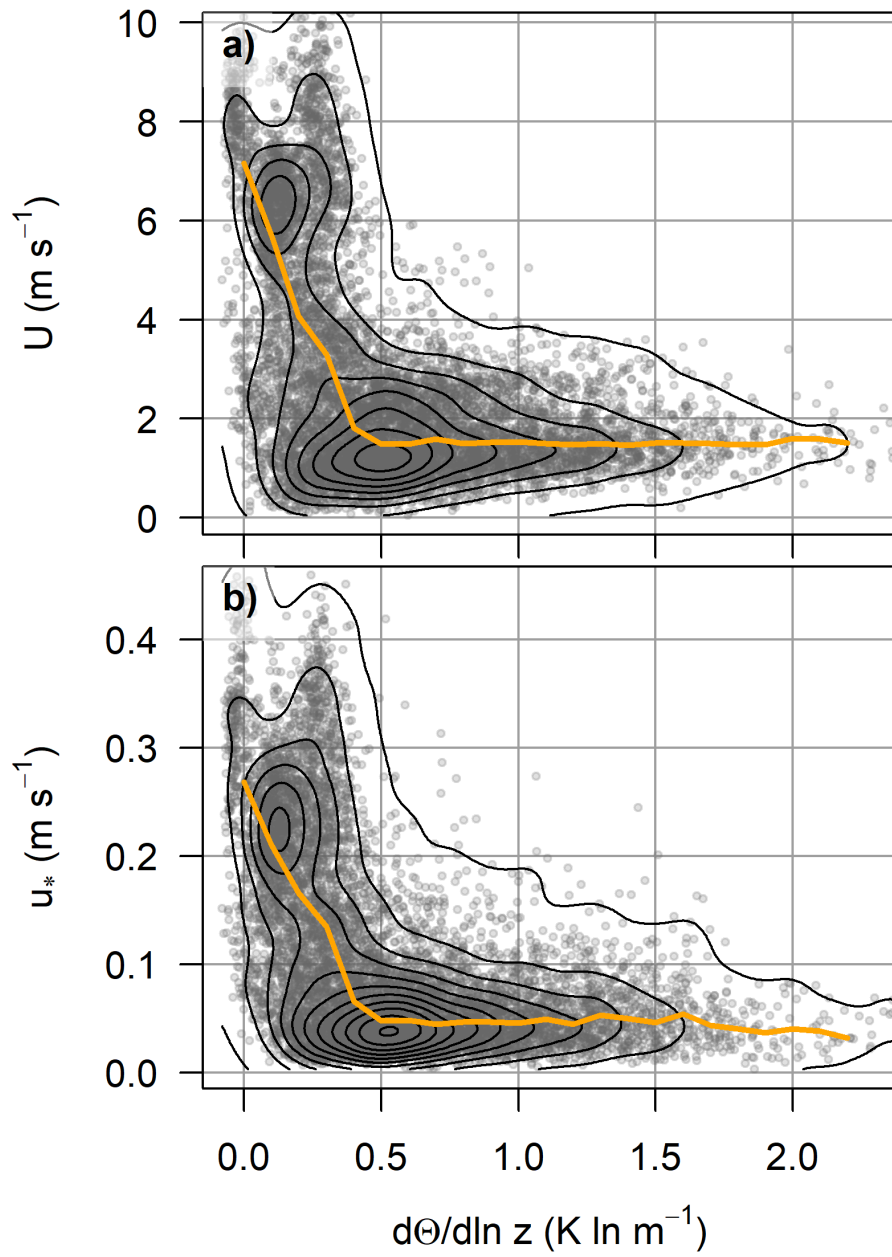


Figure A.10.: Scatter plot of the wind velocity  $U$  (a) and friction velocity  $u_*$  (b) vs static stability for the whole measuring period. The orange lines represents bin averages of  $0.1 \text{ K ln m}^{-1}$  width. The contour lines depict the point density.

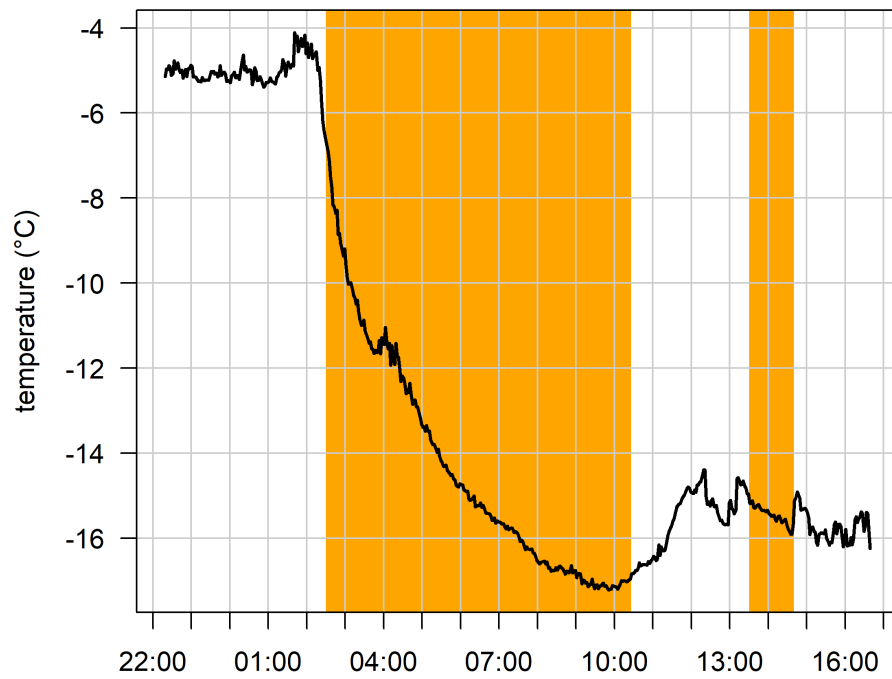


Figure A.11.: Sonic temperature  $T_s$  at Eddy tower for 07.03.2020, 22:00 to 08.03.2020, 17:00 UTC. The orange area marks the periods highlighted in A.9. The abrupt temperature drop explains the positive buoyancy flux  $Q_H$  for the highlighted periods.

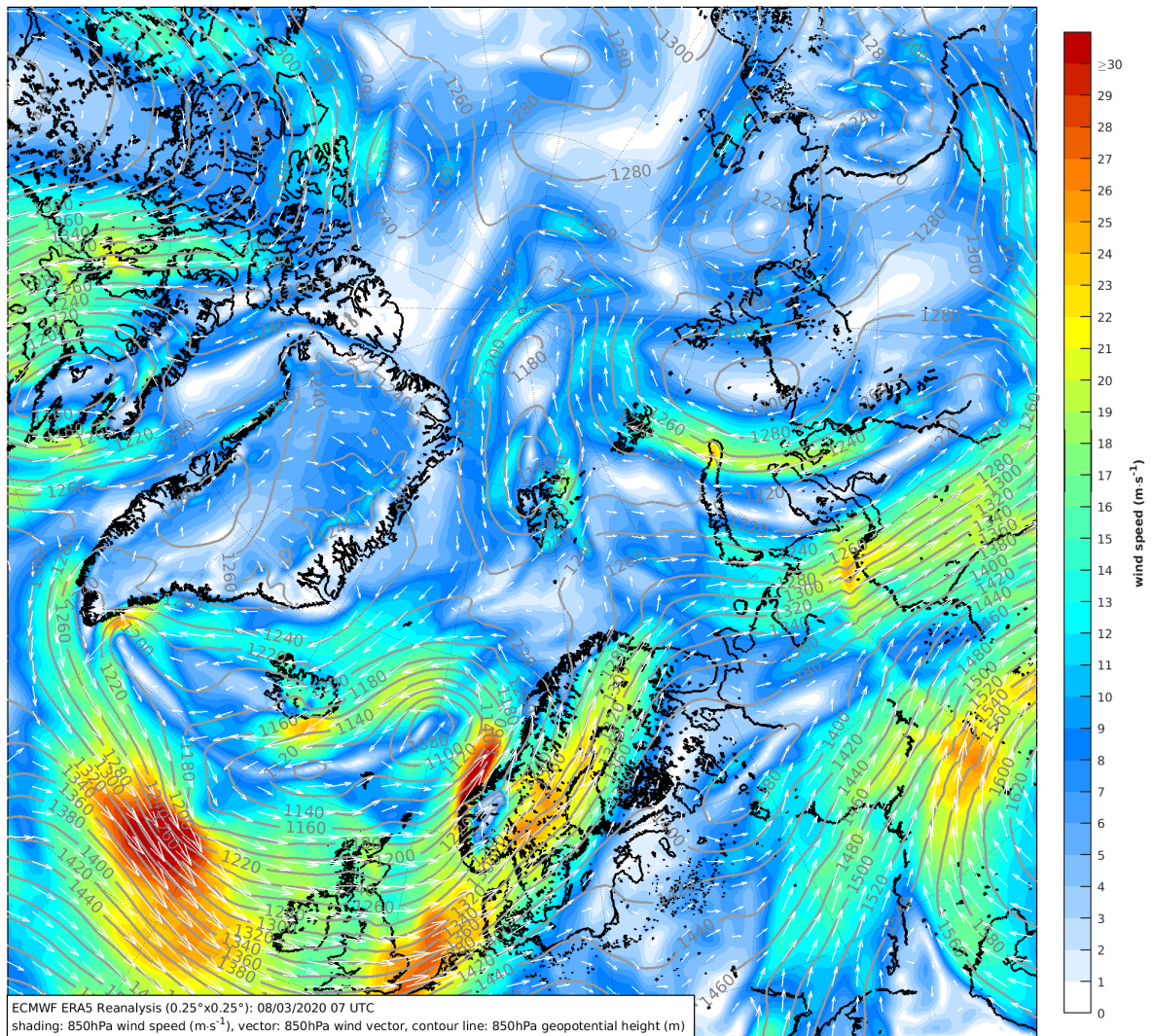


Figure A.12.: ECMWF Reanalysis v5 (ERA5) for 08.03.2020, 07:00 UTC. Shading: 850 hPa wind speeds; vectors: 850 hPa wind vectors; contour lines: 850 hPa geopotential height (GPH) in meter. Plot by Dr. Alexander Schulz.

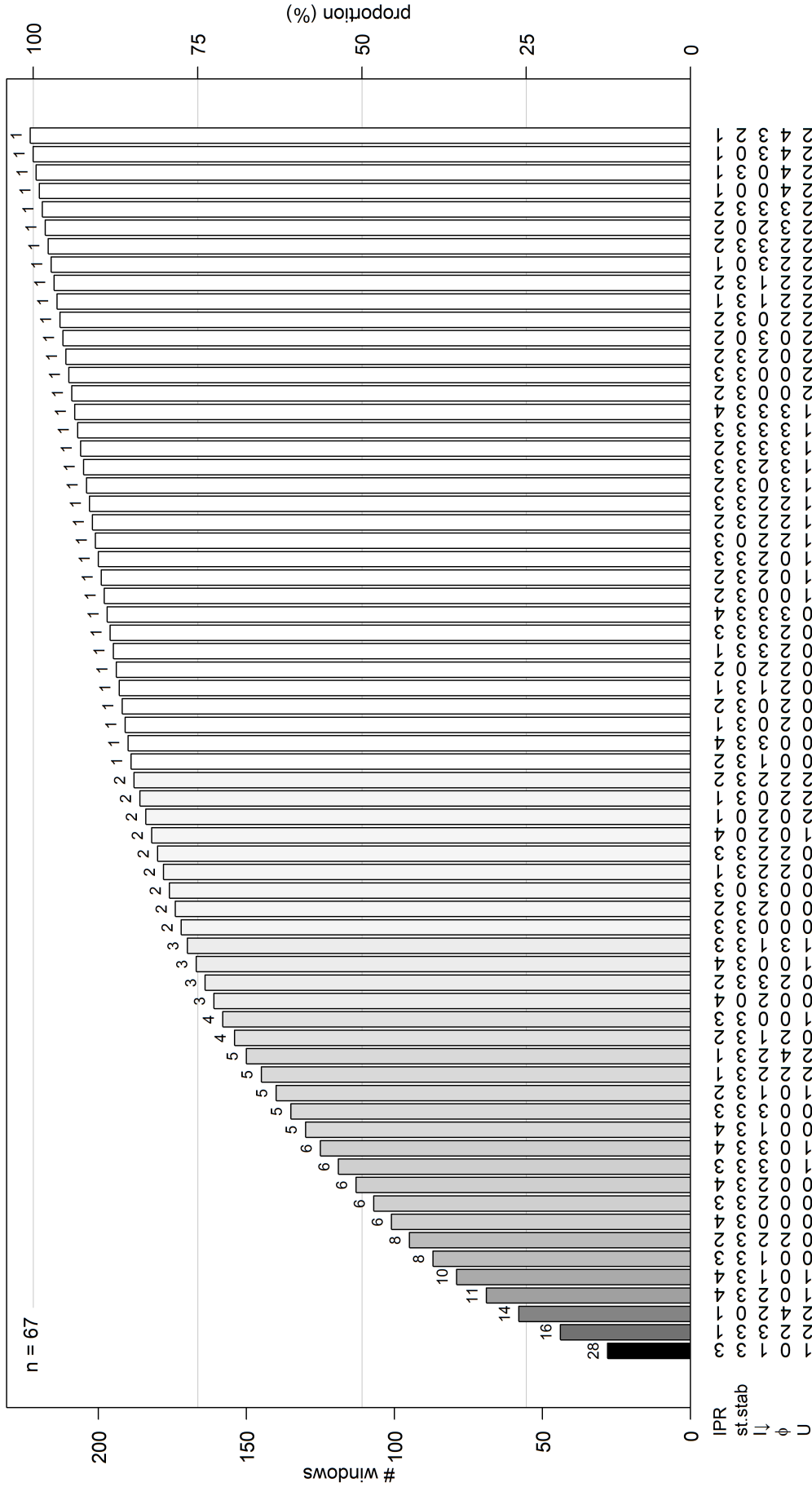


Figure A.13.: Cumulative barplot of the occurrence of all occurring boundary layer regimes (Sect. 2.5.3) within the measuring period. This covers 67 out of 960 possible regimes. The numbers above the bars as well as the grayscale indicate the number of windows for the respective regime. The numbers below the x-axis represent the regime categories as listed in table 2.1 where 0 indicates that no category covered at least 90% of the respective window. The integers stand for wind speed  $U$ , wind direction  $\varphi$ , longwave downwelling radiation  $I_{\downarrow}$ , static stability  $st.stab$  and meandering intensity interpercentile range (IPR). Windows with identical number of occurrence are ordered by their regime category numbers.

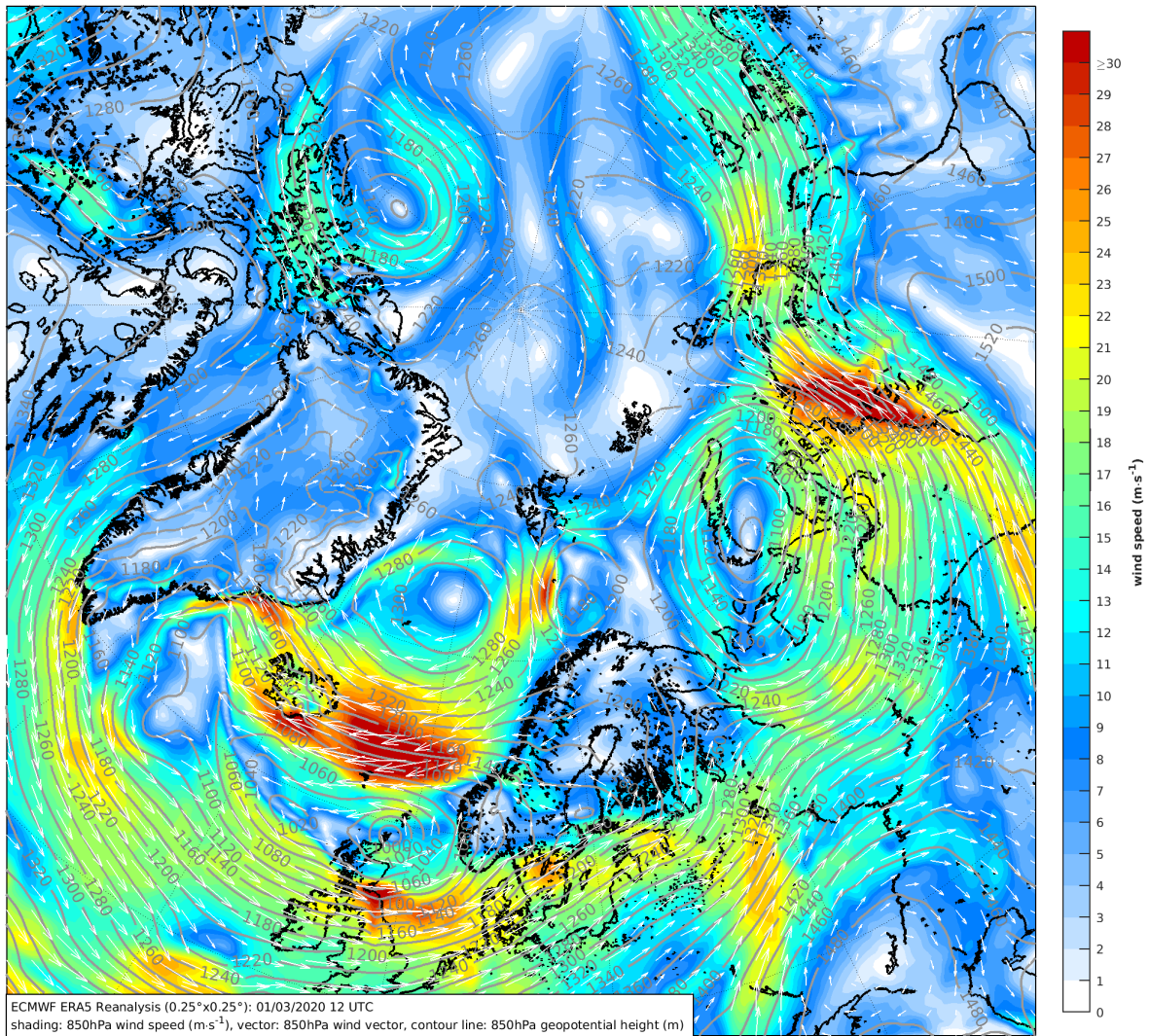


Figure A.14.: ECMWF Reanalysis v5 (ERA5) for 02.03.2020, 12:00 UTC. Shading: 850 hPa wind speeds; vectors: 850 hPa wind vectors; contour lines: 850 hPa geopotential height (GPH) in meter. Plot by Dr. Alexander Schulz.

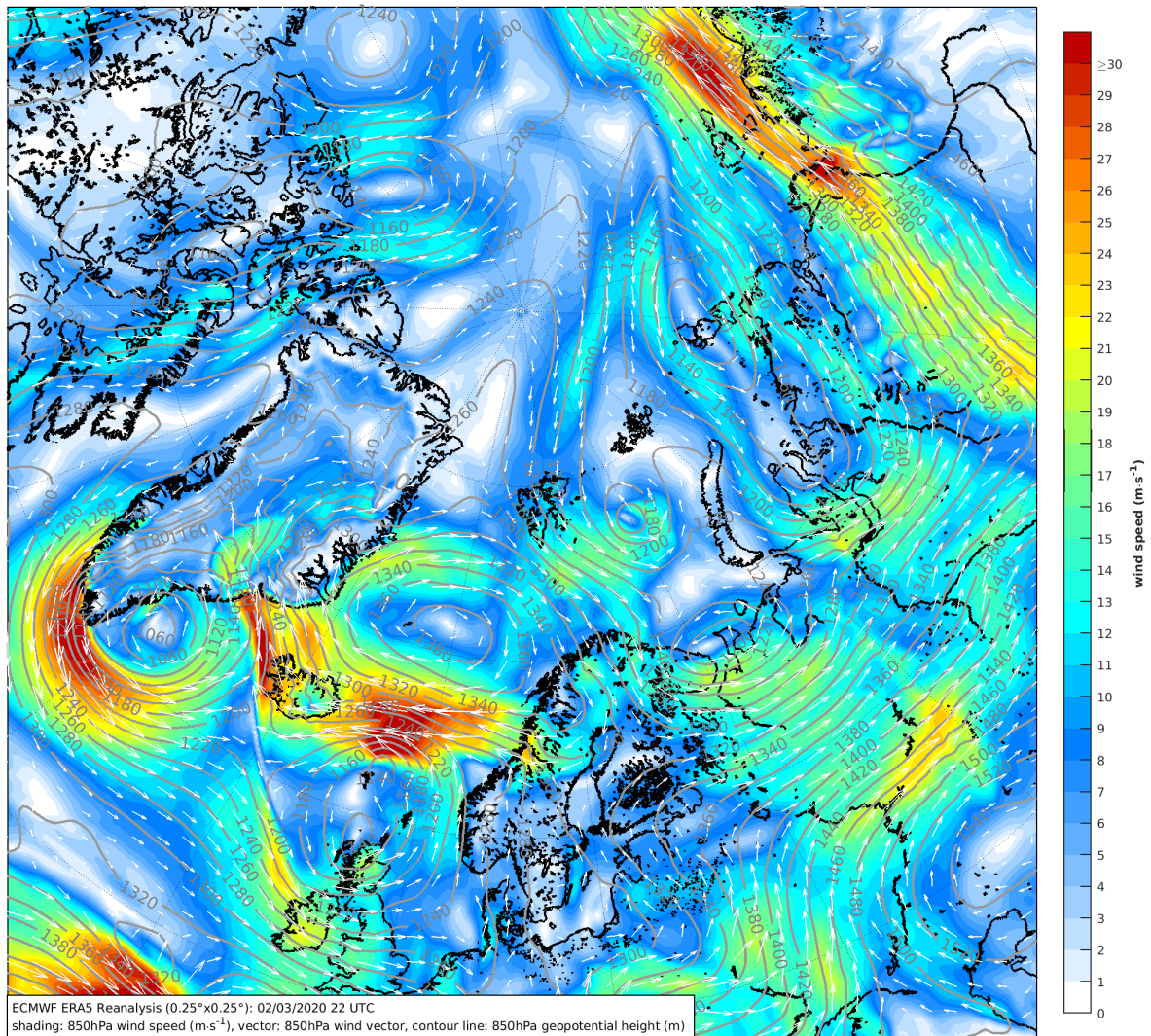


Figure A.15.: ECMWF Reanalysis v5 (ERA5) for 03.03.2020, 22:00 UTC. Shading: 850 hPa wind speeds; vectors: 850 hPa wind vectors; contour lines: 850 hPa geopotential height (GPH) in meter. Plot by Dr. Alexander Schulz.

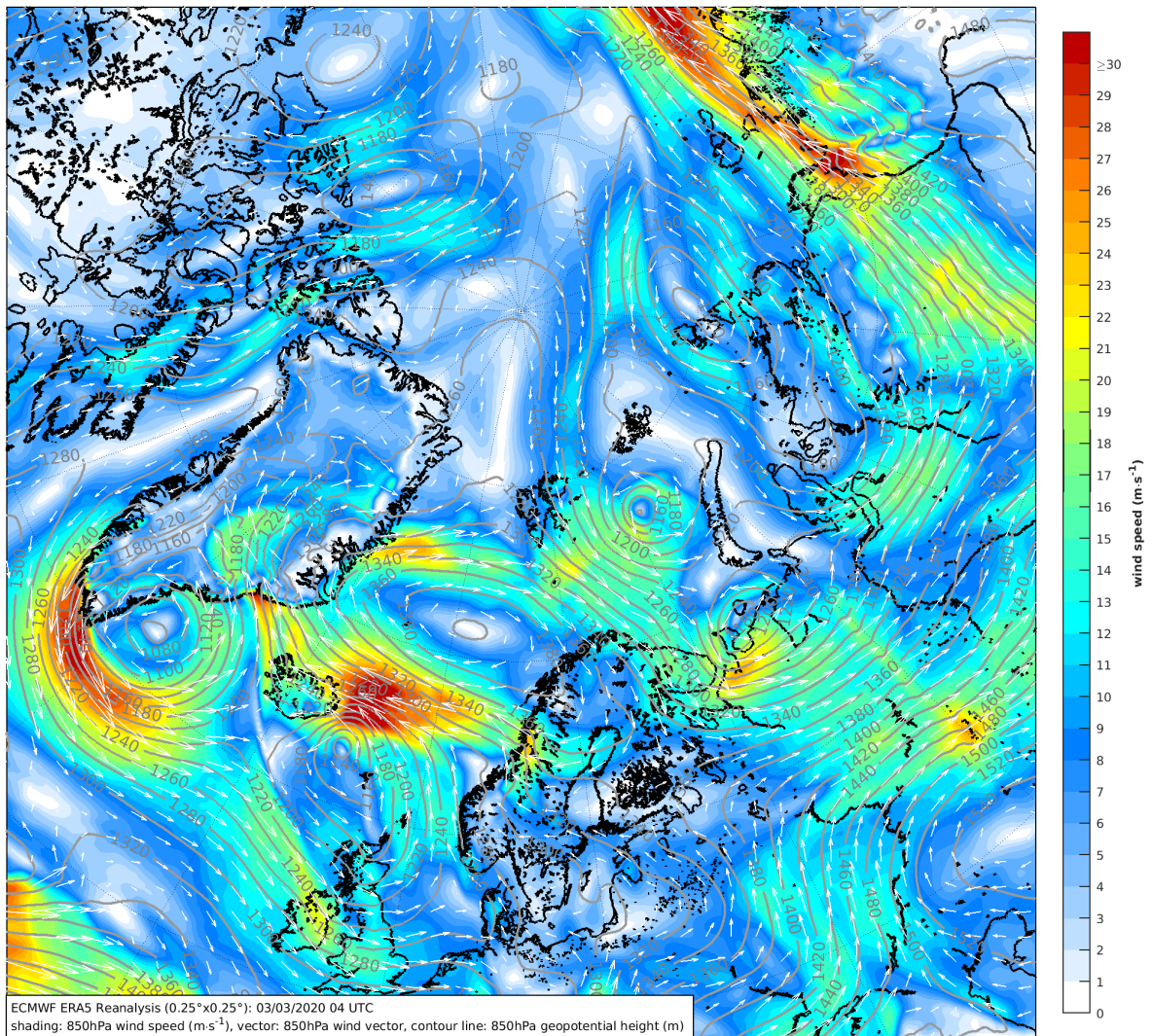


Figure A.16.: ECMWF Reanalysis v5 (ERA5) for 04.03.2020, 04:00 UTC. Shading: 850 hPa wind speeds; vectors: 850 hPa wind vectors; contour lines: 850 hPa geopotential height (GPH) in meter. Plot by Dr. Alexander Schulz.

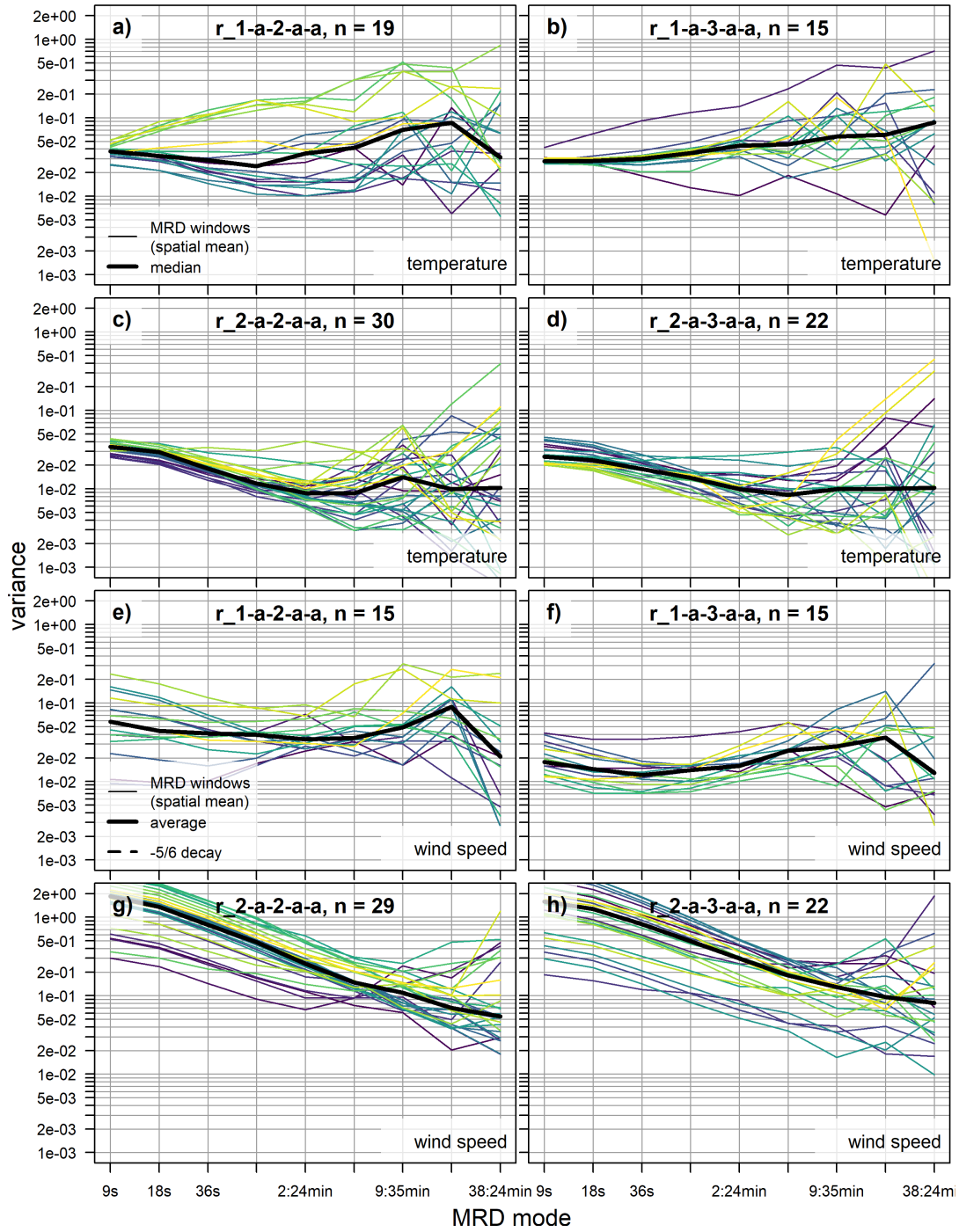


Figure A.17.: Power spectra of fiber-optic distributed sensing (FODS) temperature (a to d) and wind speed (e to h), combined for all horizontal fiber transects except between latter (a) and (d) in figure 2.2. The data are conditionally sampled by regimes with the respective regimes categories according to table 2.1 stated by each plot's title: The parameters (wind speed, wind direction, longwave downwelling radiation, static stability and meandering intensity) are separated by hyphens. 'a' refers to all categories (no sub-sampling), two digits to two categories. Hence, the rows subset by wind speed (1 = weak vs. 2 = strong) and the columns by longwave downwelling radiation (2 = medium vs. 3 = strong). The variance on the y-axis is plotted logarithmically, the x-axis shows the dyadic multi-resolution decomposition (MRD) modes. The colored lines are the variances of single MRD windows, colored chronologically to reveal temporal effects. The bold line connects the medians of each mode.

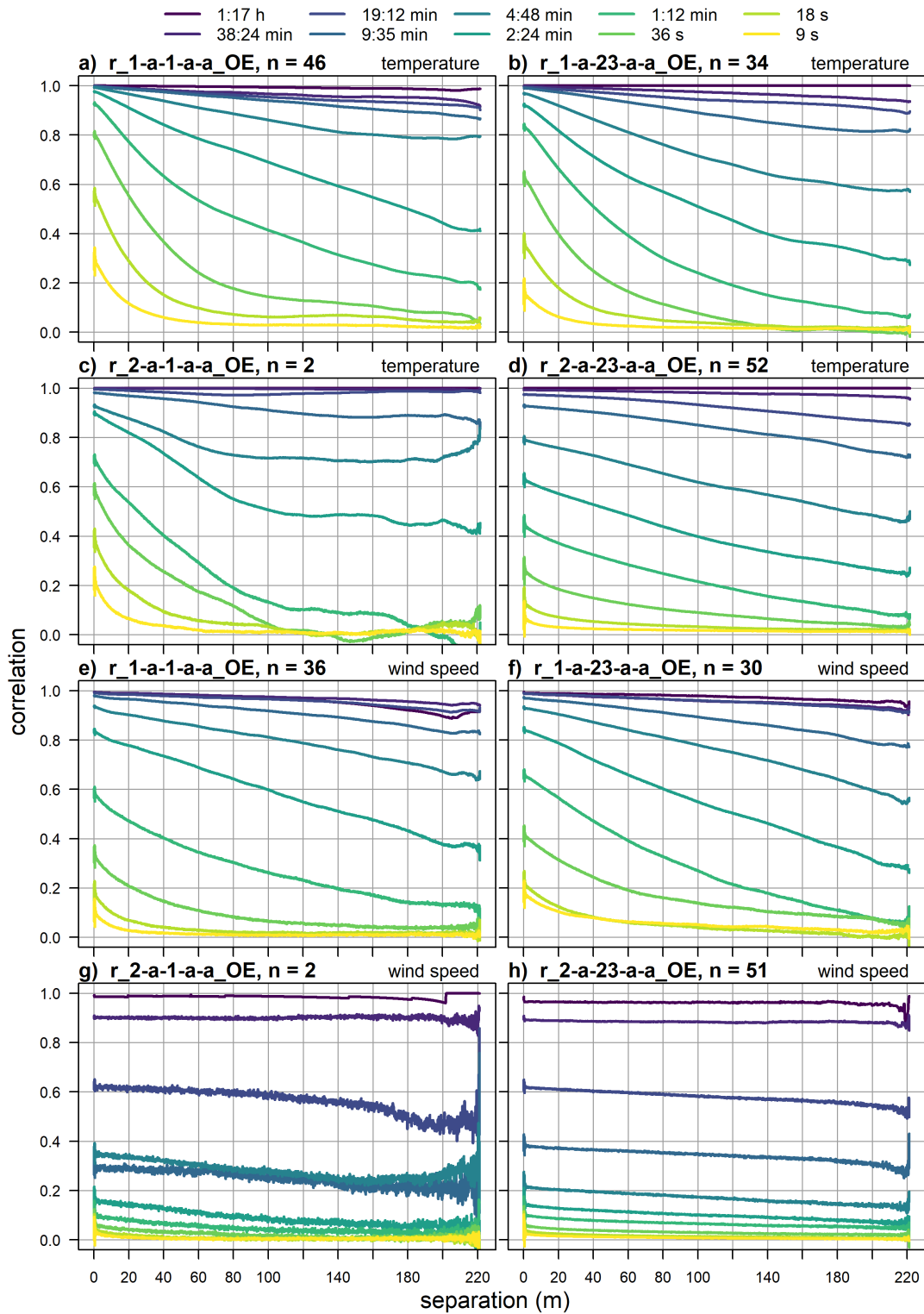


Figure A.18.: Spatially aggregated temporal correlation coefficients of fiber-optic distributed sensing (FODS) temperature (a to d) and wind speed (e to h) against the separation distance for the fiber transect between the OBSE and EDDY tower ((d) and (e) in figure 2.2). The correlations are computed for time scales from 9 s to 77 min indicated by the colors, based on a multi-resolution decomposition (MRD). The data are conditionally sampled by regimes with the respective regimes categories according to table 2.1 stated by each plot's title: The parameters (wind speed, wind direction, longwave downwelling radiation, static stability and meandering intensity) are separated by hyphens. 'a' refers to all categories (no sub-sampling), two digits to two categories. Hence, the rows subset by wind speed (1 = weak vs. 2 = strong) and the columns by longwave downwelling radiation (1 = weak vs. 23 = medium and strong).

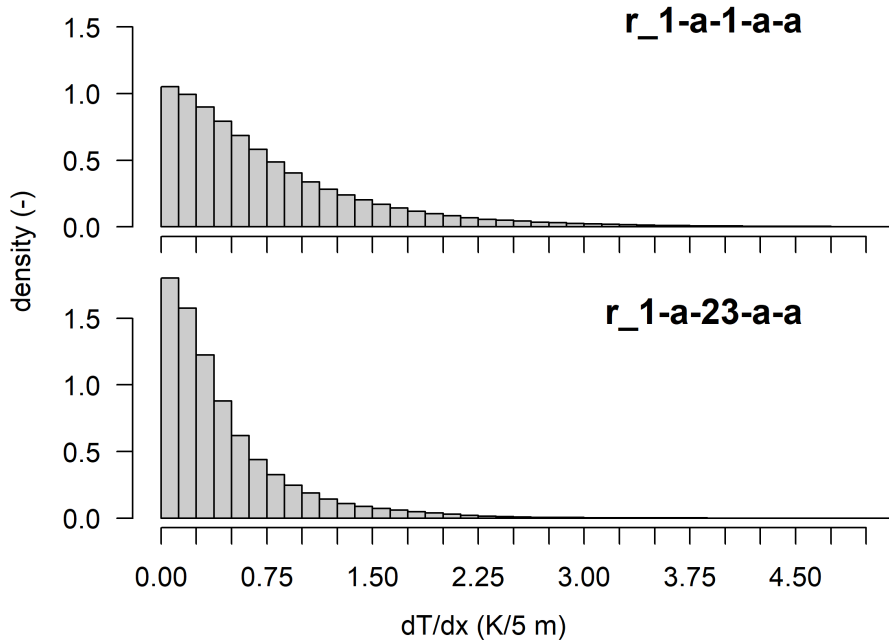


Figure A.19.: Density histograms of temperature differences along all horizontal sections of the fiberoptic distributed sensing (FODS) setup with a temporal resolution of 9 s. Differences are calculated between block averages of 4.8 m width, shifted along the fiber. Results are shown for all regime windows with weak-winds and clear-sky conditions (top) as well as weak-wind and cloudy conditions (bottom).

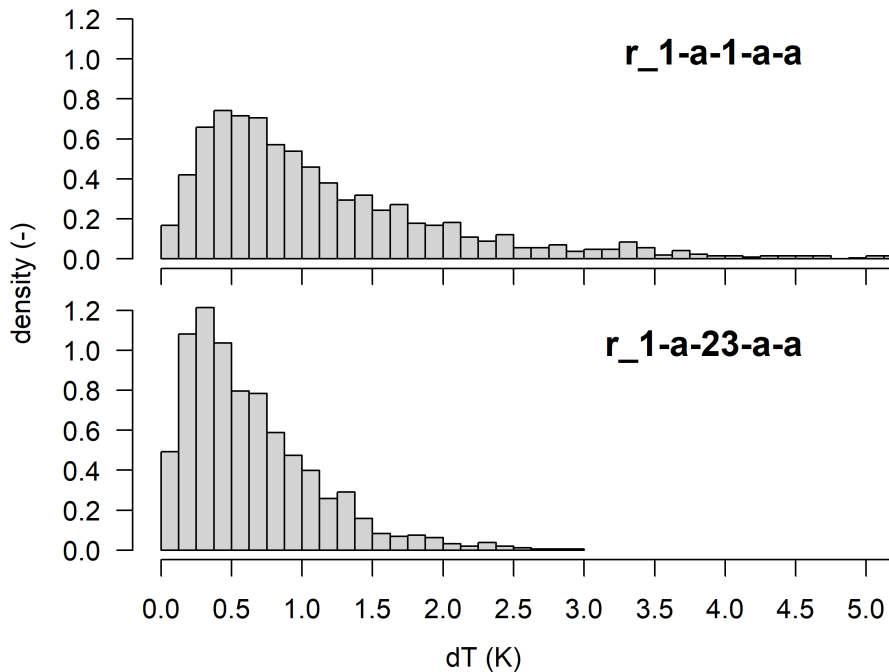


Figure A.20.: Density histograms of the maximum spatial temperature differences between the three USAs at the corners of the setup with a perturbation time scale of 2 min. Results are shown for all regime windows with weak-winds and clear-sky conditions (top) as well as weak-wind and cloudy conditions (bottom).

### A.2.1. Temperature by wind direction

To test the assumption that flows from SW and SSW and the direction of Zeppelin Mountain and Brøgger glacier (SW-sector, Tab. 2.1) were gravity driven density currents or catabatic cold air flows, the relation if incident flow direction and temperature at the measuring array has been investigated for the two example periods in section 3.2.3 (Fig. 3.11). On 26/27.02.2020 (Fig. A.21a) the pattern is less clear compared to the 29.02.2020 (Fig. A.21b) since the trend is superimposed by a decreasing temperature across the sampling period. However, in both cases temperatures mostly decrease by several K when incident flows turn from the SE-sector towards the SW-sector, indicating gravitational forcing for the latter sector.

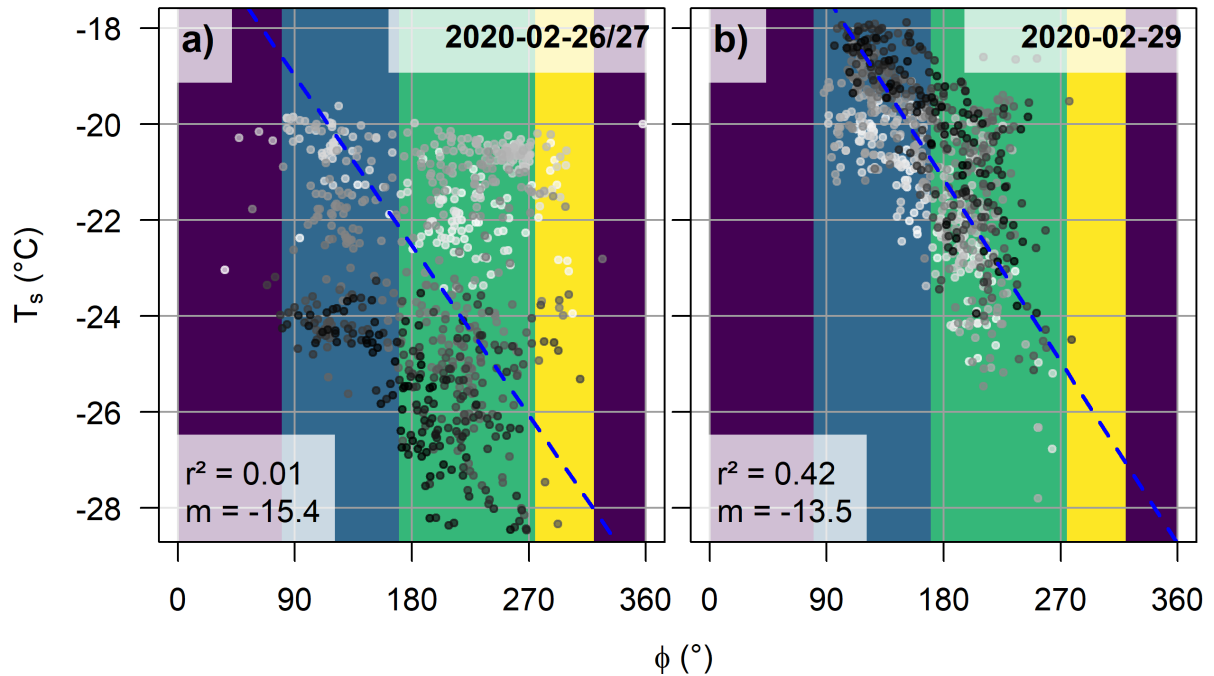


Figure A.21.: Temperatures over wind direction, measured by an USA at the EDDY tower with a perturbation time scale of 2 min. (a) includes the period from 26.02.2020, 14:30 to 27.02.2020, 14:30, (b) covers the 29.02.2020. The periods match those of figure 3.11. The points are colored chronologically from white to black. The vertical colored bars visualize the wind direction sectors listed in table 2.1: NE-sector = 320 – 80, SE-sector = 80 – 170, SW-sector = 170 – 275 and NW-sector = 275 – 320.

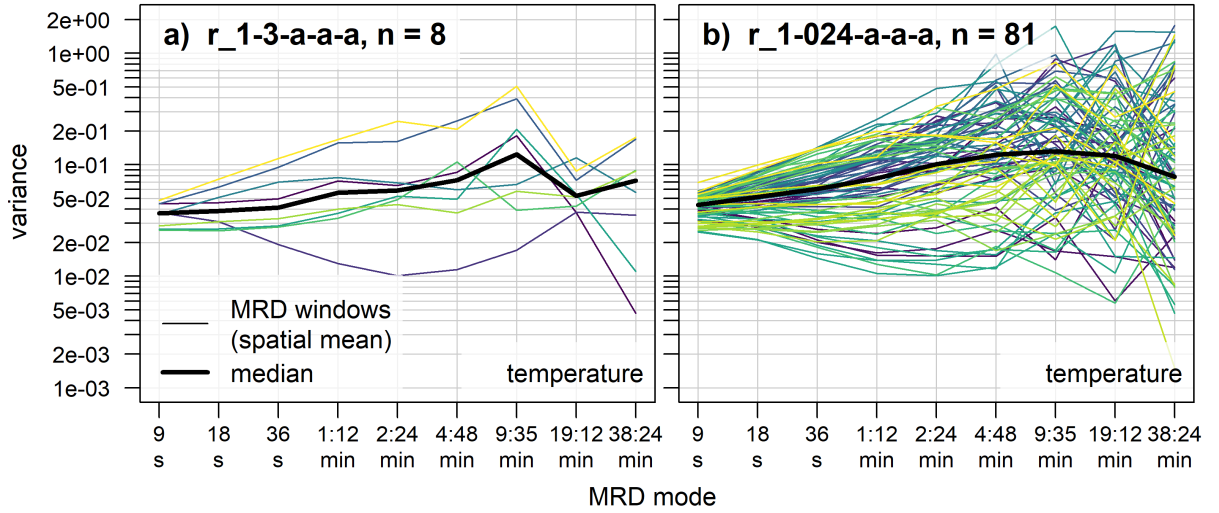


Figure A.22.: Power spectra of fiber-optic distributed sensing (FODS) temperature, combined for all horizontal fiber transects except between letter (a) and (d) in figure 2.2. The data are conditionally sampled by regimes according to table 2.1. **a** only includes weak winds from the SW-sector down the slopes of the adjacent mountains and glaciers while **b** includes weak winds from all other sectors as well as periods with varying sectors. The variance on the y-axis is plotted logarithmically, the x-axis shows the dyadic multi-resolution decomposition (MRD) modes. The colored lines are the variances of single MRD windows, colored chronologically to reveal temporal effects. The bold line connects the medians of each mode.

Table A.1.: Comparison of the  $I \downarrow$  category of regimes with identical regime parameters for all variables except for  $I \downarrow$  (see Sect. 2.5.3). ‘regime a’ and ‘regime b’ are the numbers of the compared regimes according to figure 3.17 while ‘cat. a’ and ‘cat. b’ are the respective  $I \downarrow$  regime categories. The comparisons in the upper block show a lower magnitude of the sensible heat flux  $Q_H$  for higher  $I \downarrow$  which is inverted for the lower block.

regime a	regime b	cat. a	cat. b
# 2	# 3	2	3
# 7	# 15	1	2
# 9	# 12	2	3
# 10	# 19	1	2
# 22	# 31	1	3
# 27	# 28	1	3
# 31	# 32	2	3
# 9	# 17	2	1
# 14	# 16	3	2

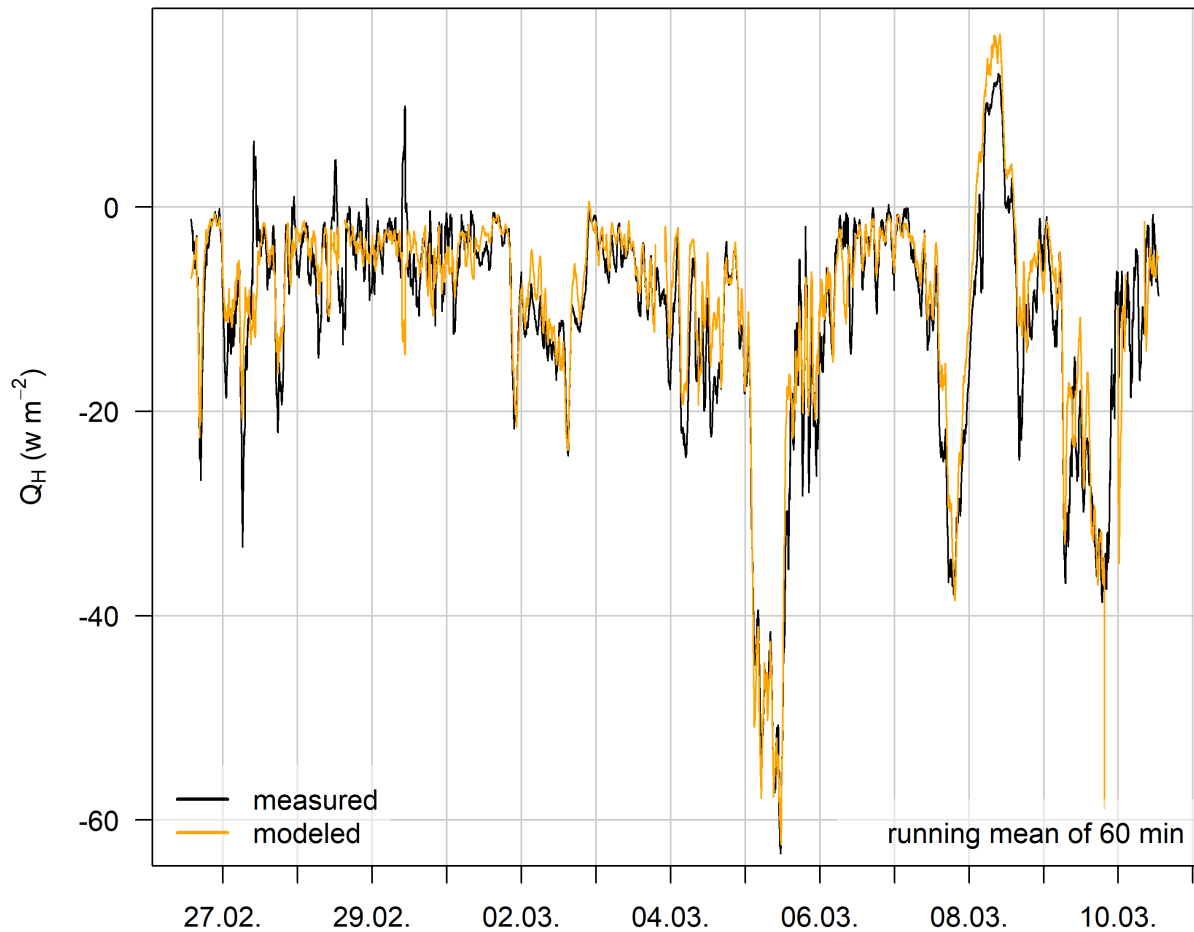


Figure A.23.: Time series of the sensible heat flux  $Q_H$  for the whole campaign period. The black line displays the  $Q_H$  measured by the ultrasonic anemometer (USA) at the BSRN tower while the orange line is the  $Q_H$  modeled using Monin-Obukhov similarity theory (MOST) according to section 2.5.2. The measured flux is processed on a perturbation time scale of 2 min which is also the raw resolution of the modeled  $Q_H$ . A running mean of 60 min is then applied to both for improved clarity.

Table A.2.: Comparison of the meandering category interpercentile range (IPR) of regimes with identical regime parameters for all variables except for IPR (see Sect. 2.5.3 and 2.5.4). ‘regime a’ and ‘regime b’ are the numbers of the compared regimes according to figure 3.17 while ‘cat. a’ and ‘cat. b’ are the respective IPR regime categories. The comparisons in the upper block show a higher magnitude of the sensible heat flux  $Q_H$  for higher IPR which is inverted for the lower block.

regime a	regime b	cat. a	cat. b
# 6	# 21	4	3
# 9	# 11	3	2
# 10	# 17	4	3
# 15	# 16	3	2
# 16	# 18	2	1
# 22	# 27	4	3
# 23	# 30	4	3
# 27	# 29	3	2
# 2	# 4	1	2
# 9	# 19	3	4
# 28	# 32	3	4

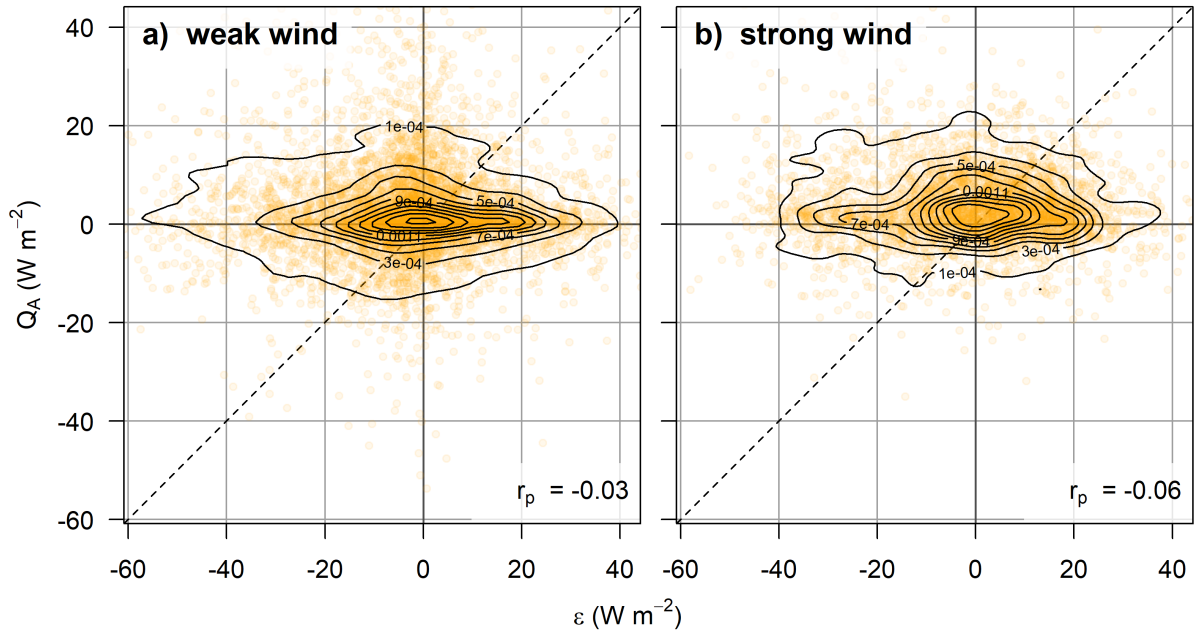


Figure A.24.: Point density of horizontal advection of sensible heat  $Q_A$  against the residual of the surface energy balance  $\epsilon$  (as in Fig. 3.5) for winds below (left) and above (right)  $2.5 \text{ m s}^{-1}$ , measured by the ultrasonic anemometer (USA) at the EDDY tower. The dashed line depicts the 1 : 1 relation.

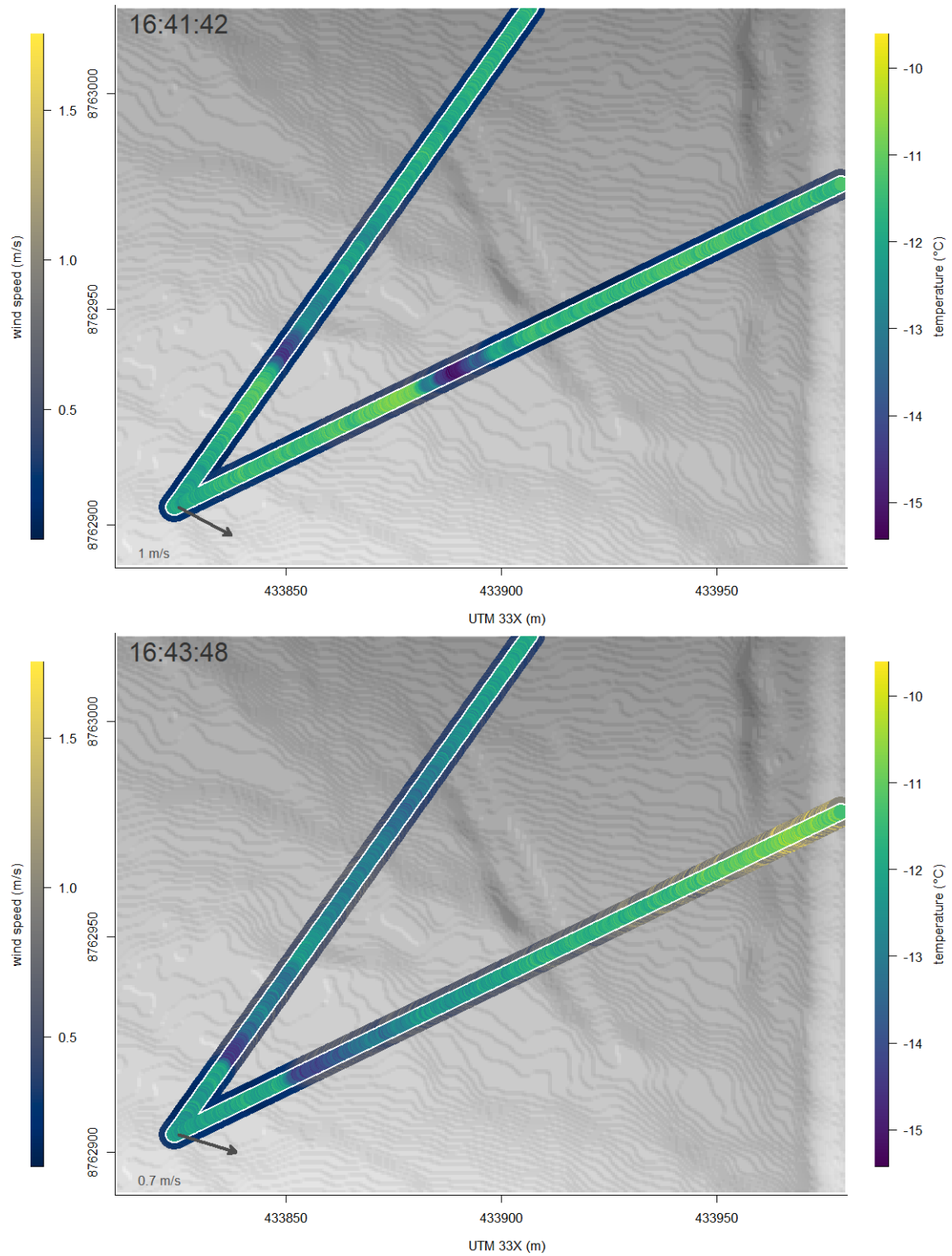


Figure A.25.: Map of the south-western part of the fiber-optic distributed sensing (FODS) setup for two instants of time during the occurrence of a solitary submeso-scale motion (see Sect. 3.4) with the time stamp topleft. The broad colored bars display temperature along the fiber-optic cable at approximately 1 m a.g.l. while the bordering stripes show the wind speed component orthogonal to the fiber. The EDDY tower is located at the bottom left tip of the setup where the grey arrow shows the wind direction recorded by the ultrasonic anemometer (USA) mounted. The respective wind speed is written below. The underlying map is a hillshade based on a digital elevation model (DEM) published by Boike et al. (2018).

# Declaration of authorship

Hereby, I declare that I have authored the master thesis titled

*“What drives submeso-scale motions in the wintertime Arctic atmospheric boundary layer? A field study using Fiber-Optic Distributed Sensing in Ny-Ålesund, Svalbard”*

independently based on my own work. All direct or indirect sources used are acknowledged as references. This thesis has not been published or previously submitted to any other examination board.

---

Date

---

Jannis-Michael Huss